# Structural and Optical Characterization of Solution Processed Lead Iodide Ruddlesden-Popper Perovskite Thin Films

Eli Kinigstein

Submitted in partial fulfilment of the
requirements for the degree of
Doctor of Philosophy
in the Graduate School of Arts and Sciences

COLUMBIA UNIVERSITY
2018

ABSTRACT

Structural and Optical Characterization of Solution Processed Lead Iodide Ruddlesden-Popper Perovskite Thin Films

Eli Kinigstein

Highly efficient LEDs and photovoltaic cells based on spin coated films of layered Ruddlesden-Popper hybrid perovskites (RPPs) have been recently reported. The electronic structure and phase composition of these films remains an open question, and diverse explanations have been offered to account for the excellent device performance. Here we report x-ray and optical characterization of hot cast RPP thin films, emphasizing the distribution of structural and electronic properties through the film depth. Our results indicate an at least 70% phase pure n=3 film results from casting a stoichiometric solution of precursors, with minor contributions from n=2 and n=4 phases. We observe a strong correspondence between the predicted single-crystal RPP reciprocal lattice and measured RPP film wide angle scattering pattern, indicating a highly ordered [101] oriented film. This correspondence is broken at the air-film interface where new scattering peaks indicate the existence of a long wavelength structural distortion localized near the films surface. Using transient absorption spectroscopy, we show that the previously detected luminescent mid-gap states are localized on the films surface. Investigating films of varying thickness, we determine the photo-excited carrier dynamics are dominated by diffusion to this interface state, and extract an excitonic diffusivity of $0.18 cm^2 s^{-1}$. We suggest that the observed surface distortion is responsible for the creation of luminescent mid-gap states.

**Contents:**

**List of Figures:**

1. This panel shows a schematic of the transient absorption spectrometer used in my thesis experiments.
2. This figure shows the set-up utilized to track the real time power of the pump pulse.
3. This figure shows the pump power measured vs time.
4. This figure shows the schematics of the PID control loop power stabilization set up.
5. This figure shows the differential absorption kinetics obtained using the PID power stabilization program.
6. This figure shows the differential absorption spectrum at 5ps measured on films with four different thicknesses

Chapter 5:

1. This figure shows the single crystal n=3 RPP structure in the orientation we expect in our film. We view the structure from the [10-1] direction.
2. This figure shows the observed GIWAXS pattern in hot cast films and post annealed films.
3. This figure shows regions of the GIWAXS scattering pattern characteristic of the layer thickness.
4. This figure compares the reciprocal lattice of the refined film unit cell, the single crystal unit cell, and the measured GIWAXS scattering pattern.
5. This figure shows the anti-phase octahedral tilting pattern present in the empirically determined n=3 RPP single crystal structure.
6. This figure shows the calculated absorption length vs incident angle for n=3 RPP film.

**Acknowledgments:**

Dr. Matthew Sfeir

I owe the successful completion of this PhD to Dr. Sfeir. He gave me the opportunity to do this research when no one else at Columbia would give me a position. He creatively figured out how to fund my PhD research, and taught me with kindness. He picked me from the bottom of the barrel, and together we have done some exciting and important science. I can never repay Dr Sfeir.

Dr. Aditya Mohite

For partially funding my PhD research, and giving me the opportunity to do work on these materials.

Dr. Wanyi Nie and Dr. Hsinhan “Dave” Tsai

For providing the samples I worked on.

Dr. Kevin Yager

For patiently teaching me about x-ray diffraction.

Dr. Robert Mawhinney

For creatively helping to find the funding and time for me to complete my PhD. This PhD would not have been possible if not for the efforts Dr. Mawhinney.

Randy Torres

For offering kind hearted words to me at a time when I was really down in the dumps, and for always being on-point.

Dr. Emlyn Hughes

For bringing me to Columbia, and being an encouraging figure.

Dr. Andrew Millis

For giving me a chance to work on DMFT, and eventually cutting me loose from his condensed matter theory group. In my time with Dr. Millis, I got to learn some many body physics, and see what world class science looks like. I will always aspire to speak as lucidly and with as much insight as Dr. Millis.

Dr. Chee Wei Wong

For the many years of funding he gave to me, in which I learned a lot. Also for introducing me to nonlinear optics, nanoscience, and Dr Sfeir.

Marilinda Pascoe, Noah Kinigstein, Tanya Kinigstein

For being there for me through the whole process, I love you all so much.

Manpreet “Pretzels” Aujla

For being my partner through the toughest years of my PhD.

**Dedication:**

I would like my work to serve as a practical tool for dismantling the world's dependence on fossil fuels. In this sense, I dedicate this work to the future generations living on planet earth.

**Preface:**

This work is part of an on-going effort in the scientific community to develop materials for solar energy conversion which are significantly cheaper to produce than the dominant silicon technology. Much of this work has focused on replacing each semiconductor component in the solar cell by an analogue that can be deposited via solution. One possible solution processed material proposed to replace the silicon active layer is methyl-ammonium lead tri-iodide (MaPbI3). Solution deposited solar cells based on MaPbI3 exhibit a large power conversion efficiency of around 22%. However, these high device efficiencies degrade significantly on the time scale of 100 hours, and the cells are essentially non-operational after a couple of weeks. Therefor it is of great technological interest to develop materials which like MaPbI3 are intrinsically well suited for solution deposition and solar energy conversion, but maintain their material integrity on the timescale of 5 years or longer. A natural place to look for such materials is in the layered derivatives of MaPbI3, of which there are several. The layered Ruddlesden-Popper Perovskites (RPP) of the form Ba2Man-1PbnI3n+1 have been shown to make highly efficient solar cells (~12.5%) and exhibit increased air and moisture stability. However, the operating principals of devices based on these films are not well understood. This thesis is an attempt to understand the processes involved with light absorption and the subsequent motion of electrical energy through solution processed RPP thin films. We show how different solution deposition procedures result in films with strongly divergent structural and optical properties, and provide an interpretation for the widely varying and solar energy conversion efficiencies based on these films.

# Chapter 1:

## Electronic Structure and Optical Properties of Hybrid Organic-Inorganic Perovskites

Introduction

Due to the surge of interest in Hybrid Organic-Inorganic Perovskites (HIOP) for applications in solution processed LEDs and Photovoltaic cells, many groups have focused on simulating and understanding their electronic band structure. $MaPbI_3$ has thus far proven the most successful in optoelectronic applications, so this brief review will focus on this material, as well as it's layered derivatives which are the subject of this thesis. We note that HIOPs differ qualitatively from the familiar perovskite metal-organic frameworks in that they do not contain direct organic-inorganic bonds[1].

$MaPbI_3$ can successfully form large grain polycrystalline films via a low temperature solution based technique on account[2] of it's relatively low activation energy for solid state crystallization between 60kJ/mol and 150kJ/mol[3] (depending on the precursor lead salts used). In contrast the activation energy for an amorphous Silicon film has been measured to be several hundred kJ/mol[4]. However, it is generally believed that the microscopic electronic structure of these crystals is the fundamental driving force behind their optoelectronic utility, rather than the mesoscale structure of the grains[4]. In particular, it is found that all point defects (interstitials, vacancies, substitutions) with low formation-energy form shallow impurities[5], which in principal do not contribute to non-radiative recombination. This is favorable for photovoltaic applications as non-radiative recombination lowers both the open circuit voltage and the short circuit current. This defect tolerance of $MaPbI_3$ is purported to result directly from it's curious band edge electronic structure which is quite different from that of tradition II-VI and III-V ionic semiconductors[5,6]. Band structure calculations have inevitably centered around density functional theory[6] (DFT) and below I will review some of the important results obtained on $MaPbI_3$ before transitioning to a description of the electronic structure of the layered derivatives.

General Structural Properties Of HIOPs

Hybrid Organic-Inorganic Perovskite crystals have a chemical formula of the form $AMX_3$. Where A is a monovalent cation, M is a divalent metal cation and X is a monovalent halide ion. The ability of this combination of elements and molecules to crystallize in the perovskite structure is related to geometric constraints dictated by size of the ions. These geometric considerations can be summed up in the most basic description by the Goldschmidt tolerance factor $t = \frac{R_A + R_X}{\sqrt{2}(R_M + R_X)}$ where $R_i$ (i=A,M,X) are the ionic radii of the various crystal constituent. A tolerance factor close to 1 is a necessary condition to form an undistorted cubic perovskite structure. 0.8<t<1 results in distortions of the octahedra. Given a $(PbI_6)^{-4}$ octahedra, and assuming t=1 implies that $R_A$ should equal 2.6Å for an undistorted perovskite structure. 2.6Å is quite large for an atomic cation, and this results from the relatively large ionic radii of Pb and I. Therefor the molecular cation methylammonium$^+$ is used. The carbon-nitrogen bond in methylammonium$^+$ is ~1.5Å while the N-H and C-H bonds are ~1Å, yielding an effective ionic radius of 2.17Å[1], which implies that $MaPbI_3$ should form a stable, though distorted perovskite structure.

$MaPbI_3$ Crystal Phases

$MaPbI_3$ has three phases, a low temperature orthorhombic phase (T<160K) a room temperature tetragonal phase (160K<T<330K), and a high temperature psudo-cubic phase(T>330K). These phases are associated with a changing effective ionic radius of methylammonium$^+$ which increases as the increasing temperature activates rotational modes around the C-N bond in the tetragonal phase and tumbling modes of the of the C-N bond in the psudo-cubic phase[7]. These crystals therefor exhibit dynamic disorder making first principals simulations challenging. However a number of work-arounds have been implemented with varying degrees of success.

DFT Band Structure of $MaPbI_3$ without Spin Orbit Coupling Analysis of Point Defects

It is found that the orientation of the $MA^+$ ion has a weak impact on the band gap and band edge structure. Reference 5 simulates the tetragonal structure (no $MA^+$ disorder) by fixing the C-N bond to lay on the [111] direction which orients the nitrogen towards one of the faces of the $(PbI_6)^{-4}$ octahedra. This choice undoubtedly gives rise to a different set of octahedral distortions than those observed experimentally[7], as the orientation of the $MA^+$ cation has been shown distort the Pb-I-Pb bond angle[8]. Thus in the context of DFT, the orientational pattern assumed for the $MA^+$ largely determines the tilting pattern adopted by the octahedra. In any event, DFT-GGA simulations of the said structure yield reasonable agreement with the experimentally determined band gap around 1.5eV. However it has been determined that this agreement is spurious[9] as the inclusion of inclusion of spin-orbit coupling (SOC) related to the lead and iodine atoms bring the band gap down to about 0.7eV[10], which shows the huge energetic importance of this effect. The obtained agreement between DFT-GGA and experiment has been attributed to cancelation of errors, involving SOC and correlation effects not accounted for at the GGA level[5]. Without being an expert on DFT, it seems questionable to extract energetic information about the point defects based on DFT-GGA, as it is unclear that the cancelation of errors present for the delocalized bands will obtain in the case of localized point defects. However, reference 5 is cited in many reviews which adopt it's point of view, and concurring DFT predictions have followed[11,12]. We therefor review some of the qualitative aspects of reference 5 below.

The band gap of tetragonal $MaPbI_3$ is located at the R point of the brillouin zone (unchanged by SOC). The conduction band minimum is composed of the Pb $6P_{x,y,z}$ orbitals with a small contribution from the I 5s state. The valance band maximum is composed mostly of I 5p orbitals with a reasonable contribution from the lower energy lead Pb 5s states. The strong interaction between the I 5p states and the Pb 5s states at the valance band maximum is anti-bonding in character, which pushes the valance band maximum higher in energy than the normal

position of the I 5p states. This situation in which the conduction band is located on the metallic cation, and the valance band is mostly localized on the halogen anion reflects the ionic nature of the crystal. Specifically, the two Pb 6p valance electrons present in metallic lead are transferred to Iodine, and these empty states form the conduction band. In the absence of orbital hybridization between lead and iodine (a covalent bond) the crystal is held together by electrostatic interactions. Qualitatively, this situation does not change by the inclusion of spin orbit coupling, or changing the orientation of $MA^+$.

Point defects are simulated in a 3x3x3 super cell, which is large enough that the impurities don't spatially overlap, and thus no impurity bands are formed in the simulation. Based on a thermodynamic analysis of the formation energies of various defects they conclude that a lead vacancy and a $MA^+$ substitution at a lead site are the dominant acceptor point impurities, and they are derived from the I 5p orbitals. Without the antibonding interactions with the lead ions in these two cases, the energy of the I 5p orbitals is decreased which puts these impurity energies in the valance band. Likewise, the dominant donor point defects are $MA^+$ interstitials and Iodine vacancies which are composed of the Pb 6p orbitals. Because the $MA^+$ ions have no covalent bonds to the inorganic lattice components, they don't create sub gap states when they exist at interstitials. Similarly, due to lack of bonding interactions between I and Pb (iconicity), an iodine vacancy has very little effect on the Pb 6p orbitals. All other defects are shown to have large formation energies, and thus are much less likely to occur during formation. The lack of deep impurity levels means that photoexcited carriers can be trapped, but escape those traps with relative ease. Thus these point defects do not serve as non-radiative recombination centers.

DFT with Spin Orbit Coupling

To understand the effects of spin orbit coupling, a cubic lead halide perovskite phase was simulated in reference 6. Here the $MA^+$ ions are replaced by cesium$^+$, which is shown to have no effect on the band edge electronic structure due to lack of covalent interactions with between the

octahedra and the ion on the A site. This is necessary because the cubic phase features dynamic disorder associated with the rotation and tumbling motion of the $MA^+$ ions, which results a cubic structure on average[7]. The inclusion of spin orbit coupling in a DFT-LDA calculation splits both the conduction band and the valance band, significantly reducing the degeneracy of both. The conduction band minimum becomes the spin orbit split off band which now has a degeneracy of 2 (previously 6), and is shifted down by an amount $2\Delta_{SO}/3$. The remaining 4 states are shifted up by an amount $\Delta_{SO}/3$. A similar effect is produced on the valance band, except these states have opposite parity from the conduction band, and thus the direct band gap nature is preserved. Information on spin orbit coupling in the tetragonal phase can be obtained by parameterizing a k-p Hamiltonian model with the bands from the cubic phase (without SOC). With this k-p Hamiltonian the electronic structure of the band edge of the tetragonal phase can be obtained by considering the tetragonal structure as a perturbative strain acting on the cubic phase. With this model it is shown that the effects of spin orbit coupling always dominate those produced by the strain, thus we expect the band edge of the other perovskite phases to be dominated by SOC as well.

Relativistic GW

A number of papers have shown that the correlation corrections in the DFT+GW approximation increase the energy of the band gap, counteracting the shift due to spin orbit coupling. These calculations show that systematically including the many body correlation effects in conjunction with SOC results in a band gap (1.67eV) in reasonable agreement with what observed experimentally[13](1.6eV) .

Electronic Structure of Layered HIOP Single Crystals

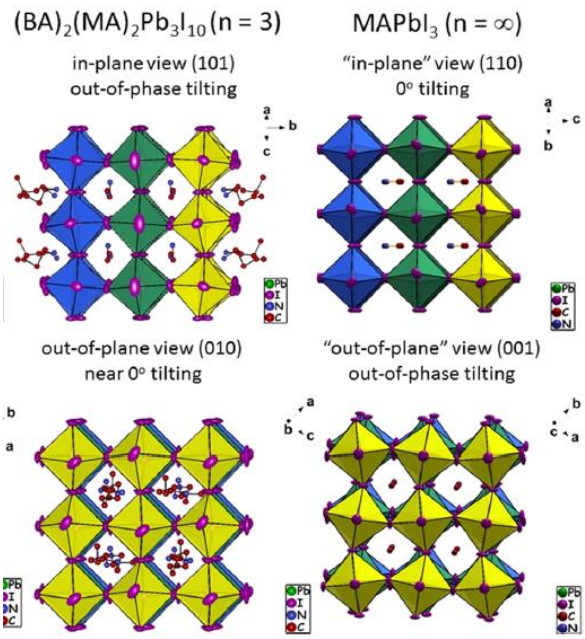


**Figure 1.** This figure compares the crystal structure of $MaPbI_3$ with it's layered derivative $(Ba)_2(Ma)_2Pb_3I_{10}$ which is the subject of this thesis.

Lead Halide Ruddelsden-Popper Perovskites (RPPs) such as $(Ba)_2(Ma)_{n-1}Pb_nI_{3n+1}$ (figure 1a) are a family of layered compounds related to the $MAPbI_3$ structure. $MaPbI_3$ devices are plagued by instability and degradation in ambient conditions. However the layered RPP materials exhibit enhanced moisture and air stability[14–18], with suppressed ion migration[19] compared to $MAPbI_3$. Each layer has an inorganic core of $(PbI_6)^{-4}$ octahedra , and a capping layer of butylammonium ions which electronically isolate the slabs from each other[20,21]. The inorganic core can be constructed conceptually by taking a slab out of the $MaPbI_3$ crystal structure parallel to the [110] plane. The number of $(PbI_6)^{-4}$ octahedra composing the slab thickness determines 'n' in the chemical formula $(BA)_2(MA)_{n-1}Pb_nI_{3n+1}$. The organic capping layer is constructed by substituting the surface methyl ammonium cations for the bulkier butly-ammonium cations. This structure can be regarded as a self-assembled multiple quantum well. The octahedral periodicity is completely out of phase in adjacent slabs which is driven by the bulkiness of the butylammonium hydrocarbon chain, and is characteristic of the Ruddelsden-Popper phase.

Phase pure (containing only one n value) single crystals of $(BA)_2(MA)_{n-1}Pb_nI_{3n+1}$ have been produced in solution and characterized by x-ray diffraction[8,22,23]. Single crystals exhibit room temperature excitonic luminescence[8,22]. However, because of the large unit cell, and the expected large impact of spin orbit coupling (described in the previous sections), simulations are strongly limited by computational resources. Simulating the optical properties requires the resolution of the

Bethe-Salpeter equations to account for excitonic effects, which has not been possible up to this point. By analogy with type 1 quantum wells it seems reasonable to attempt an effective mass model in the envelope function approximation to understand the confinement effects of the ultrathin inorganic slabs. Physically this picture makes sense because the crystal structure consists of alternating layers of a small band gap semiconductor separated by much larger band gap organic materials. However, to construct an effective mass model the bulk parameters (effective mass, band offsets) of the heterostructure must be known. The bulk parameters of $MaPbI_3$ may be reasonably assumed for the core of the slab provided that passivating ions are included, however there is ambiguity in defining the parameters of the organic spacer layers in the crystal. Futhermore, the envelope function approximation assumes that the Bloch functions at the interface are very similar which is clearly not the case[21].

Briefly the electronic structure at the level of DFT will be reported for comparison with the $MaPbI_3$. Similar to the bulk $MaPbI_3$ phase, the band edge of the layered materials exhibit the ionic character that one would expect. The conduction band is composed of the lead 6p states while the valance band consists of the iodine 5p states with a small contribution from lead 5s. The n=3 layered compound exhibits a direct band gap at the Γ point[8], however the band gap is systematically underestimated at this level of calculation. The variation of the band gap with layer thickness is qualitatively reproduced. The valance band has an effective mass of $0.14m_e$ and the conduction band has an effective mass of $0.09m_e$ which is close to constant as a function of layer thickness. The effective mass in the direction corresponding to the layer stacking is observed to be very large, indicating highly anisotropic transport is expected. Spin orbit interactions can only be applied to the n=1 crystal ($BA_2PbI_4$) due to the large number of atoms in the unit cell of thicker layered materials. Similar to $MaPbI_3$ it is found that including the spin orbit interaction drastically decreases the band gap to way below the experimental values, but results in no change in the band dispersion.

Below the band gap, an additional absorption peak is observed, and room temperature photoluminescence is observed at the positions of these lower energy peaks. These peaks shift with the band gap as the layer number increases, and are attributed to excitonic absorption. The presence of stable room temperature excitons in layered perovskites has received much attention[24,25], and has been explained by a combination of reduced dimensionality and an image charge effect. It's well known that the two dimensional hydrogen atom exhibits a binding energy four times larger than the three dimensional hydrogen atom[26]. The image charge effect results from the dielectric mismatch between the organic spacer and the perovskite core which results in a slab surface polarization charge which has the same sign as the carrier. These induced charges increase the coulomb interaction between the carriers and thus the binding energy[8,20,21,24,27,27,28]. A wide range of binding energies have been reported for the n=3 phase from 20meV[8] up to greater than 200meV[25]. The value of 20meV from reference 8 is the lowest found in the literature, with most values larger than 100meV.

Spin Coated Films of Layered HIOP

The technologically useful form of layered perovskite materials is obtained by dissolving the purified single crystals, and subsequently spin coating the solution onto the desired substrate. In this way solution processed solar cells in a planar PIN geometry have achieved a 12.5% power conversion efficiency under simulated sunlight. These devices exhibited increase air stability compared to $MaPbI_3$ devices and operated un-encapsulated for 2250 continuous hours with an only 60% degradation in power conversion efficiency. Encapsulated devices show no signs of degradation in efficiency[14]. In contrast $MaPbI_3$ devices generally drop to 40% within 100 hours, although certain notable exceptions exist. Similarly, highly efficient solution processed LED have been produced from spin coated films[16].

It is strange that such good devices have been obtained in reference 14, in light of the strongly bound excitons that dominate the optical properties, and large band gap of the material.

However, such device efficiencies are not typical[15,22,29] of these materials. The best performing devices are obtained using a 'hot casting' spin coating procedure. Devices based on hot cast films consistently out-perform layered perovskite films deposited by other methods. In the hot casting method glass substrates coated with a transparent hole conducting material are heated to $110^0$C. They are then placed on the spin coating chuck where a solution of DMF and dissolved single crystal perovskites are deposited on them and allowed to dry in ambient. The resulting films are optically smooth, and no subsequent annealing steps are necessary. AFM images of these films show a ~300nm lateral grain size. Although the resulting films are polycrystalline, they all have their [101] planes parallel to the substrate, yielding sharp Bragg peaks in grazing incidence x-ray diffraction experiments[14,25]. This amazing macroscopic out of plane alignment of the crystal grains, results in the two dimensional slabs standing strictly perpendicular to the substrate. Incredibly, cross sectional SEM images of RPP thin film solar cells show no visible grain boundaries in the out of plane direction[14,22,25]. Thus we expect that the strong orientation of perovskite slabs is related to the high efficiency obtained in devices based on hot cast films.

The unit cell of the species existing in hot cast the thin films is found to be very similar to that of the single crystals. However, the optical properties of the films have notable differences from the single crystals regardless of the spin coating deposition procedure. The films contain an emissive sub gap state who's exact energy seems to depend greatly on the processing conditions of the film. In hot cast films it was suggested that this state has a positive impact on device performance. This thesis is an attempt to understand the nature of that sub gap state, how it interacts with the excitons native to the material, and it's relationship to the macroscopic alignment of the grains [101] crystallographic planes parallel to the substrate observed in hot cast films. We attempt to answer these questions by performing broad band ultrafast transient absorption spectroscopy, and grazing incidence X-ray diffraction on a set of hot cast of n=3 RPP films of

varying thickness. This work was carried out at the Center for Functional Nanomaterials (CFN) and the National Synchrotron Light Source-II (NSLS-II), both located at Brookhaven National Lab.

1. Saparov, B. & Mitzi, D. B. Organic–Inorganic Perovskites: Structural Versatility for Functional Materials Design. *Chem. Rev.* **116,** 4558–4596 (2016).

2. Huang, J., Yuan, Y., Shao, Y. & Yan, Y. Understanding the physical properties of hybrid perovskites for photovoltaic applications. *Nat. Rev. Mater.* **2,** 17042 (2017).

3. Moore, D. T. *et al.* Crystallization Kinetics of Organic–Inorganic Trihalide Perovskites and the Role of the Lead Anion in Crystal Growth. *J. Am. Chem. Soc.* **137,** 2350–2358 (2015).

4. Köster, U. Crystallization of amorphous silicon films. *Phys. Status Solidi A* **48,** 313–321 (1978).

5. Yin, W.-J., Shi, T. & Yan, Y. Unusual defect physics in $CH_3NH_3PbI_3$ perovskite solar cell absorber. *Appl. Phys. Lett.* **104,** 063903 (2014).

6. Even, J. *et al.* Solid-State Physics Perspective on Hybrid Perovskite Semiconductors. *J. Phys. Chem. C* **119,** 10161–10177 (2015).

7. Whitfield, P. S. *et al.* Structures, Phase Transitions and Tricritical Behavior of the Hybrid Perovskite Methyl Ammonium Lead Iodide. *Sci. Rep.* **6,** (2016).

8. Stoumpos, C. C. *et al.* Ruddlesden–Popper Hybrid Lead Iodide Perovskite 2D Homologous Semiconductors. *Chem. Mater.* **28,** 2852–2867 (2016).

9. Mosconi, E., Amat, A., Nazeeruddin, M. K., Grätzel, M. & De Angelis, F. First-Principles Modeling of Mixed Halide Organometal Perovskites for Photovoltaic Applications. *J. Phys. Chem. C* **117,** 13902–13913 (2013).

10. Even, J., Pedesseau, L., Jancu, J.-M. & Katan, C. Importance of Spin–Orbit Coupling in Hybrid Organic/Inorganic Perovskites for Photovoltaic Applications. *J. Phys. Chem. Lett.* **4,** 2999–3005 (2013).

11. Kim, J., Lee, S.-H., Lee, J. H. & Hong, K.-H. The Role of Intrinsic Defects in Methylammonium Lead Iodide Perovskite. *J. Phys. Chem. Lett.* **5,** 1312–1317 (2014).

12. Yun, S., Zhou, X., Even, J. & Hagfeldt, A. Theoretical Treatment of $CH_3NH_3PbI_3$ Perovskite Solar Cells. *Angew. Chem. Int. Ed.* **56,** 15806–15817 (2017).

13. Umari, P., Mosconi, E. & De Angelis, F. Relativistic GW calculations on CH3NH3PbI3 and CH3NH3SnI3 Perovskites for Solar Cell Applications. *Sci. Rep.* **4,** (2015).

14. Tsai, H. *et al.* High-efficiency two-dimensional Ruddlesden–Popper perovskite solar cells. *Nature* **536,** 312–316 (2016).

15. Smith, I. C., Hoke, E. T., Solis-Ibarra, D., McGehee, M. D. & Karunadasa, H. I. A Layered Hybrid Perovskite Solar-Cell Absorber with Enhanced Moisture Stability. *Angew. Chem. Int. Ed.* **53,** 11232–11235 (2014).

16. Tsai, H. *et al.* Stable Light-Emitting Diodes Using Phase-Pure Ruddlesden-Popper Layered Perovskites. *Adv. Mater.* **30,** 1704217 (2018).

17. Xinqian, Z. *et al.* Vertically Oriented 2D Layered Perovskite Solar Cells with Enhanced Efficiency and Good Stability. *Small* **13,** 1700611 (2017).

18. Proppe, A. H. *et al.* Synthetic Control over Quantum Well Width Distribution and Carrier Migration in Low-Dimensional Perovskite Photovoltaics. *J. Am. Chem. Soc.* **140,** 2890–2896 (2018).

19. Xiao, X. *et al.* Suppressed Ion Migration along the In-Plane Direction in Layered Perovskites. *ACS Energy Lett.* **3,** 684–688 (2018).

20. Even, J., Pedesseau, L. & Katan, C. Understanding Quantum Confinement of Charge Carriers in Layered 2D Hybrid Perovskites. *ChemPhysChem* **15,** 3733–3741 (2014).

21. Pedesseau, L. *et al.* Advances and Promises of Layered Halide Hybrid Perovskite Semiconductors. *ACS Nano* **10,** 9776–9786 (2016).

22. Cao, D. H., Stoumpos, C. C., Farha, O. K., Hupp, J. T. & Kanatzidis, M. G. 2D Homologous Perovskites as Light-Absorbing Materials for Solar Cell Applications. *J. Am. Chem. Soc.* **137,** 7843–7850 (2015).

23. Peng, W. *et al.* Ultralow Self-Doping in Two-dimensional Hybrid Perovskite Single Crystals. *Nano Lett.* **17,** 4759–4767 (2017).

24. Ishihara, T. Optical properties of PbI-based perovskite structures. *J. Lumin.* **60–61,** 269–274 (1994).

25. Blancon, J.-C. *et al.* Extremely efficient internal exciton dissociation through edge states in layered 2D perovskites. *Science* **355,** 1288–1292 (2017).

26. Yang, X. L., Guo, S. H., Chan, F. T., Wong, K. W. & Ching, W. Y. Analytic solution of a two-dimensional hydrogen atom. I. Nonrelativistic theory. *Phys. Rev. A* **43,** 1186–1196 (1991).

27. Sapori, D., Kepenekian, M., Pedesseau, L., Katan, C. & Even, J. Quantum confinement and dielectric profiles of colloidal nanoplatelets of halide inorganic and hybrid organic–inorganic perovskites. *Nanoscale* **8,** 6369–6378 (2016).

28. Tanaka, K. & Kondo, T. Bandgap and exciton binding energies in lead-iodide-based natural quantum-well crystals. *Sci. Technol. Adv. Mater.* **4,** 599–604 (2003).

29. Chen, A. Z. *et al.* Origin of vertical orientation in two-dimensional metal halide perovskites and its effect on photovoltaic performance. *Nat. Commun.* **9,** (2018).

# Chapter 2:

## X-Ray Scattering Experimental Systematics

X-Ray Scattering Experimental Details

Grazing incidence x-ray scattering techniques make use of high intensity x-ray beams incident on the sample at very low angles (<$1^0$). This low incident angle implies that the almost microscopic beam (50μmX200μm) is spread out over macroscopic distances on the sample surface, greatly enhancing the scattering cross section. This allows the assessment of the crystalline quality of films as thin as 20nm. In addition to an increased cross section, the very low incident angles allow one to leverage the phenomenon of total external reflection of the x-rays to obtain a quantitative picture of the crystalline structure as a function of depth in the film. However the increased scattering cross section comes at a the expense of a greatly reduced resolution in the $|\vec{Q}|$ direction.

Theory of X-ray Scattering

The interaction of the x-rays with the average electron density in the sample is accounted for by the "jellium" approximation[1], producing an effective refractive index which is less than 1 by roughly $10^{-5}$. This yields very small Fresnel reflection coefficients for angles above the critical angle. Physically, we can consider the observed scattering as arising from the fluctuations in the electron density which are characteristic of the of the crystal structure. X-rays incident on the sample cause the fluctuations electron density to oscillate in phase with the radiation, and the oscillating electron density from each point produces a spherical wave in accordance with the Huygens-Fresnel principal. In the far field, the scattered wavelets are approximately plane waves with a phase that depends on it precise positon in the sample. The contributions from the ensemble of scatterers add coherently at the detector. Therefor periodic structures in the sample cause constructive interference in discrete directions, and totally destructive interference in other directions which result in intense scattering in specific directions called Bragg peaks. The scattering directions can be related to the size of the periodicity in the sample. The so-called kinematic structure amplitude (proportional to the scattered field amplitude) is given by : $F(\vec{Q}) = \int \Delta\rho(\vec{x}) e^{i\vec{Q}\cdot\vec{x}} d^3x$ where $\vec{Q} =$

$\overrightarrow{k_\iota} - \overrightarrow{k_s}$ is the difference between the incident wave vector and the scattered wave vector. This shows that a periodicity of length scale L in the sample scatters the incident radiation by $|\overrightarrow{Q}|$=2π/L. Thus by measuring the x-ray scattering peaks we can evaluate the periodicities present in our sample to deduce information about the basic crystal structure. The photon flux (photons/s*mm$^2$) scattered $\vec{Q}$ is thus given by $I_0 r_e^2 \langle F(\vec{Q})F(\vec{Q})^* \rangle$ [1] where $r_e$ is the classical electron radius which equal 2.8x10$^{-5}$Å $I_0$ is the incident flux, and the brackets indicate thermal averaging. This expression omits factors related to the transmission coefficient of the surface, and the polarization of the beam as they do not affect the Q structure of the expected scattering and only modify the peak magnitudes. In light of this somewhat nuanced variation of the peak magnitudes with incident angle and scattered angle we will refrain from analyzing the peak magnitudes quantitatively in this thesis. Instead our analysis is based on the locations of the observed Bragg peaks, and the expected periodicities present in the structural model of our crystalline samples. These periodicities are conveniently specified by the use of the miller indices [h k l]. By indexing the observed peaks with [h,k,l] values we can quantitatively compare the observed unit cell dimensions and orientation with what we expect based on our model.

Generation of X-Rays at the National Synchrotron Light Source-II (NSLS-II)

NSLS-II is an 3GeV electron storage ring operating at 600mA. Highly relativistic electrons are cut off of the main beam at 60 different end station (not all up and running). The complex materials scattering end station utilizes a three pole magnetic wiggler to accelerate the electrons producing x-ray radiation. These magnets operate at a peak field of 1.14T. The longitudinal length of the wiggler system is 0.25 meters with a gap of 28mm through which the beam is guided. This system produces broad band x-ray radiation between 10keV and 17keV which is then filtered using a monochromator and conditioned with the help of 4 adjustable slits to control the beam shape at

the sample. Our experiments utilized 13.5keV photons with a wavelength of approximately 0.9184Å.

Limits on the $|\vec{Q}|$ resolution

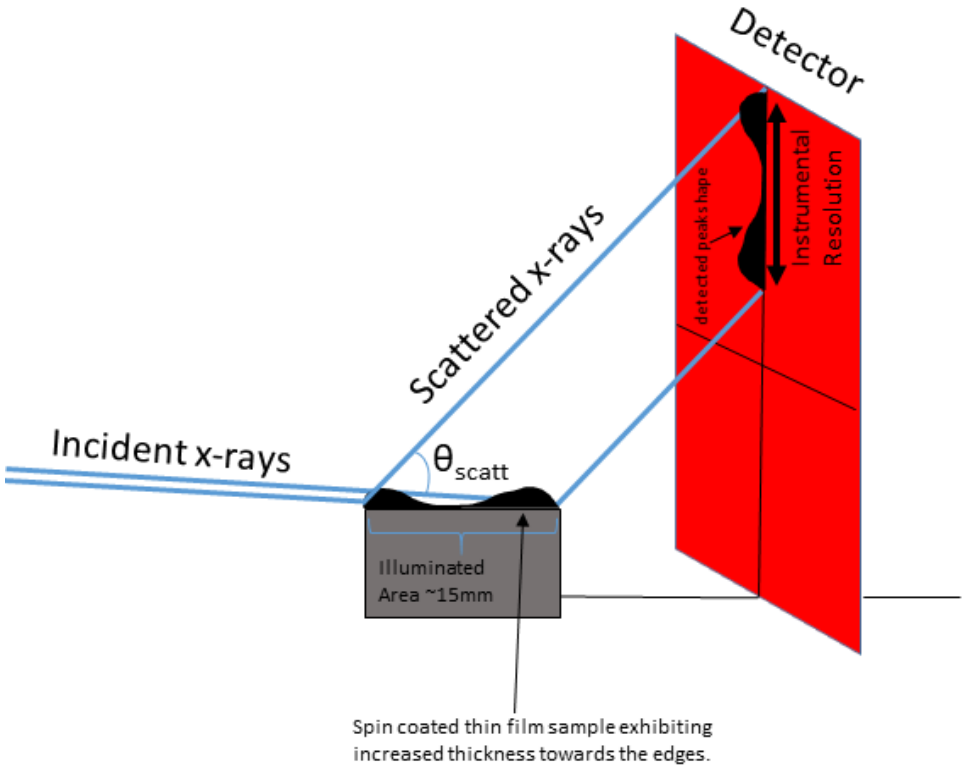


**Figure 1.** This figure shows the physical origin limiting the $|\vec{Q}|$ resolution of the GIWAXS setup at the CMS beam line.

Physically the limits on the GIWAXS $|\vec{Q}|$ resolution are imposed by the large beam footprint on the sample and the large scattering angle as is shown in figure 1. Thus any features that occur with a $|\vec{Q}|$ variation smaller than the resolution must come from localized points on the film. This ambiguity in the position on the film from which the scattering arises translates into an ambiguity in the true scattering vector. Thus sharp features that arise at low incident angle have to be considered with some care when attempting to physically interpret them in term of periodicities present in the sample crystal structure. One prominent effect we see in our data relates to the accumulation of material at the perimeter of our samples. This effect is a consequence of the spin

coating procedure by which they were made. Figure 2 shows our samples mounted in the scattering chamber at the CMS beam line, and they clearly display thick ridges around the edges, which are expected to result in sharp shoulders on the high |Q| edges of the Bragg peaks at low incident angle, and such features are observed in our data.

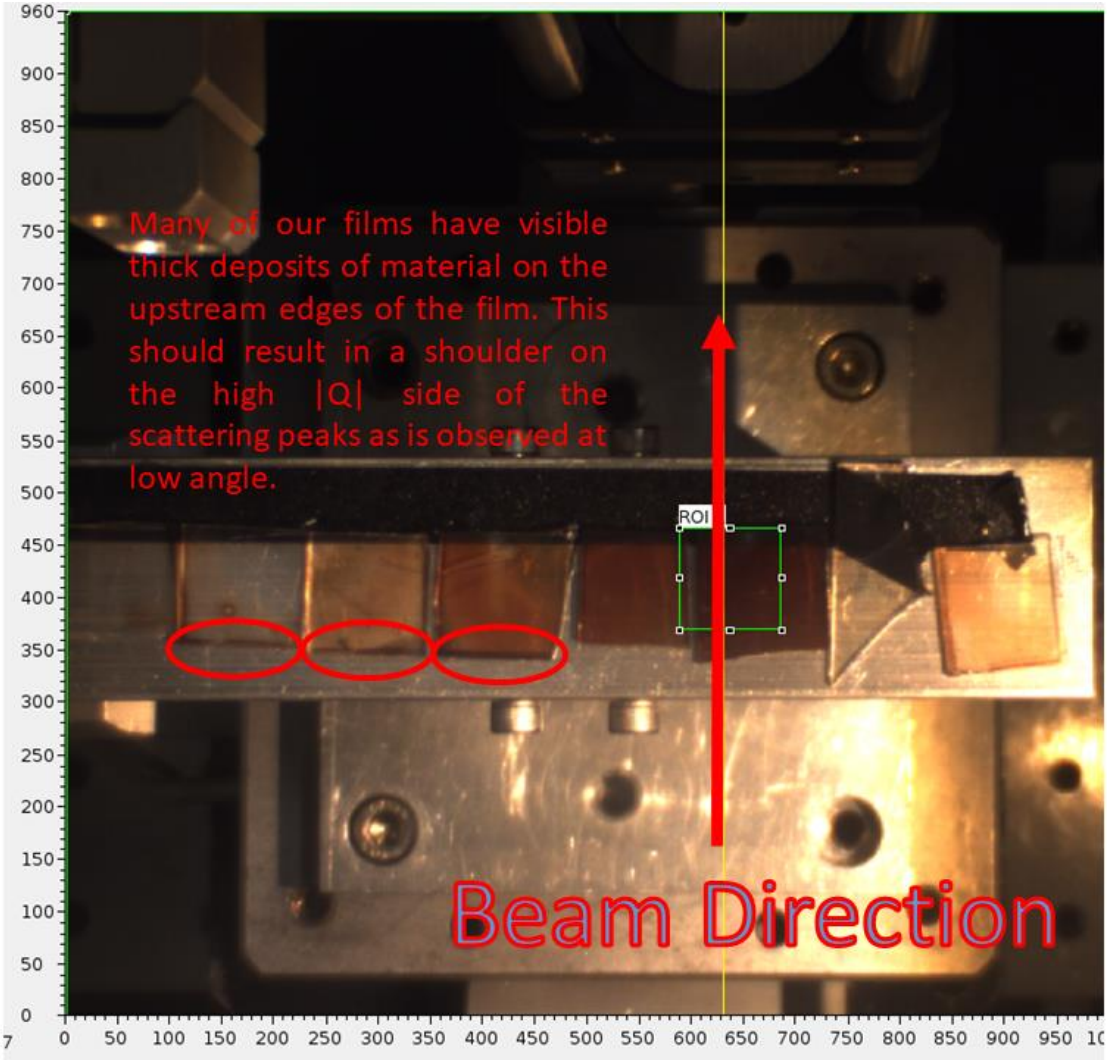


**Figure 2.** This figure shows the samples mounted on the alignment chuck in the scattering chamber. The accumulation of material on the sample edges are circled for clarity.

1. Dosch, H. *Critical Phenomena At Surfaces and Interfaces*. (Springer Tracts in Modern Physics, 1992).

# Chapter 3:

## Ultra-Fast Laser Technology

Laser Technology in the CFN's Ultrafast Spectroscopy Lab

In the 60 years since the first creation of the laser, significant advances in technology have occurred which enable the generation of wavelength tunable ultrashort short (30fs), high energy pulses (3mJ) with very high duty cycles (Pulse Spacing/Pulse Width ~$10^{10}$). Here I'll briefly review the technology behind three components which enable the outstanding time resolution and spectral tunability of our pump-probe technique: 1) the Ti:Sapphire Oscillator 2) the Ti:Sapphire Regenerative Amplifier and 3) The Optical Parametric Amplifier.

The radiation wave length used in our system is 800nm, while the pulse duration is 150fs, which corresponds to 45μM in spatial extent. Thus we typically have about 60 full oscillations of the field within one pulse. The generation of ultrashort pulses requires the use of a lasing material which has a board fluorescence spectrum. The exact fluorescence bandwidth required is determined by our target pulse duration of 150fs. The relationship between the pulse duration and the minimum required bandwidth is determined by the shape of the pulse, and takes the form:

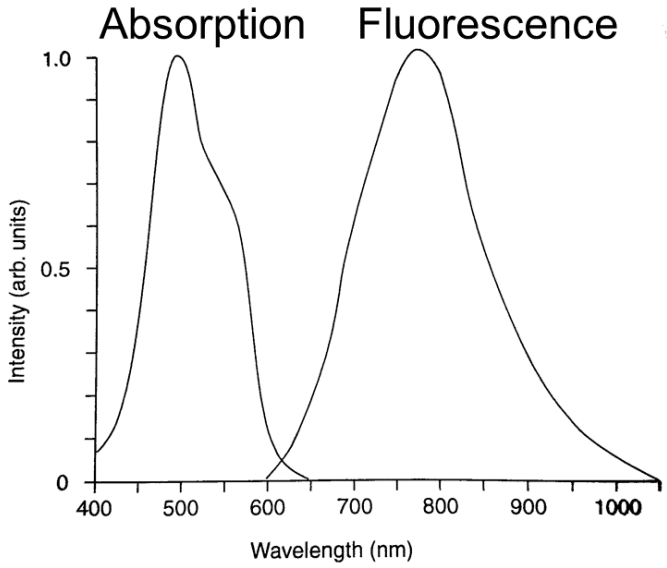


**Figure 1.** This figure shows the absorption and fluorescence of the Ti:Sapphire lasing rod in our Oscillator and Regenerative Amplifier. **This figure was taken from the user manual of the Tsunami oscillator.**

$$\Delta\omega\Delta\tau \geq 2\pi K$$

Where $\Delta\omega$ is the full width at half max of the angular frequency distribution, while $\Delta\tau$ is the full width half max of the pulse's temporal profile. K is a constant that depends on the precise temporal profile which the pulse and takes on. K has the value 0.441 for a Gaussian temporal profile, and 0.142 a Lorentzian. Thus to

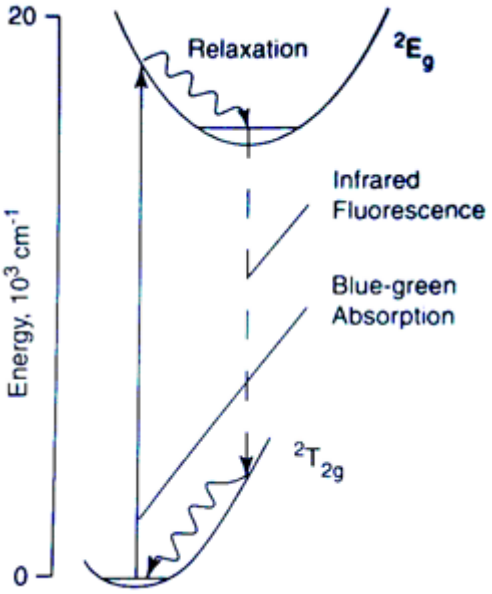


**Figure 2.** This figure shows the nuclear potential energy surfaces associated with the optical transitions in our Ti:Sapphire rod. **This figure was taken from the user manual of the Tsunami oscillator.**

achieve a 150fs Gaussian pulse requires 18.5THz of band width. At a wavelength of 800nm this corresponds to an intrinsic broadening 6.2nm. This corresponds to an energy broadening of about 10meV which ends up limiting the energy resolution of the pump in ultrafast experiments. Figure 1 shows the fluorescence spectrum of the Titanium-Sapphire rod used in our oscillator. It's bandwidth is more than broad enough to accommodate 150fs pulses. As shown in figure 1 the emission is greatly red shifted from the absorption, which is related the Frank-Condon effect[1]. In this situation the dipole matrix elements of the optical transitions of the $Ti^{3+}$ ions are strongly influenced by the nuclear coordinates of the $Al_2O_3$ surrounding host crystal. Therefor the highest probability transition from the ground state of the titanium atom is to a vibronic state with a significant vibrational contribution to the transition energy. After excitation, this vibrational energy relaxes and the electron and surrounding crystal relax to the lowest energy vibrational state consistent with the excited electronic state. The emission process is a mirror image of the absorption process, and the highest probability radiative transition downwards is to another highly excited vibrational state. Thus vibrational energy in the two transitions accounts for the red shift of the emission with respect to the absorption, as is shown in figure 2. The Ti:Sapphire rod is different from the original lasing mediums in the sense that the red shifted fluorescence implies population is not necessary to achieve gain.

The Ti:Sapphire Oscillator

In our Tsunami Ocsillator, the Ti:Sapphire rod is pumped with high energy continuous wave solid state diode operating at 532nm with 5W of output power. Lasing is seeded by the vacuum fluctuations of the longitudinal modes of the cavity. In order to achieve ultra-short pulses, a time varying loss is added to the cavity with an acousto-optic modulator. This loss is modulated at the round trip frequency of the cavity which is c/2L, where c is the speed of light, and L is the cavity length ($\omega_{\text{Round Trip}}$ is typically ~2πx80MHz). This effectively adds an additional loss to the non-mode-locked (ie non-pulsed) component of the intra-cavity field. After many round trips, the pulsed component of the field which is in phase with the modulator gets amplified, with all other components decreasing due to their increased round trip loss.

The Ti:Sapphire Regenerative Amplifier

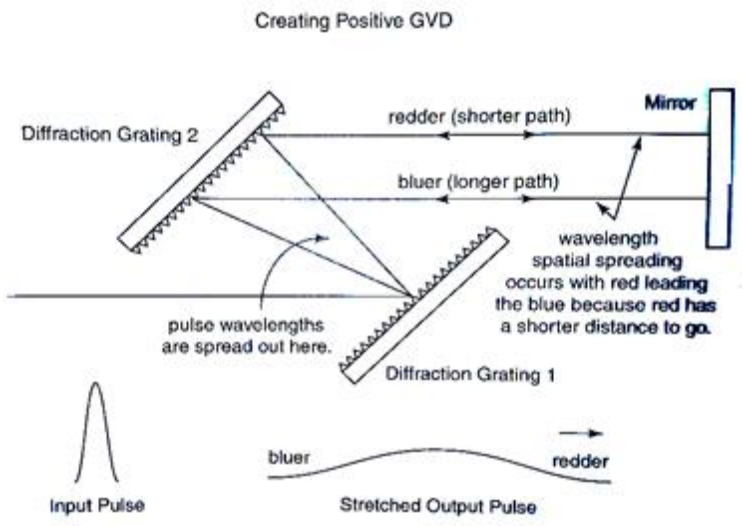


**Figure 3.** This figure depicts the concept behind the operation of the pulse stretcher in our regenerative amplifier. An optimized version of this is used in the real device which only utilizes one grating. **This figure was taken from the user manual of the Spitfire Regenerative Amplifier.**

The Ti:Sapphire oscillator creates pulses that are used to seed the Ti:Sapphire regenerative amplifier. However because of the pulses very short duration, directly amplifying the pulse to the desired energy will bring the peak power past the Ti:Sapphire rod's damage threshold of 10GW/cm$^2$. Therefore, to further amplify the pulses, their duration must be increased such that the peak power of the pulse is below the stated damage threshold at the desired pulse energy. This is the basis of the chirped pulse amplification (CPA) method. The pulse is first stretched out temporally, then amplified, then recompressed to the desired temporal length.

Figure 3 shows the operating principal of the pulse stretcher used in our regenerative amplifier. Briefly, the seed pulse from the oscillator (duration ~100fs) is directed at a diffraction grating pair. The first grating disburses the light, which means it causes the different wavelengths in the pulse to travel in different directions. Note that no temporal dispersion is introduced by the grating. The second grating re-collimates the beam but preserves the spatial separation of the different wavelengths. This collimated beam then hits a mirror at an angle such that the longer wavelength components travel a shorter optical path length than the shorter wavelengths components. The beam is then recombined by traveling the same path backwards. Because of the shorter optical path length traveled by the long wavelength components they will emerge first from the pulse stretcher, while the shorter wavelength components having traveled a longer optical path length emerge later. This gives rise to a positively "chirped" pulse (a pulse in which the lower wavelength components are at the front and the shorter wavelength components are at the back) whose temporal duration is significantly longer ($x10^4$) than the seed pulse.

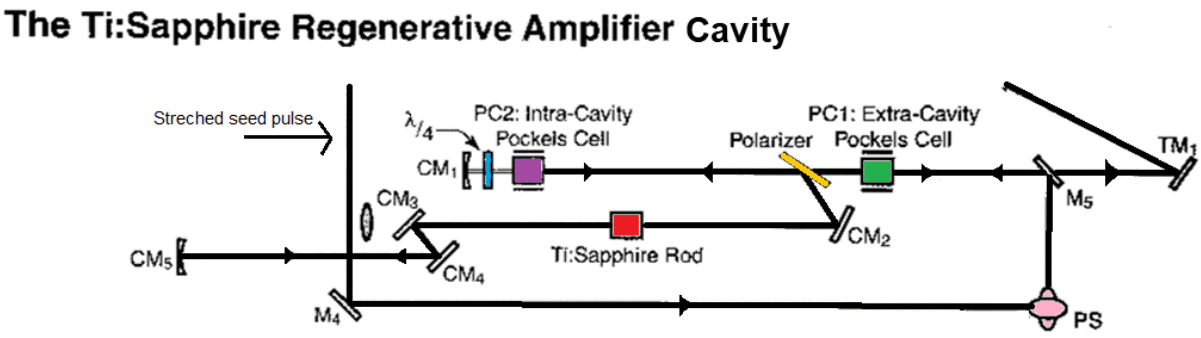


**Figure 4.** This figure shows a schematic of the cavity in our regenerative amplifier. The beam line of the CW laser pumping the Ti:Sapphire rod is not shown for clarity. **This figure was taken from the user manual of the Spitfire Regenerative Amplifier and modified for clarity.**

The seed pulses coming from the oscillator are separated by roughly 12 nanoseconds. After stretching the pulses by a factor of $10^4$ we have pulse duration of roughly 1.5 nanoseconds, which shows that the pulses remain spatially and temporally separated. This allows us to actively pick which pulses which are trapped in the amplifier cavity, and this is achieved with the help of the extra cavity Pockels cell in combination with a polarizer, as shown in green and yellow in

figure 4 respectively. A Pockels cell is an electro-optic modulator that can rotate the pulse's polarization depending on the voltage across it. A polarizer is an optical element that transmits light polarized parallel to its axis, while reflecting all light polarized perpendicular to it's axis. A polarizer sits at the entrance of the amplifier cavity. In conjunction with the Pockels, cell the polarizer can dynamically determine which pulses can enter and exit the cavity. The pulses coming from the stretcher are horizontally polarized, and are subsequently rotated to vertical using a polarization rotating periscope, shown in pink if figure 4. After the periscope the pulse passes through the extra-cavity Pockels cell shown in green. Depending on the voltage across it one of two things can happen. If the voltage across the Pockels cell is zero, the polarization of the pulse remains vertical and is subsequently rejected by a polarizer (shown in yellow) at the cavity's entrance. If the Pockels cell is in a high voltage state, the polarization of the beam is rotated back to horizontal in passing through the Pockels cell, and is subsequently allowed to pass through the entrance polarizer and enter the cavity. The pulse now encounters the intra-cavity Pockels cell λ/4 plate combination (purple and blue respectively). If the intra-cavity Pockels cell is off when the pulse enters the cavity, the beam will be rotated back to vertical by two passes through the λ/4 plate (one pass on the way in, and one pass after reflection from $CM_1$). The vertically polarized pulse cannot pass through the polarizer at the cavity's entrance, and thus reflects off of it, and becomes trapped in the cavity. The reflected pulse is directed at the Ti:Sapphire rod (shown in red) which is synchronously pumped by a frequency doubled pulse of an Nd:YLF laser (527nm 20mJ pulses 300ns 1kHz). In traveling through the rod twice, it picks up a factor of 3 or 4 in energy. After being reflected by the mirror at the cavities end and passing through the Ti:Sapphire rod once more, the pulse is then incident on the entrance polarizer. Up to this point, the pulses polarization remains unchanged and it is thus once again reflected from the entrance polarizer, and is directed back towards the Pockels cell-λ/4 plate combination. At this time if the Pockels cell is in a high voltage state, the pulse will experience four λ/4 rotations (two from the intra-cavity Pockels cell, 2 from the λ/4 plate), which will leave the vertical

polarization unchanged. In this case the pulse goes back to the lasing medium for another round trip. As long as the Pockels cell remains on the pulse will remain trapped in the cavity and will have it energy multiplied by a factor of 3 with each round trip. After 13 to 15 round trips the pulse will have been amplified by a factor of roughly $3^{13}$= 1,594,323, which turns oscillator's nanojoule pulses into milliejoule pulses. However, if the intra-cavity Pockels cell is turned off when the trapped pulse hits it, the pulse will experience 2 λ/4 rotations making it horizontally polarized, and it will exit the cavity. Thus when the pulse can no longer obtain gain from the Ti:Sapphire rod, the Pockels cell is turned off and the pulse is kicked out of the cavity. The pulse then encounters the compressor, where it squeezed back to 150fs, and exits the amplifier. These milliejoule pulses are split by a beam splitter, with one arm used to generate our white light probe, and the other used to pump the Optical Parametric Amplifier, which tunes the pulses wavelength, and is used for the pump pulse. Our regenerative amplifier is run at 1kHz, to achieve the pulse energies required of the experiment.

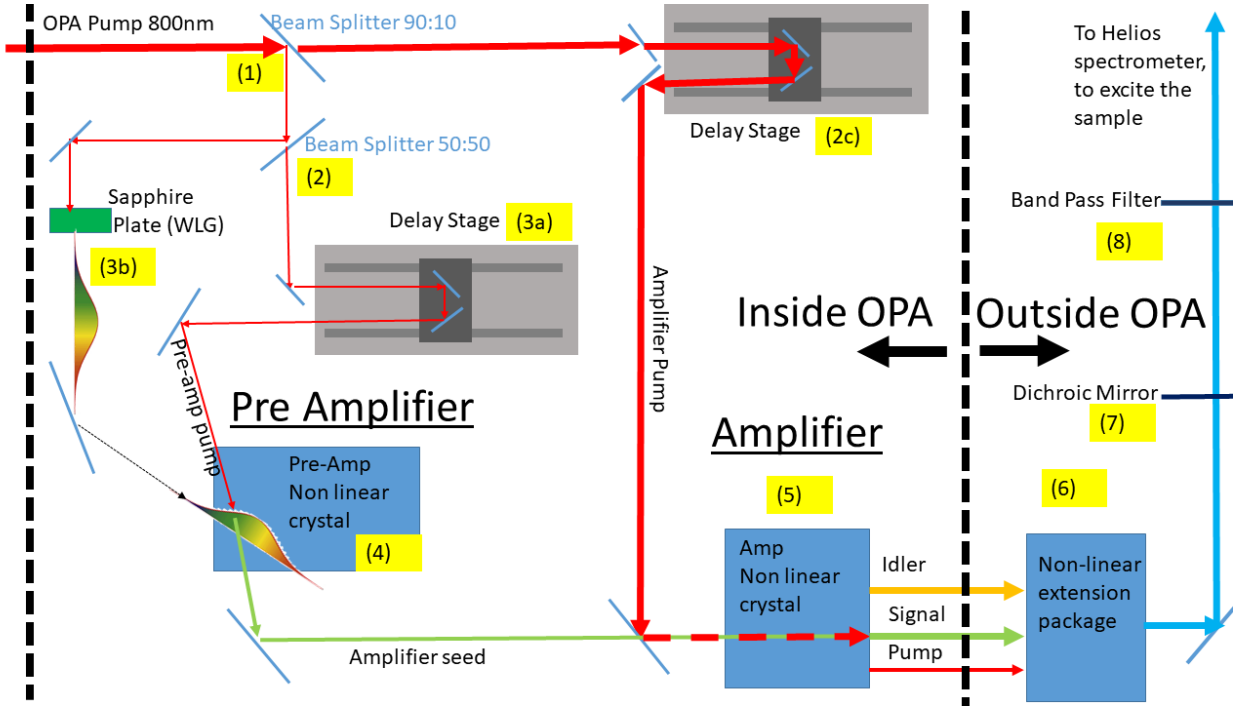


**Figure 5.** This figure illustrates the operating principals of our TOPAS-c optical parametric amplifier.

Optical Parametric Amplifier (OPA)

A schematic of our OPA is shown in figure 5. Optical Parametric Amplifiers make use of $\chi^{(2)}$ interactions in a nonlinear crystal to turn the pump pulse into a signal pulse and an idler pulse. The signal pulse is used to excite our sample. In our OPA the frequency conversion is achieved in two steps. First there is a pre-amplifier stage in which a seed pulse at the desired wavelength is generated by overlapping a white light pulse and a small portion of the pump beam. The energy of the seed pulse is generally about 0.5μJ. Next the amplification stage mixes the majority of the pump beam with the seed beam, which produces pulses of roughly 10μJ. This process will be described in more detail in the following. In the description of the operation of the OPA I will refer to optical elements by their numbers shown in yellow in figure 5.

Seed Generation- Pre Amplifier

As noted, when the pump beam enters the OPA it is split with the majority of the energy used in the amplifier stage, this first beam splitter corresponds to number 1. This beam is again split (2) with one portion incident on a sapphire plate which generates a white light continuum pulse (WLC) The WLC is a chirped pulse with a long temporal profile and a large spectral bandwidth(3b). The stability of the white light generation process depends strongly on the pump pulse's energy and cross sectional profile. If the energy is too high or too low this will lead to fluctuations in the power of the seed pulse, which ultimately leads to fluctuations in our pump beam. The other beam emerging from beam splitter (2) is sent down a delay stage (3a). These two beams are non-collinearly overlapped in the pre-amp nonlinear crystal (4) with the pre-amp pump pulse parametrically amplifying a portion of the WLC pulse. The WLC pulse is chirped and has a very long temporal duration compared to the pre amp pump pulse (150fs) which comes directly from the regenerative amplifier. Thus the pre amp pump pulse can only be spatially overlapped with a small portion of the WLC pulse, and this is the component of the WLC which experiences parametric amplification. The chirp of the WLC pulse implies that different spatial positions of the

WLC pulse have different frequencies. Thus by adjusting the spatial overlap (or equivalently the temporal overlap) of the pre-amp pump pulse and the WLC pulse, different frequencies can be parametrically amplified. The overlap between the pre amp pump and the WLC can be continuously varied using delay stage (3a), which can continuously tune the frequency of the seed pulse which results from the pre amplifier stage. We note many subtleties of the pre-amplification process. First, the pump and WLC are not collinear in the non-linear crystal. This allows the separation of the parametrically amplified signal (propagating collinearly with the WLC), and the pump. The collinear nature of the seed and the WLC is not reflected in figure 5 for clarity. In addition to the signal, there are other nonlinear process which give rise to distinct beams. There is the idler, the sum frequency of the signal and the pre-amp pump, and the sum frequency of the idler and the pre-amp pump. Due to the non collinear geometry, these are all spatially separated which allows one to pick the desired beam for the amplification step. Also, the delay line is actually on the WLC pulse which modulates it's timing with respect to the pre-amp pump pulse. This is not reflected in the figure for clarity. However, this implies that the timing of the pre-amp pump pulse and thus the seed of the amplifier stage has a relatively constant timing with respect to the amplifier pump pulse. Finally, we note that the pre-amp Nonlinear crystal (4) is mounted on a pre-calibrated rotation stage, which automatically adjusts the orientation of the crystal with respect to the incident beams to achieve phase matching for the desired parametric amplification wavelength.

Amplifier

As stated, the majority of the power passes the first beam splitter (1) and is directed down an additional delay line (2c). The Amplifier pump pulse and the seed pulse have to be well-overlapped temporally in the amplifier non-linear crystal (5) in order to achieve efficient energy conversion from the pump into the signal. The delay stage (2c) is used for fine adjustment of the the timing of the amplifier pump pulse to account for delay incurred in the seed pulse coming from

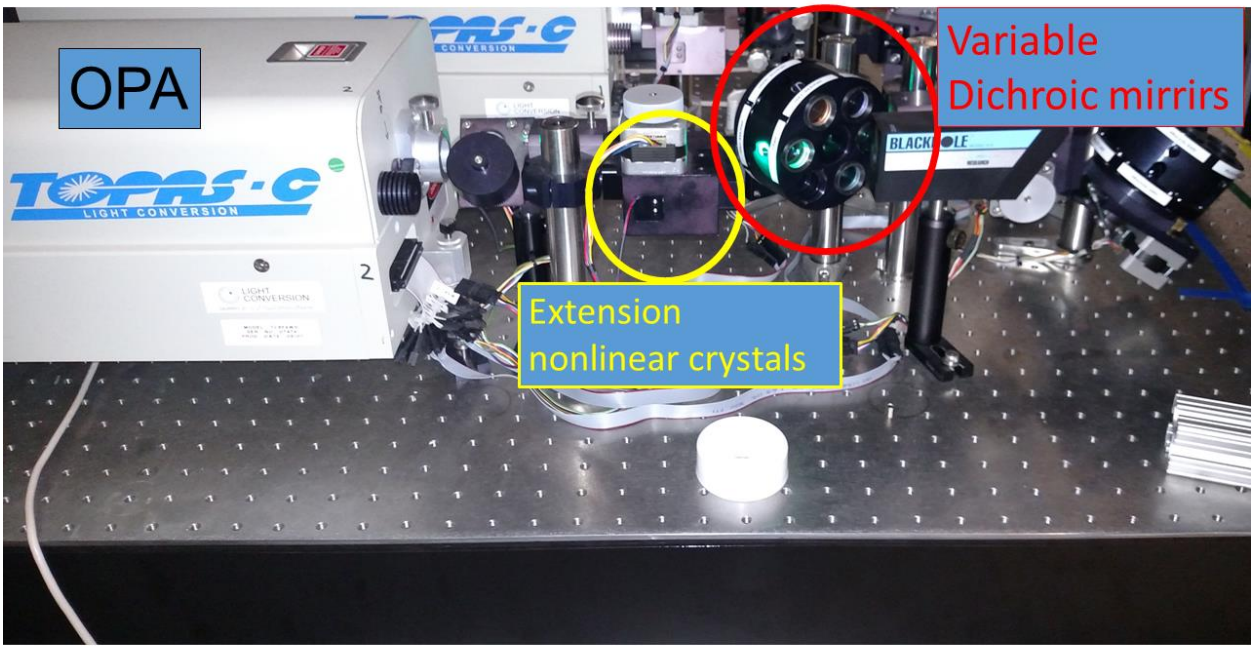


**Figure 6.** This figure shows a picture of the OPA in our lab, with the nonlinear extension package.

the pre-amp stage. Generally, this stage does note move during normal operation because as noted the pre-amp pump pulse, and thus the amplifier seed has a constant delay with respect to the amplifier pump. Again the amplifier nonlinear crystal (5) is mounted on a pre-calibrated rotation stage which is used to optimize the phase matching for the parametric amplification process with the desired wavelength.

Nonlinear extension package

In the amplifier non-linear crystal, the pump and seed travel collinearly, and thus the signal, idler and pump all emerge from the crystal collinearly as well. The pump still contains significant energy and we use this fact to extend the tuning range of the OPA system using a non-linear extension package (6). This package is a suite of $\chi^{(2)}$ nonlinear crystals, which perform sum frequency generation (SFG) between the signal and the pump or idler and pump. The system is also calibrated to perform second harmonic generation (SHG) on the signal or idler. However, because the pump generally has more energy than the signal or idler, the SFG process generally has a

higher energy output at the desired wavelength than the SHG process. The $\chi^{(2)}$ crystals in the nonlinear extension are mounted on a pre-calibrated rotation stage which allows the automated selection of the correct crystal, and automated adjustment of the crystals angle for phase matching. The OPA box and nonlinear extension package are shown in figure 6. After the desired wavelength has emerged from the nonlinear extension box, it still contains the pump, signal, idler and likely the second harmonic of the signal and the idler. Thus we use a dichroic mirror (7) to filter out the unwanted light, and direct this light at a beam stop (the 'black hole' seen in figure 6, but not shown in figure 5). Finally, to filter our any remaining unwanted light passing the dichroic mirror, we use a band pass filter. This concludes the pulse frequency conversion. The beam is now sent to the Helios spectrometer and is hence fourth referred to as the "pump pulse" because it is used to excite electrons and holes in our sample. We typically have about 10μJ pulses coming out of the OPA at 1kHz depending on the desired wavelength.


1. Moulton, P. F. Spectroscopic and laser characteristics of Ti:A120 3. *J Opt Soc Am B* **3,** 125–133 (1986).
2. Tsunami Mode-Locked Ti:Sapphire Laser, Users Manual. **Spectra Physics**
3. Spitfire Pro Ti:Sapphire, Users Manual. **Spectra Physics**
4. TOPAS-c Users Manual. **Coherent**

# Chapter 4:

## The Transient Absorption Spectrometer at the CFN

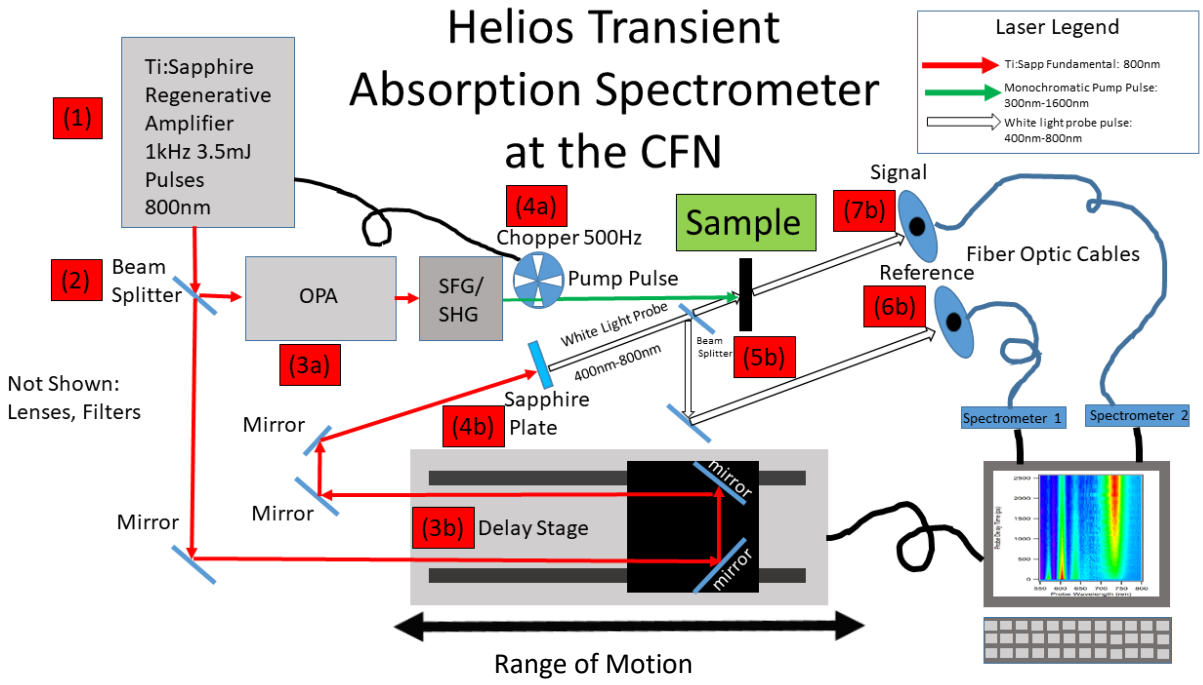


**Figure 1.** This panel shows a schematic of the transient absorption spectrometer used in my thesis experiments. Lenses and filters were left out for simplicity and clarity.

Transient Absorption Spectrometer at the CFN

Transient absorption spectroscopy is a time resolved a pump-probe optical technique. It measures how the transmission spectrum of a material changes as a function of time after being excited by a pump pulse. We physically interpret the transient absorption spectrum as reflecting the energetic distribution of photoexcitations in the material. Thus the transient absorption spectral kinetics contain information about the local electronic structure, dissipation processes, transport processes, and electronic temperature experienced by the photoexcitations. Throughout the description of the set up, I'll direct your attention to various parts of figure 1 by referring to the numbers that appear in red.

Transient absorption spectroscopy is based on a high powered, mode locked laser source. We use a Ti:Sapphire regenerative amplifier emitting 3.5mJ pulses of 800nm light at 1kHz (1). The operating principals of the regenerative amplifier are described in chapter 3. The first optical element encountered by output of the regenerative amplifier is a beam splitter which

divides the beam into two (2). The beam reflected from the beam splitter is used to generate the pump pulse, and is directed into an optical parametric amplifier (3a), whose operation is described in chapter 3 as well. The OPA utilizes parametric amplification change the λ=800nm pulse from the regenerative amplifier into a pulse with the wavelength desired of the pump pulse. When used in conjunction with the nonlinear extension, the range of accessible pump wavelengths is extended to 1600nm - 300nm. After the desired wavelength is achieved, the pump pulse is then synchronously chopped such that every other pulse is blocked (4a). The chopped beam is then used to photo-excite the sample material (labeled in green). The probe pulse is created using the beam transmitted at the initial beam splitter (2). This beam is directed down a variable delay line (3b), which consists of a retroreflective mirror mounted on a translation stage. This delay line functions to accurately and precisely introduce additional optical path length in the probe beam line, which is critical to our time resolution. The beam emerging from the delay line is then directed at a sapphire crystal (4b) which is used to generate a broadband pulse of white-light. The white light pulse is used to measure the transmission spectrum of the material with very high time resolution (~20fs). Before the probe pulse hits the sample it is again split (5b). The transmitted beam is used to probe the sample, while the reflected beam is used as a reference to eliminate noise contributions from the probe beam. The reference beam is collected by a fiber optic cable (6b), and disbursed in a multi-channel spectrometer. The probe pulse passes through the sample, and is collected by a fiber optic cable (7b), and is also dispersed in a multichannel spectrometer. This transmitted pulse carries with it a snapshot of the optical information of the material at the time the pulse passed through it. The spectrometers utilize diffraction gratings to disburse the probe pulse, which causes light with different wavelengths to travel at different angles inside the spectrometer. The disbursed light is directed at a 1024x1 pixel array which measures the light intensity at each wavelength I(λ). Using the probe and reference intensity spectra we can calculate the transmission spectrum: $T(\lambda)=I(\lambda)_{probe}/I(\lambda)_{reference}$.

Information about photo-excited carrier dynamics is obtained tracking how the transmission spectrum changes in time after the pump pulse excites the sample. If the pump pulse and probe pulse travel the same optical path length, they arrive at the sample at the same time. This condition determines the t=0 of the experiment. The arrival time of the probe can be delayed relative to the pump with high accuracy and precision by increasing the optical path length of the probe. This is achieved introducing a retroreflective mirror on a translation stage into the probe beams path (3b). By adjusting the position of the stage we can introduce a specified additional amount of path length to the probe beam. For every 1mm moved by the stage, the probe arrival time is delayed by 6.6 picoseconds. It is typical that delay stages can precisely position themselves with the accuracy of less than one micron, which corresponds to 6.6femtoseconds. Thus a typical delay stage can offer more than enough accuracy and precision to obtain a time resolution of 150fs. High precision stages can yield time resolution on the scale of hundreds of attoseconds ($10^{-16}$s).

As noted the, the pump beam is chopped synchronously with the regenerative amplifier and thus only excites the material at 500Hz, while the probe beam is un chopped and measures the transmission of the sample at 1kHz. Thus we measure the excited state transmission spectrum and the linear transmission spectrum at 500Hz each. We calculate $\Delta A(\lambda) \equiv -\log\frac{T(\lambda)_{Excited\ Sate}}{T(\lambda)_{Linear}}$ at 500Hz. We delay the discussion of the physical significance of $\Delta A(\lambda)$ until a later section. In practice we specify the pump-probe delay time using the translation stage and average $\Delta A(\lambda)$ until the desired signal to noise is achieved, then move to the next time point and repeat the procedure.

The integration time per point has a maximum value of 10s in the Helios software. To achieve higher signal to noise ratios, we took multiple consecutive kinetic scans and averaged them together. This technique has the additional advantage of allowing us to track systematic and

irreversible changes in the spectrum or kinetics, which are signs of beam induced sample damage.

For completeness we note that the pump beam of a 1kHz TA spectrometer is composed of relatively high energy monochromatic pulses ( $\Delta\lambda$~10nm, $E(\lambda)$~0.01μJ/nm). The energy of the probe pulse is typically much smaller and broader spectrally ($\Delta\lambda$ ~ 400nm, $E(\lambda)$ ~ $7.5x10^{-6}$ μJ/nm). The pump pulses typically photo excite a carrier density between $10^{17}cm^{-3}$-$10^{19}cm^{-3}$ or a fluence of roughly $10^{12}cm^{-2}$-$10^{14}cm^{-2}$. In this range of carrier densities $\Delta A_{max}$ is typically between $10^{-3}$-$10^{-1}$. Satisfactory signal to noise can be achieved on the low end of the density distribution by integrating roughly 4 seconds at each pump probe delay. There are typically 300 points per scan, implying an acquisition time of around 20 minutes. However, observing $\Delta A$ signals around $10^{-4}$ and carrier densities around $10^{16}cm^{-3}$ takes significant effort and extensive signal integration. Typical carrier densities excited in solar cells are closer to $10^{15}cm^{-3}$-$10^{16}cm^{-3}$. Thus kHz TA spectrometers are meant to study much higher density phenomena than what is directly applicable in solar energy devices, and significant effort was expended to make this set up amendable to these low fluences.

## Laser power DAQ and Stabilization

The experiments I conducted for this thesis had to be done at a small absorbed fluence. In order to achieve a reasonable signal to noise, I needed to take about 12 scans, each scan with 250 points, using an integration time of 10 seconds per point. In total this equals about 8 hours and 30 minutes to obtain one piece of data at one absorbed fluence. To get a good feeling for the kinetics, one has to vary the absorbed fluence by at least a factor of 20. All together each data set took around 24 hours to complete with some taking significantly longer. Approximately 10 full data sets were required for the analysis in this thesis. However, the stability of the pump laser was very poor in the lab due in part to fluctuations in temperature. To get consistent data the pump power had to be stabilized.

Figure 2 shows the set up used to measure the time variation of the pump power. The first element in the set-up is an iris which is set to ~500μm in diameter, which was significantly smaller than the size of the incoming pump beam ~3mm. This iris is important because in addition to fluctuations in the overall power of the pump beam, there are also fluctuations in the pointing of the beam. In the context of our experiment, these two types of fluctuations both distort our data in a similar way, because if the pump beam drifts away from the probe beam an effective decrease in pump power is measured in the TA signal. However, using an iris which is much smaller than the pump beam itself ensures that no fluctuations in beam pointing occur within the spectrometer. After the iris the beam is incident on a silicon photodiode, which generates a signal at 500Hz whose magnitude is proportional to the pump power. This signal is then routed to a box-car gated

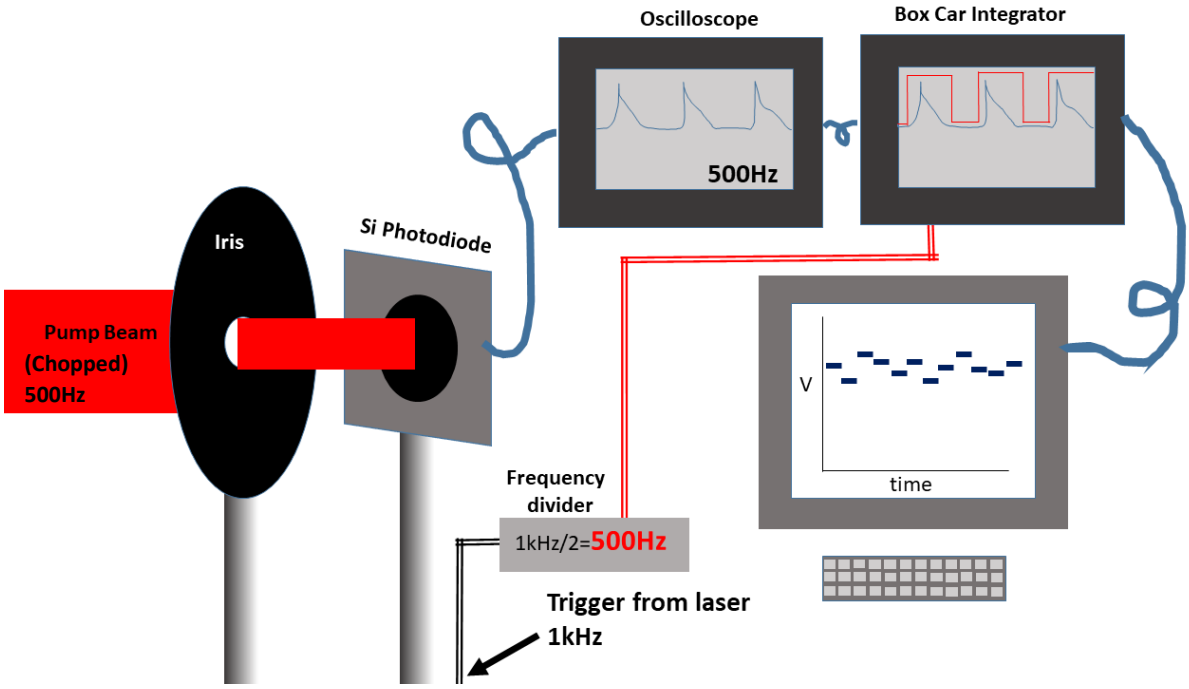


**Figure 2.** This figure shows the set-up utilized to track the real time power of the pump pulse.

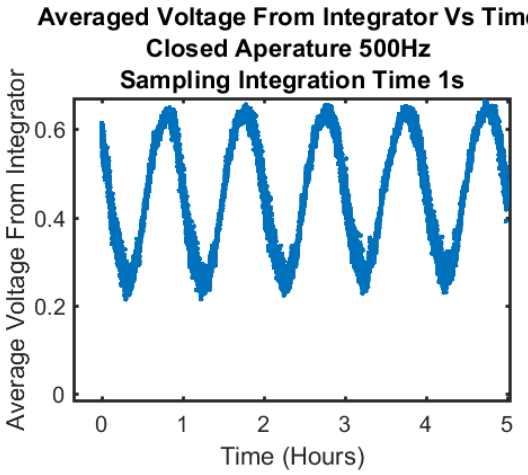


**Figure 3.** This figure shows the pump power measured vs time with the set up in figure 2.

integrator. The integrator integrates the signal from the photodiode across the gate shown in figure 2. As the gate is only about 10ns, the timing between the pulse and the gate has to be accurately prescribed to ensure they overlap. This is achieved by triggering the gate on the integrator using the synchronizing TTL signal from the regenerative amplifier. However, the frequency of the trigger from the regenerative amplifier is at 1kHz, while the chopped beam produces a signal in the photodiode at 500Hz. Thus a digital frequency divider is used to account for this difference. When the trigger for the gate is properly aligned to the photodiode signal, the integrator outputs a constant voltage proportional to the integrated signal for the roughly 2ms until the next trigger is received. The voltage from the integrator is sampled at 50kHz by an analog to digital converter, which reads the signal into the computer. In this way the power of the individual pulses can be read out by the computer. The result of this procedure is shown in figure 3. Note that each point in figure 3 represents the signal averaged over 500 pulses corresponding to an integration time of one second. Due to the small diameter of the iris compared to the beam size, this figure represents large fluctuations in the pointing of the beam on the time scale of hours.

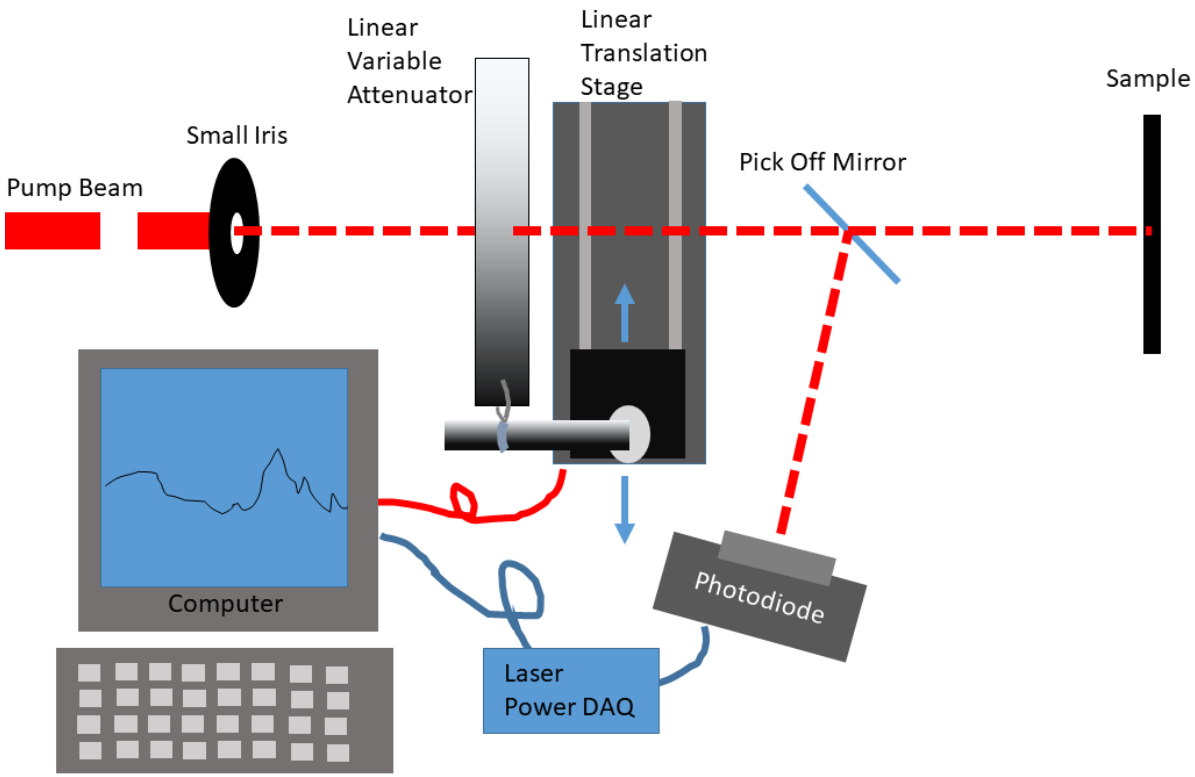


**Figure 4.** The schematics of the PID control loop power stabilization set up. Error signal read out is achieved using a pick off mirror and a photodiode to measure the power in real time. Control over the beam power is achieved by mounting a variable linear attenuator on a translation stage.

These fluctuations in the beam pointing were found to correlate with temperature fluctuations in the lab which are actively monitored and recorded by the facilities manager here at the CFN. We note that the room which houses the ultrafast spectroscopy facility at the CFN was not originally designed to be a laser lab, and thus the temperature and humidity controls are less stringent than one would desire of a dedicated laser facility. The power fluctuations shown in figure 3 are definitely an over estimate of the importance of pointing fluctuations because the beam was not centered on the iris in this measurement. None the less, these fluctuations still represent a variation in pointing which is a significant fraction of the beam diameter.

The price of stabilizing the beam pointing with the iris are the large power fluctuations shown in figure 3. In reality these fluctuations are always present but they cannot be measured with a large area photodetector, because the detector averages the power over the illuminated

area, making it insensitive to small drifts in pump pointing. To counteract the power fluctuations which result from the pointing drift, a PID control loop was developed in LabView, and the set-up is shown in figure 4. This loop utilizes a variable linear attenuator on a fast translation stage to adjust the power incident on the sample in response to the voltage measured on the photodiode.

In practice the desired power is measured with a large area power meter (after the iris) , and the corresponding photodiode voltage is input into the control loop as the set point. After this, the program is run and the linear translation stage dynamically adjusts the position of the stage-attenuator combination to account for the long term drifts in power read out by the photodiode. Together, the stage and photodiode combination are capable of feeding back at 50Hz, but in practice this does not lead to the smallest RMS deviation from the set point, and actually introduces noise into the signal. This occurs because shot to shot variation in the pulse power is significant and unavoidable. The PID parameters and the feed-back bandwidth were empirically adjusted to achieve the smallest RMS deviation from the set point. In this way we achieved long term power stability with a relatively small RMS deviation of +/- 10% at one second integration time.

The power stabilization loop was used in acquiring all of our data, and is now employed by virtually all users in the ultrafast spectroscopy lab at the CFN. This loop was incorporated into another program which utilizes a power meter to calibrate the photodiode voltage. Specifically, this program measures the pump power, the transmitted power, the reflected power, and the beam spot size in-situ which allows the prescription of the absorbed fluence (photons/$cm^2$) before the measurement. Furthermore, this program allows one to obtain a batch of TA measurements at various absorbed fluences. For each measurement, the absorption information is used to calculate photodiode set point corresponding to the desired fluence. After the correct set point is achieved this program then triggers the Helios software take a full measurement of the TA spectral kinetics. In this way large data sets can be autonomously and consistently collected, over a period

of days, with no interaction from the user. Together with homemade data analysis software developed in Matlab, the process of acquiring and analyzing data was greatly streamlined. This program enabled the acquisition of huge amounts of data using the TA spectrometer in the limited

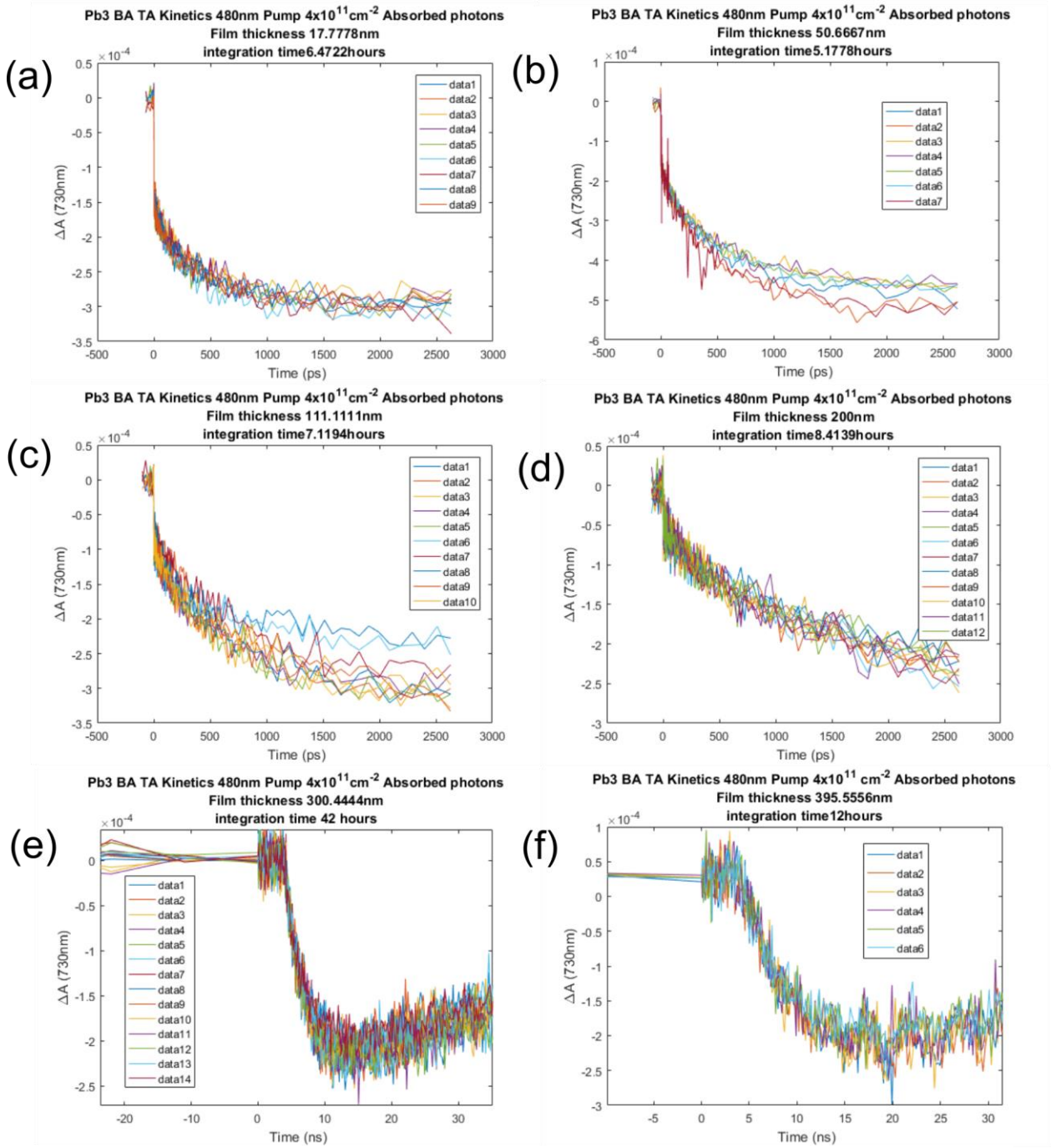


**Figure 5.** This figure shows the differential absorption kinetics obtained using the described program on the set of films which are the subject of this thesis.

time which was allotted to me for use.

Results of the Power Stabilization Loop and Long Term Sample Stability

Figure 5 shows the differential absorption kinetics at 730nm obtained using the power stabilization and calibration program described in the previous section. Details of the interpretation of these kinetics will be given in chapter 5 on the analysis of the TA data. The legends in figure 5 indicates the chronological order of the measurements. The typical measurement time for these figures was 8 hours, but the measurement time ranges as high as 42 hours in figure 5e. Note that the pump-probe delay time axis in figures 5(e,f) is in nanoseconds rather than picoseconds.

Figure 5 shows the magnitude of these features is on the order of $10^{-4}$, and reasonably consistent between the different film thicknesses measured, with the notable exception of figure 5b, which appears appreciably larger than the rest. We note that the calibration procedure is significantly less accurate at small pump powers (~1μW), as it depends strongly on properly taking into account all of the background sources of light., and we attribute the differences in signal magnitude to improper calibration at low absorbed fluence. Thin film interference does not appear to have a big impact on our measured signals as this would result in a strong modulation in the line shape across the spectral band used for the probe pulse (400nm-800nm), which is not observed. The lack of this effect can be attributed to surface roughness on the

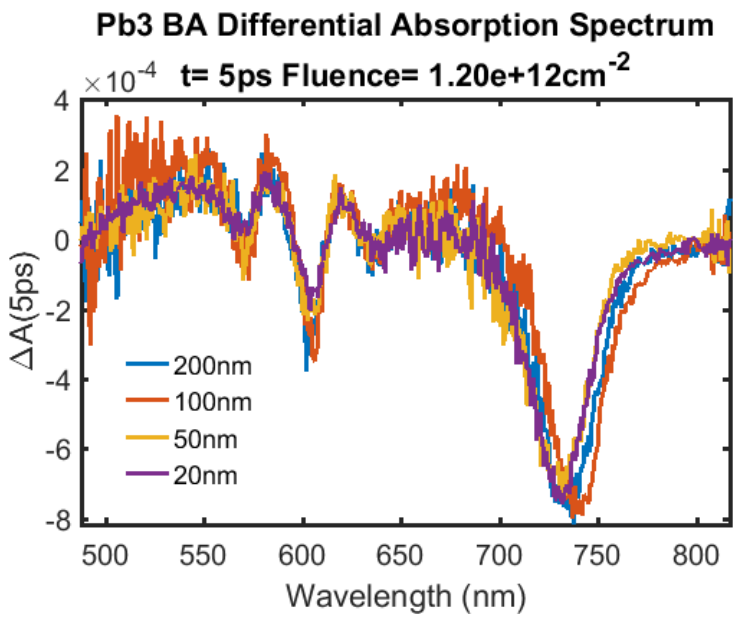


**Figure 6.** this figure shows the differential absorption spectrum at 5ps measured on films with four different thicknesses. All of these films were excited with a calibrated absorbed fluence of $1.2x10^{12}cm^{-2}$.

sample surface which is found to be significant in AFM images (shown in 6). To this effect, figure 6 shows the calibration procedure works much better a 3x higher absorbed fluence, while all of the spectra look very similar. The slight shift of the peak at 730nm to larger wavelengths with increasing film thickness may be a result of thin film interference, however figure 6 shows this effect is small and does not affect the magnitude of these features. Finally, there do appear variations in the kinetics within the panels in figures 5b and 5c. All scans within each panel are supposed to be identical apart from the noise. The differences in kinetics appear to be associated with random periods of extreme laser instability, which degrades the performance of and PID control loop. Such periods of extreme instability we typically observe when the temperature and humidity of the room change, which impacts the stretcher and compressor of the regenerative amplifier and translates into instability in the output of the OPA. Importantly, these differences in kinetics seen in figure 5b and 5c and do not have a consistent chronological trend. On the other hand, in figure 5e there is a 20% decrease in the signal magnitude over the 42 hours that this data was acquired. However, this appears to result of the sample rather than the variation of the pump power.

The Relationship Between $\Delta A(t,\lambda)$ and the Film Optical Constants

Due to the lack of interference phenomena observed in our samples, the intensity transmission spectrum of our samples (defined as $T(\lambda)=I(\lambda)_{probe}/I(\lambda)_{reference}$ in section 1) as can be approximated as $T(\lambda)=T_0e^{-\alpha L}$, where $\alpha=4\pi[Imag\{\tilde{n}\}]/\lambda$, and L is the film thickness. $\lambda$ is the wavelength of the radiation, and Imag{ñ} is the imaginary part of the complex refractive index. Absorption of the pump beam slightly modifies the complex refractive of the material. Thus $\alpha_{Pump\ On}= \alpha_{Pump\ Off} +\delta\alpha$, where $\delta\alpha$ is the pump induced change in absorption coefficent. Using the definition of $\Delta A(t,\lambda)$ given in section earlier:

$$\Delta A(\lambda,t) \equiv -\log\frac{T(\lambda)_{Excited\ Sate}}{T(\lambda)_{Linear}} = -\log\frac{T(\lambda)_0 e^{-(\alpha+\delta\alpha)L}}{T(\lambda)_0 e^{-(\alpha)L}} = -\log\left(e^{-\delta\alpha L}\right) = \delta\alpha(\lambda,t)L$$

Thus ΔA(t,λ) is directly proportional to the change in refractive index. In the above I have omitted a contribution to ΔA(t,λ) which comes from $\delta T_0$, the pump induced change in the Fresnel transmission coefficient of the air-film interface. This contribution tends to distort the shape of the ΔA(t,λ) which means that quantitative analysis of the TA line shape is generally not possible without taking into account this contribution. $\delta T_0$ is related to the change in the real and imaginary part of the refractive index. However, both of these changes are proportional to each other (in magnitude, not spectral shape), because they come from the same physical origin. Thus the contribution to ΔA(t,λ) from $\delta T_0$ does not affect the spectral kinetics. The reasoning employed in this thesis is mostly based on kinetic data rather than line shape data. When reasoning based on line shape is employed, it is done qualitatively.

The Physical Origin of $\delta\alpha(\lambda, t)$

The general description of the interaction between semiconductors and electromagnetic radiation requires the full force of many body quantum mechanics, which is far beyond the scope of this thesis. Therefor I'll briefly review the description of light's interaction with semiconductors which is relevant to the understanding of the experiments which make the body of this thesis. The absorption of light by direct band gap semiconductors is accomplished predominantly by moving electrons from the mostly full valance band into the mostly empty conduction band, while conserving the energy of the semiconductor + electromagnetic field system. This result can be derived from a time dependent perturbative treatment of the electromagnetic wave interacting with the quantum mechanical system of electrons in the semiconductor. The number of such upward transitions per unit time is given by fermi's golden rule[1]:

$$R_{cv} = (\pi/2\hbar)E(\omega)^2 \sum_k |P_{cv}|^2 \delta(E(k)_c - E(k)_v - \hbar\omega)$$

The field is composed of photons. Thus for every upward transition in energy experienced by the electronic system the field loses energy equal to that of the photon $\hbar\omega$. Therefor the energy loss

per unit time per unit area experienced by the field

$$\frac{dI}{dt} = -R_{cv}\hbar\omega = -I\left(\frac{\pi}{2\hbar}\right)\sum_k |P_{cv}|^2\delta(E(k)_c - E(k)_v - \hbar\omega) = \frac{dI}{dx}\frac{dx}{dt} = -\frac{c\alpha I}{n}$$

Thus we have the equality

$$\alpha = \left(\frac{n\pi}{2\hbar c}\right)\sum_k |P_{cv}|^2\delta(E(k)_c - E(k)_v - \hbar\omega)$$

The imaginary component of the refractive index thus depends on $P_{cv}$ which is related to the strength of the coupling between the conduction band and valance band state induced by the field, and the quantity $\sum_k \delta(E(k)_c - E(k)_v - \hbar\omega)$ which is called the joint density of states, and it is equal to the number of possible electronic transitions upward in energy. If the number of upward transitions at a particular frequency is N, we can then write $\alpha$=N$\left(\frac{n\pi}{2\hbar c}\right)\langle|P_{cv}|^2\rangle$ where the brackets denote averaging $|P_{cv}|^2$ over all possible transitions. Thus is the simplest case:

$$\delta\alpha = \delta N\left(\frac{n\pi}{2\hbar c}\right)\langle|P_{cv}|^2\rangle$$

and we have the physical interpretation that a change in the absorption coefficient can result from a change in the number of electronic transitions upwards in energy. When photo-exciting a semiconductor the population of excited electrons and holes relax to the band edge and occupy these states until they decay radiatively or otherwise. Due to the Pauli-exclusion principal an occupied state in the conduction band is not available for subsequent transitions. Thus in response to photoexcitation we obtain a change in the number of allowed transitions between the conduction band and the valance band, and this change is directly proportional to the population. In this treatment we have neglected the possibility of stimulating downwards transitions of photoexcited electrons in the conduction band into the valance band. A more rigorous treatment shows that this contribution combines additively with the one derived, and has exactly the same magnitude. This is based on the equivalence of the Einstein ‘A’ and ‘B’ coefficients for absorption and stimulated emission. Thus adding a factor of two to the above equation one obtains the

correct expression describing how the absorption coefficient changes in response to a photo-excited population of electrons and holes:

$$\delta\alpha = 2\delta N\left(\frac{n\pi}{2\hbar c}\right)\langle|P_{cv}|^2\rangle$$

We note that in the case that δN=N/2 (the photo-excited population is equal to half the total number of transitions) we find that the absorption coefficient vanishes. This describes the phenomenon of population inversion. Any photoexcited carriers which is excited in addition to N/2 actually amplify the field as it travels through the semiconductor, a process which is known as light amplification by stimulated emission of radiation, and is the basis of the laser technology which is leveraged in both the Ti:Sapphire oscillator an the Ti:Sapphire regenerative amplifier we use in our lab. We note that pump induced changes in the oscillator strength of the transition give rise to a nonlinear change in the absorption coefficient with excited fluence and therefor can be mostly ignored.

Thus the physical interpretation of ΔA(λ,t) and δα(λ,t) in our data is reasonably clear. ΔA(λ,t) is proportional to the number of photoexcited carriers occupying transitions associated with the wave length λ at the time t after photo excitation. Although the treatment is different in the case of excitons, the result is the same. Thus transient absorption spectral kinetics tell us about how the populations of photo excited electrons and hole distribute themselves over the optically active states of the excited material, and how these populations change in time.

Processes Occurring After Photoexcitation of a Semiconductor

In order to give proper context to our measurements it is important to speak of the typical processes and the associated time scales that are observed after the photoexcitation of a direct bandgap ionic semiconductor such as Gallium Arsenide[2]. The following discussion is based on reference 2.

Following excitation by an ultrashort laser pulse (like the ones used in our experiments) there are four physically distinct though temporally overlapping regimes that occur before the semiconductor can return to thermodynamic equilibrium. The first physical regime is characterized by coherent polarization. In this regime the electrons continue to quantum mechanically oscillate at the driving frequency of the field even after it has left the material. In the case of an inhomogeneously broadened transition this oscillation continues roughly until the dephasing time of the oscillators is reached, but the macroscopic polarization is destroyed immediately after the pulse leaves the material. This is because the phases of the various transition evolve at slightly different rates, and thus destroy the polarization at a time $\hbar/\Delta E_{inhomogeneous}$ which is smaller than the pulse duration if the inhomogeneous broadening is larger than the pulse bandwidth. A linear relationship between density and dephasing rate was observed in a 12nm single GaAs Quantum well at 2K[3]. Scaling the dephasing rate of free carriers to the lowest densities used in our experiments yields a carrier-carrier dephasing time of about 250fs. This dephasing time is similar to the phonon dephasing time of 100fs measured at room temperature for the excitons in GaAs Quantum wells[4].

During and after the dephasing process the carriers are in a non-thermal regime meaning that their distribution cannot be characterized by a quasi-temperature. Again scattering process between carriers, and with phonons thermalizes the carriers towards a Maxwell Boltzmann distribution[5]. Once thermalization has occurred (~1ps) we are in the hot carrier regime, in which the electron and hole populations are in thermal equilibrium with each other, but are out of equilibrium with the lattice. Importantly, because of thermal equilibrium has been established in the electronic population, all electronic states locally available to the carriers are occupied with the appropriate Boltzmann factors weighing their occupation. Thus in this regime the TA spectrum should reflect all optically active electronic states that are locally available to the photoexcitations. This fact will figure prominently in the analysis of our TA data. Because of the lack of equilibrium

with the phonon system, this regime is characterized by a one way transfer of energy from the electronic system to the phonon system. Because of symmetry, energy and momentum conservation, the electrons and holes typically interact with a few specific phonons which may take a substantial amount of time to decay. Thus this regime can be characterized by large non equilibrium phonon populations. The phonon populations can be so large and persistent that phonon reabsorption by the electrons and holes can compete with phonon emission. This situation can be identified by an electronic cooling time that depends strongly on excitation density. Such a situation is called a hot phonon bottle neck, and has recently been observed in $MaPbI_3$, the prototypical hybrid organic-inorganic perovskite semiconductor. In this thesis we report the observation of a hot phonon bottleneck in $Ba_2Ma_2Pb_3I_{10}$ as well, which is a layered derivative of $MaPbI_3$.

Finally, after the electronic population cools to the temperature of the lattice (~100ps) we enter the isothermal regime. This regime is characterized by an excess of electrons and holes compared the thermal equilibrium. The observed kinetics in this regime mostly reflect radiative and non-radiative recombination.

1. Yu, P. Y. & Cardona, M. *Fundamentals of semiconductors: physics and materials properties*. (Springer, 2010).
2. Shah, J. & American Telephone and Telegraph Company. *Ultrafast spectroscopy of semiconductors and semiconductor nanostructures*. (Springer, 1996).
3. Honold, A., Schultheis, L., Kuhl, J. & Tu, C. W. Collision broadening of two-dimensional excitons in a GaAs single quantum well. *Phys. Rev. B* **40,** 6442–6445 (1989).
4. Knox, W. H. *et al.* Femtosecond Excitation of Nonthermal Carrier Populations in GaAs Quantum Wells. *Phys. Rev. Lett.* **56,** 1191–1193 (1986).
5. Oudar, J. L., Hulin, D., Migus, A., Antonetti, A. & Alexandre, F. Subpicosecond Spectral Hole Burning Due to Nonthermalized Photoexcited Carriers in GaAs. *Phys. Rev. Lett.* **55,** 2074–2077 (1985).

# Chapter 5:

## GIWAXS/GISAXS Analysis

Grazing Incidence Wide/Small Angle X-Ray Scattering (GIWAXS/GISAXS) Characterization of Spin Coated n=3 RPP Thin Films

Studies of RPP thin films suggest that the macroscopic alignment of their [101] planes parallel to the substrate plays an important role in their exceptional performance as active layers in photovoltaic devices[1–3]. X-ray diffraction studies of these materials all seem to conclude that the material is phase pure[1,3,4] (containing close to a single n value). However, this has been questioned because the peaks characteristic of the layer spacing [0 k 0] are obscured when the crystals are oriented in the [101] geometry. Furthermore, the absorption spectra of these films appears to contain contributions from the primary excitons of other layer thicknesses, which is true in our films as well. Based on optical and device data a number of groups have suggested an energy funnel architecture in the film, in which the layer thickness increases towards the front of the film, eventually terminating with the n=∞ phase on the surface[5,6] ($MaPbI_3$). Although an intriguing and potentially technologically important prospect, there is no *direct* experimental evidence supporting such an architecture. A number of open questions regarding the structure of these films exist. In particular: How similar is the films crystal structure to that of the single crystal n=3 RPPs from which they are derived? Is there evidence of disorder or distortions compared to the single crystal structure? Is there any evidence for an energy funnel architecture? And finally, what's the mechanism behind the alignment of the crystal slabs perpendicular to the substrate? Therefore, to properly understand the composition of our films and give context to our optical studies, we performed GIWAXS and GISAXS as a function of incident angle on a number of hot cast RPP films with varying thickness. We also investigated the structure of an RPP thin film deposited with a post annealed technique for reference.

Comparing the Observed Scattering Pattern to That of the Single Crystal RPP Structure: Structural Refinement Analysis

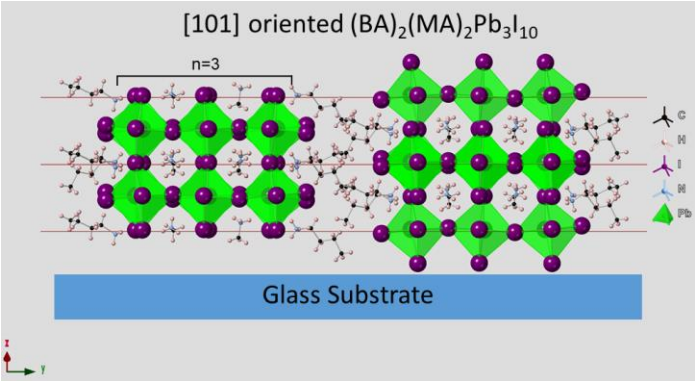


Figure 1. This figure shows the single crystal n=3 RPP structure in the orientation we expect in our film. We view the structure from the [10-1] direction. The red lines are the [101] planes which we expect to be parallel to the glass substrate.

Figure 1 shows the single crystal n=3 RPP structure in the [101] orientation. This structure was obtained from Stoumpos et al[7] who inferred it based on single crystal x-ray diffraction data. To obtain the thin films used in our experiments, purified single crystals are completely dissolved in solvent and then are spin coated onto glass substrates. We note that the crystallization conditions under which the single crystals are formed very different from those in which and the spin coated films are formed.

Figure 2a shows the observed GIWAXS pattern obtained on a 400nm hot cast n=3 RPP thin film. Note that $Q_z$ represents the out of plane component of the scattering vector, while $Q_r=(Q_x^2+Q_y^2)^{1/2}$, is the magnitude of the in-plane component of the scattering vector. The pattern in figure 1a displays sharp and intense Bragg peaks reflecting the highly crystalline nature of our films. The red open face circles on in figure 2a represent the intensity weighted reciprocal lattice of the structure and orientation in figure 1 (single crystal n=3 RPP). Generally speaking, the agreement is very good and it appears that we have roughly the correct unit cell dimensions.

Typically, when performing x-ray diffraction experiments on mono crystalline materials only one set of Bragg peaks can fulfil the Bragg condition for a given lattice orientation with respect to the beam. However, figure 2a shows we observed every peak in the predicted reciprocal lattice for an n=3 RPP single crystal (and only one peak that can't be indexed in this structure shown in

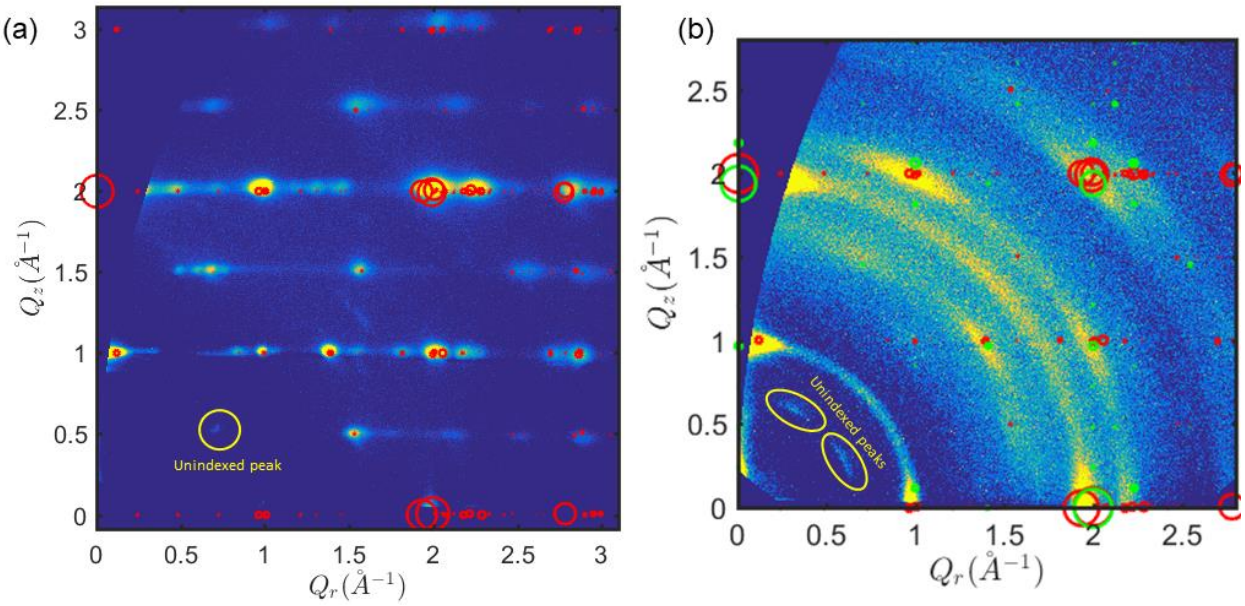


**Figure 2.** Panel a shows the measured GIWAXS scattering pattern of a 400nm hot cast n=3 RPP thin film. The red circles are the intensity weighted reciprocal lattice of the single crystal n=3 RPP in the [101] orientation. Panel b shows the measured GIWAXS pattern obtained on a 200nm Post annealed RPP thin film.

yellow). Thus, even though we have strict crystalline order in the out of plane direction, our film contains every in-plane grain orientation, which enables the fulfilment of the Bragg condition for every peak in reciprocal space. The latter is typical of spin coated polycrystalline films while the former is quite unusual. The only planes of the reciprocal lattice which we cannot measure (in range of our detector) lay exactly parallel to the substrate, such as the [101] and [202]. In this case wide angle scattering cannot fulfil the Bragg condition, and this is represented in our data by the blank wedge at starting at the origin and expanding up the $Q_z$ axis, easily seen in figure 2b.

Figure 2b shows the observed scattering pattern obtained on a post annealed n=3 RPP thin film 200nm thick. The post annealed GIWAXS pattern exhibits diffuse arcs of scattering intensity typically observed in polycrystalline spin coated thin films. These arcs reflect the distribution of lattice orientations of the various crystalline grains in the film. These arcs are noticeably absent in the hot cast films GIWAXS pattern confirming that in the out of plane

direction, hot cast films appear to scatter as single crystals. The red and green open face circles in figure 2b are the intensity weighted reciprocal lattice of single crystal n=3 RPP in the [101] orientation (layer stacking perpendicular to substrate, same as figure 2a) and the [010] (layer stacking parallel to substrate) orientation respectively. Only 2 peak in this scattering pattern that appear unrelated to the perovskite structure which appear at $|Q|\sim0.67Å^{-1}$ which corresponds to a periodicity on a length scale of 93Å. These peaks likely represent a long wavelength distortion of the unit cell, although it's not clear exactly what they correspond to.

Our n=3 RPP film appears highly crystalline, however most of the observed peaks in figure 2a could be equally well indexed in a n=[2,3,4…] structure within the accuracy of the experiment. This is because wide angle peaks mostly sample the atomic scale periodicity, while the differences in the unit cells are on the much longer length scales of b={39Å, 51Å, 64Å} for the n=[2,3,4] phases respectively. As noted, the [020], [040], and [060] peaks characteristic of the interlayer spacing are conspicuously absent on the $Q_r$ axis of figure 2a. However, most of the peaks on the $Q_r$ axis are obscured, except the [20-2] at $Q_r=2Å^{-1}$. This indicates that the absence of these purely in-plane peaks is likely a systematic effect of the experiment, as will be shown subsequently. There is one region of reciprocal space that contains phase specific information about the layer width which does not lay on the $Q_r$ axis, and which has not been previously identified in the literature. It lays along $Q_z$ =2, $0<Q_r<1Å^{-1}$. This region contains the [222], [242], [262] peaks, though the [222] lays in Bragg restricted wedge on the $Q_z$ axis and is thus cut from view. A zoom in of this region is shown in figure 3. As shown in figures 3a and 3b, two peaks characteristic of the n=3 layer spacing can be observed, and distinct peaks corresponding to n=2 and n=4 are absent. However, they likely exist but are buried beneath the dominating n=3 characteristic peaks. Based on these characteristic peaks, we can definitively say that we are looking at a structure dominated by an n=3 RPP crystal. We note that the absorption length of the

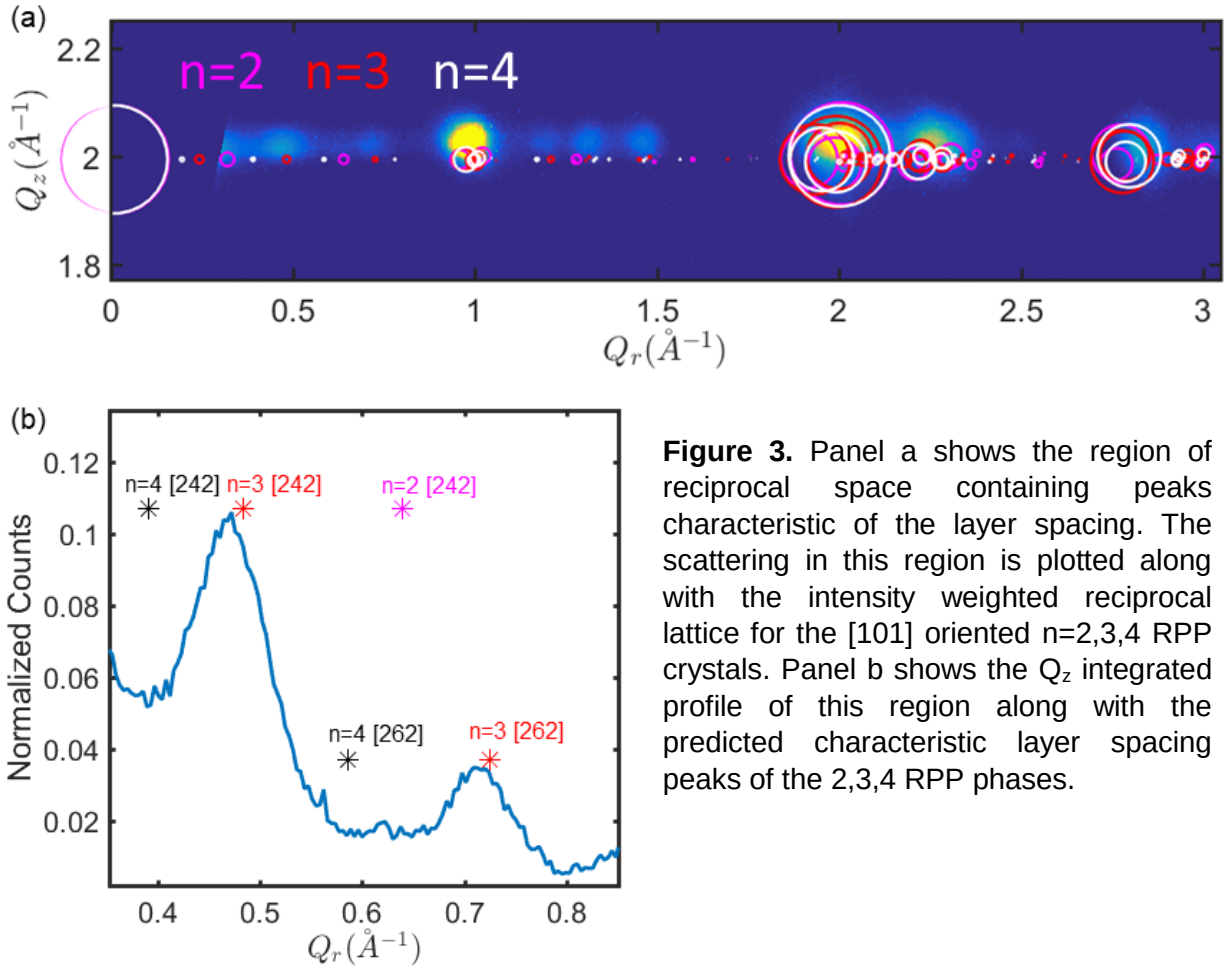


**Figure 3.** Panel a shows the region of reciprocal space containing peaks characteristic of the layer spacing. The scattering in this region is plotted along with the intensity weighted reciprocal lattice for the [101] oriented n=2,3,4 RPP crystals. Panel b shows the $Q_z$ integrated profile of this region along with the predicted characteristic layer spacing peaks of the 2,3,4 RPP phases.

13.5keV x-rays at this incident angle (0.4$^o$) is 200nm (shown in subsequent sections), so this measurement has an outsized contribution from the upper region of the film. As such, we cannot rigorously speak of the relative abundances of the various phases in the films bulk without taking this into account. However, we can say that this scattering pattern is mostly reflective of an n=3 RPP in the [101] orientation, which allows us to refine the structure based on the empirical peak positions for further analysis.

Figure 3a shows that the peaks predicted using the single crystal RPP structure lay systematically below (lower $Q_z$) the positions of the measured diffraction peaks. This implies a slight contraction of the unit cell in the a and c directions. The b dimension of the unit cell (layer stacking direction) appears in fair agreement with the single crystal prediction. Thus, we refine the single crystal structure by decreasing the unit cell by 1.4% in the a and c directions, figure 3

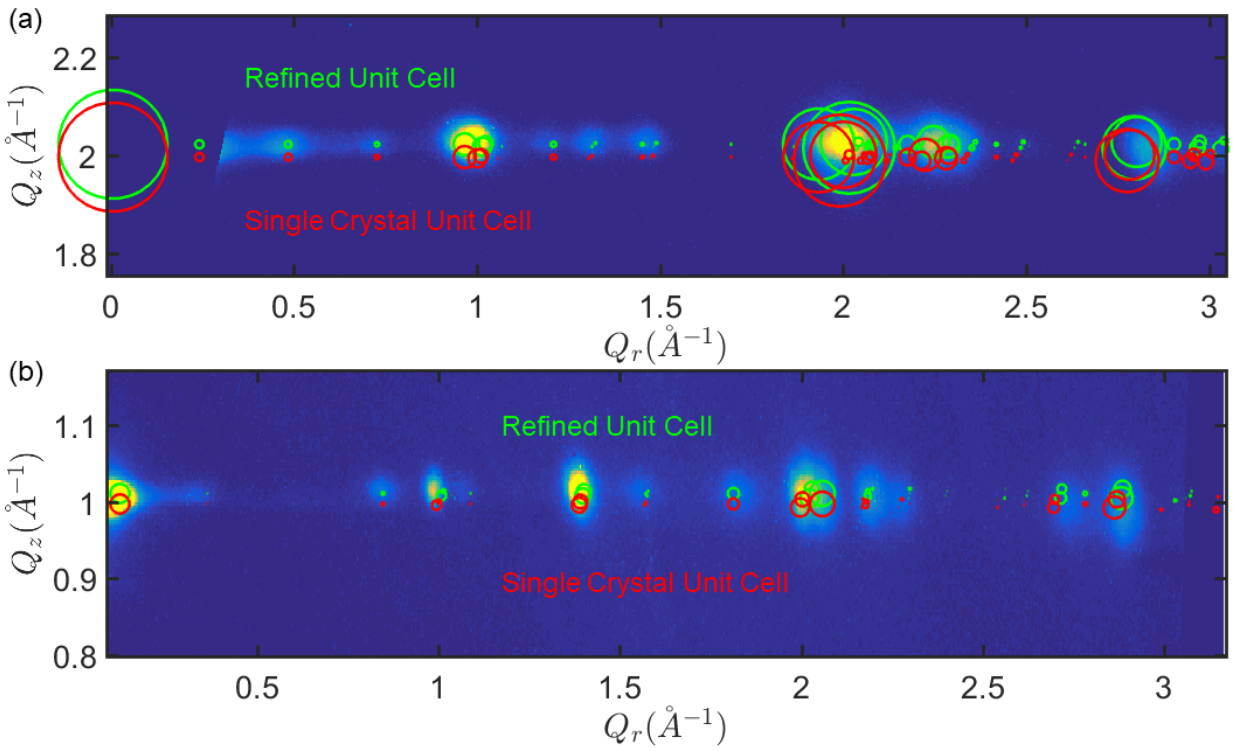


**Figure 4.** These panels compare the reciprocal lattice of the refined unit cell and the single crystal unit cell, with the measured GIWAXS scattering pattern.

shows the results of this refinement, along with the data and the predictions using the single crystal unit cell. Although the change is slight, the refinement certainly appears to agree better with the measured data.

We note that this shrinking of the in-plane unit cell is consistent with increased octahedral tilting. Figure 5a and 5b shows the octahedral tilting pattern present in single crystal n=3 RPPs. Interestingly, tilts around the [101] axis are much larger than the tilts around the [010] axis. It is reported that this results from a competition between the distortions preferred by the $MA^+$ cations in the octahedral cages and the $BA^+$ cations on the slabs surface[7]. Figure 5c geometrically illustrates concept that tilting rigid octahedra results in a compressed unit cell. If the contraction of the unit cell does in fact come from tilts of rigid octahedra around the [010] axis this would represent an important difference from the single crystal structure, with likely important electronic consequences as the in plane Pb-I-Pb bond angle has been shown to have a profound impact on

the band gap of HIOPs[8] . This issue therefor warrants further investigation, perhaps with a rigorous peak magnitude analysis.

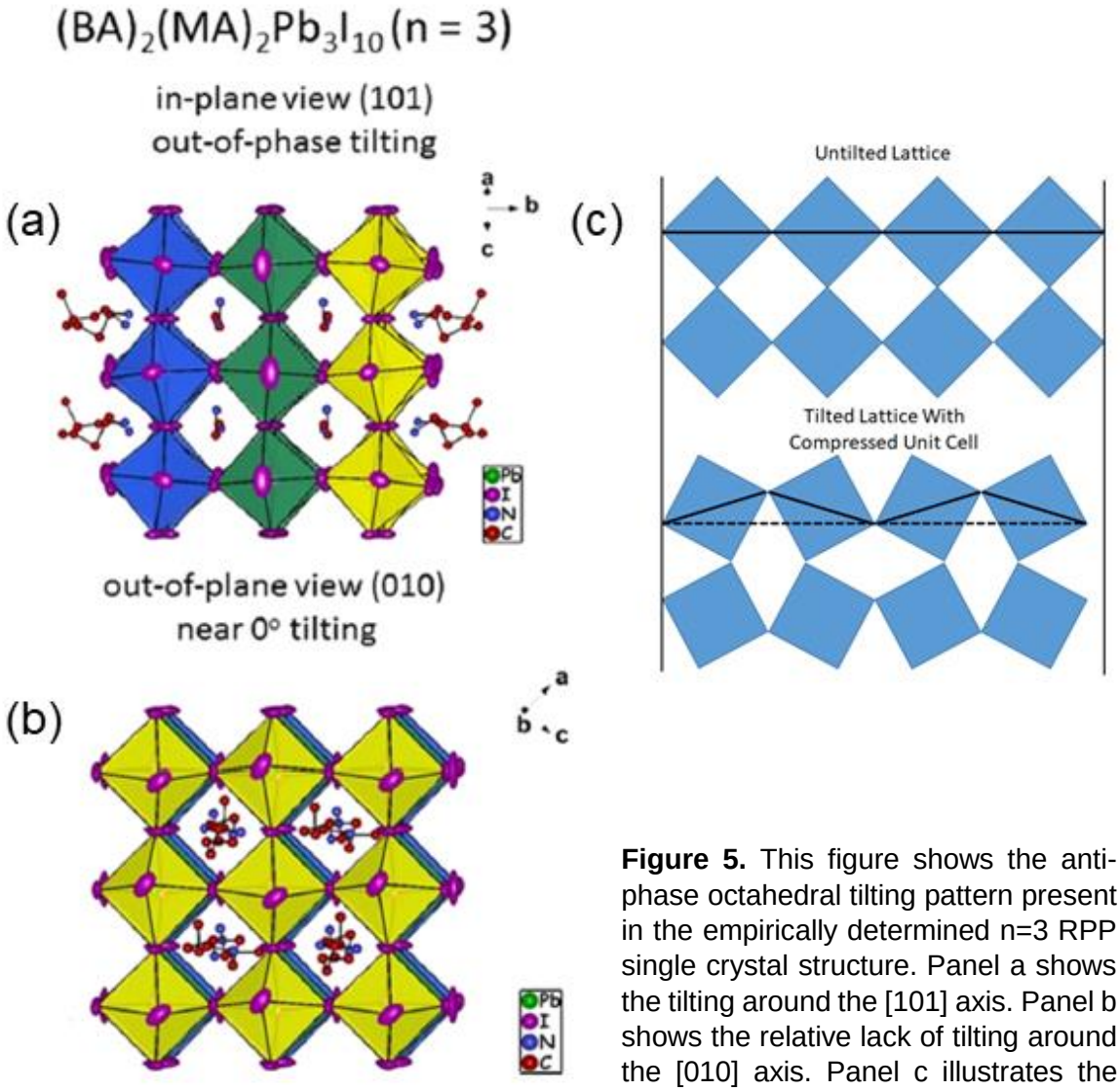


**Figure 5.** This figure shows the anti-phase octahedral tilting pattern present in the empirically determined n=3 RPP single crystal structure. Panel a shows the tilting around the [101] axis. Panel b shows the relative lack of tilting around the [010] axis. Panel c illustrates the principal that antiphase tilts of rigid octahedra compress the unit cell. **Panels a and b were taken from reference 7.**

GIWAXS as a function of Incident Angle: Investigation of surface contamination

X-rays typically have an effective refractive index less than one in solid materials as noted in chapter 2. This allows us to take advantage of the phenomenon of 'total external reflection' to

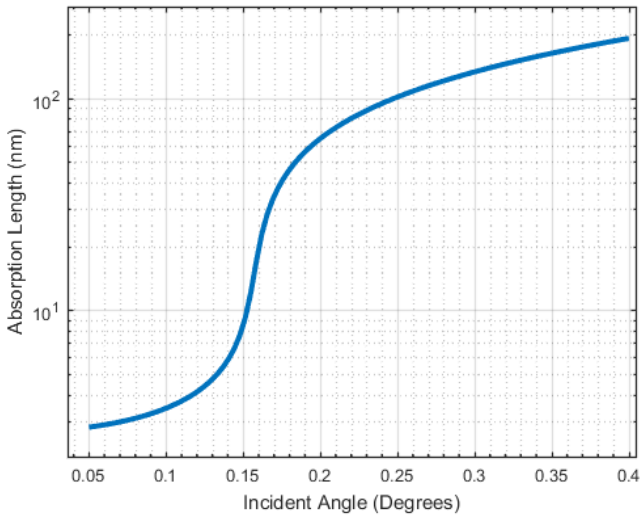


**Figure 6.** Calculated absorption length vs incident angle for n=3 RPP film.

obtain surface selective information about the crystal structure. The critical angle can be calculated based on the materials density, and empirical formula. In n=3 lead halide RPPs the critical angle is calculated to by 0.15°. Figure 6 shows the calculated absorption length versus incident angle, and a precipitous drop is observed at the critical angle, which reflects the evanescent nature of the x-ray field within the material. The absorption length represents the upper limit on the depth of the region from which scattering originates[9]. In the case of an incident angle of 0.1 degrees the main contribution to the scattering signal comes from the top ~3.5nm of the film at maximum at maximum. There for, if there are any crystalline species contaminating the surface of our samples, we should certainly be able to seem them at a low

incident angle. In particular we will be testing the hypothesis that crystalline $MaPbI_3$ exists on the films surface, in light of recent claims of its existence based on the optical properties of the films.

Figure 7 shows selections from measured GIWAXS pattern obtained at an incident angle 0.1°. We simulated the scattering of many different tetragonal $MaPbI_3$ orientations, and most produced patterns which strongly deviated from the observed GIWAXS pattern. However, for comparison we pick the two that came the closest reproducing the measured scattering results. These two orientations are the [010], and the [001]. These two orientations have special physical significance in that they contain perovskite octahedra oriented such that they could naturally corner share iodine atoms with the existing [101] oriented n=3 RPP structure existing in the films bulk. Figures 7 a and b show that the refined n=3 RPP structure comes much closer to reproducing the peak positions than bulk $MaPbI_3$ in any orientation. Note that there are certain peaks which appear to contain contributions from different phases as is evidenced by the larger

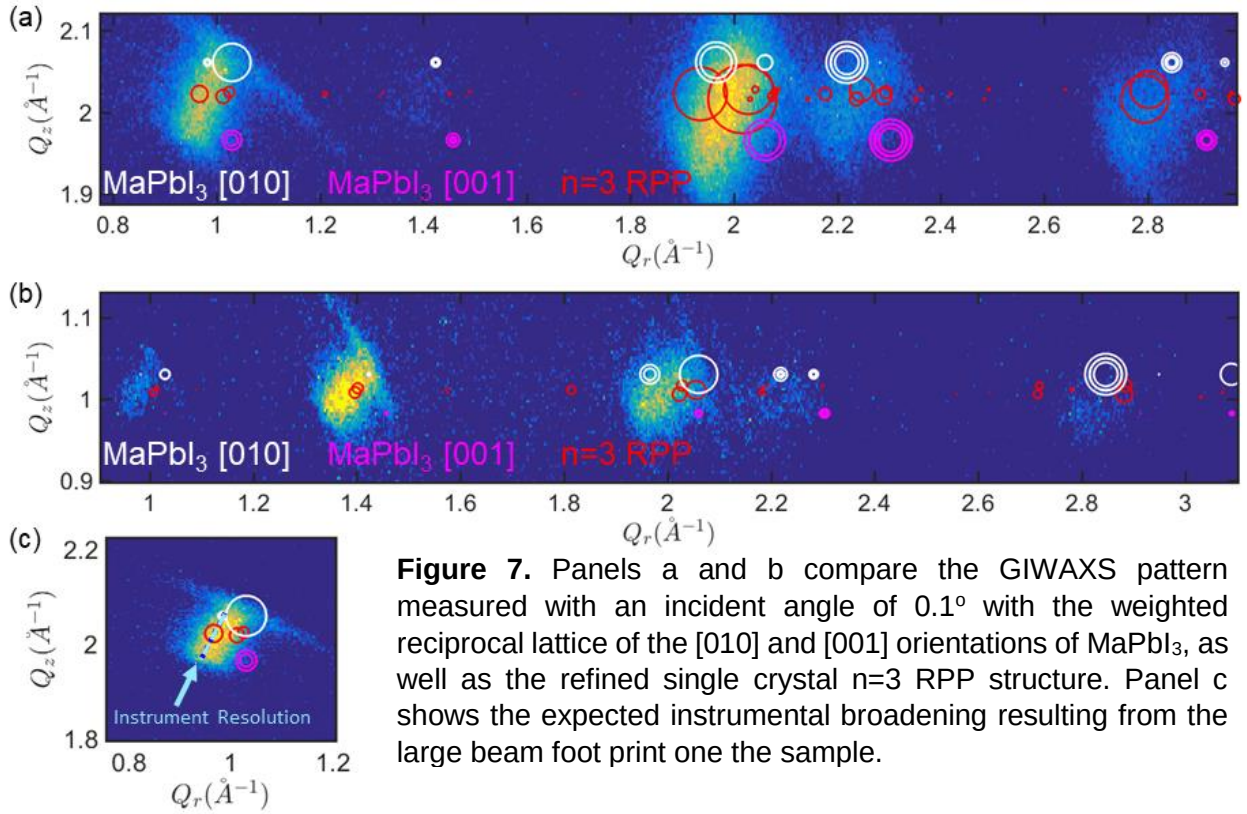


**Figure 7.** Panels a and b compare the GIWAXS pattern measured with an incident angle of 0.1° with the weighted reciprocal lattice of the [010] and [001] orientations of $MaPbI_3$, as well as the refined single crystal n=3 RPP structure. Panel c shows the expected instrumental broadening resulting from the large beam foot print one the sample.

spreading in the azimuthal direction on the high |Q| shoulder. One example of this is shown in

figure 7c. Interestingly, every peak which contains an excessively broadened high |Q| edge feature also has a [010] oriented $MaPbI_3$ peak nicely corresponding to the radial position of the broadened feature. One is tempted to conclude that these peaks represent a population of [010] oriented $MaPbI_3$ which exists preferentially on the surface of the film, and has a slightly larger distribution of lattice orientations than the bulk RPP structure. However, this interpretation is significantly less robust than it appears, although this data did confuse us for a short while. Please refer to the chapter 2 regarding the resolution limits of GIWAXS as a function of incident angle. Briefly, at low incident angle the sample is greatly overfilled by the incident x-ray beam, and has a very large foot print (I'll denote the length of the footprint W). When the beam undergoes scattering this foot print is projected on to the detector, and takes up a physical size on the detector equal to W*Tan(θ), where theta is the scattering angle defined by $\theta=2\text{Arcsin}(q_{scatt}/2k_{incident})$. This broadening in detector space results in the observed radial broadening in q space at low incident angle. The expected radial instrumental resolution expected from our 10mm sample is plotted as the blue dotted line in figure 8c. Thus it's clear that the radial breadth of the peak can be accounted for mostly by instrumental broadening. This means that any peak which is present through the whole film must be broadened by the instrumental resolution by definition. Equivalently any peak which is sharper than the instrumental resolution must come from a localized region of the film. However, there is uncertainty in what localized region of the film the peak comes from, and this translates to uncertainty in the true value of the scattering vector. Thus the radial position of any peak sharper than the instrumental resolution has no significance. The more likely explanation of this phenomena comes from inhomogeneity in the film thickness as one would expect from a spin coating procedure. In particular, at the edges of spin coated samples there often occurs a build-up of material. Pictures of the film orientations used in the experiment show that there is indeed a thick deposit of material on the upstream side of the film, shown in chapter 2. Having eliminated the uncertainty in the position, there is no longer any uncertainty in the scattering vector, which implies that this feature corresponds to the same

scattering vector as the center of the peak. With this possibility eliminated we inspect the peaks shown in figure 8a and 8b, and observe that the n=3 RPP reciprocal lattice agrees significantly better with the observed peaks than either the [010] or the [001] oriented $MaPbI_3$. We thus eliminate the possibility of *crystalline* $MaPbI_3$ contaminating the surface of our film.

Phase Purity Analysis: Observation of the [020] characteristic peak with SAXS Detector

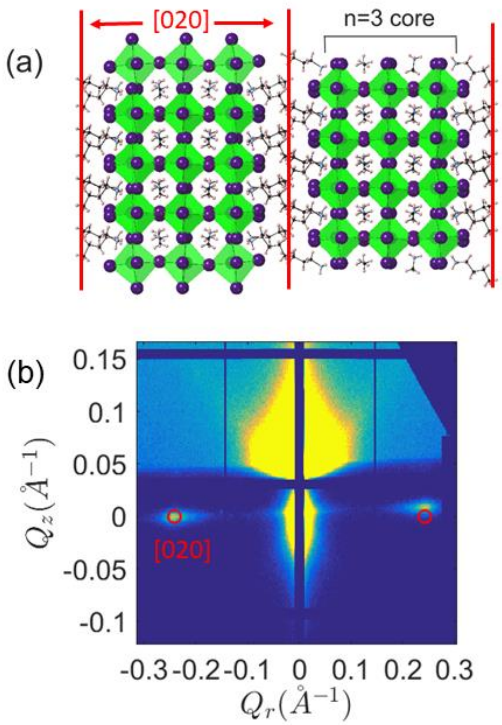


**Figure 8.** Panel a shows the RPP crystal structure with the [020] planes displayed. Panel b shows the SAXS pattern observed on a 400nm film with the predicted peak positions based on the single crystal structure.

The [242] and [262] discussed earlier in the chapter appear to sit on a relatively large background, likely due to the strength of the nearby [202] which is predicted to be the strongest peak in reciprocal space. It not clear a-priori how to remove this 'background signal', to do a quantitative analysis of the line shape to determine the relative abundances of the various phases. As noted, the other peaks which are characteristic of the layer spacing are the purely in-plane [020], [040], [060], and they have not yet been detected in hot cast films due to the [101] orientation. A clue as to why they're not observed lays in the fact that almost none of the in plane peaks are observed. This can be understood because purely in plane peaks follow the propagation of the incident beam downwards through the glass substrate, and are thus greatly attenuated. Thus, in principal they should still be detectable if one has a sufficiently sensitive detector. The small angle x-ray scattering detector at the CMS beamline at NSLS-II turned out to be exactly what was needed, as the background counts are essentially zero for large integration times up to 300s.

Figure 8 shows the [020] peaks are readily observable, and confirm our assessment that the RPP slabs stand perpendicular to the substrate. The layer spacing appears to be in good agreement with that predicted for the n=3 single crystal RPP structure of ~25.5Å, corresponding to a peak at $Q_r$=0.248Å$^{-1}$. Note that the peaks appear in the sub-horizon on the SAXS detector implying they propagate through the glass substrate. The surface scattering of the direct beam is shown in the region $Q_z$ > 0.05 Å$^{-1}$. Due to the in plane nature of the [020] Bragg peaks, they're behavior as a function of incident angle mirrors that of the transmitted beam, disappearing below the critical angle. Therefor we do not have robust SAXS data sets as a function of incident angle.

Figure 9 shows that the films all exhibit the [020] peak characteristic of the n=3 layer spacing. Interestingly, figure 9a shows that the 20nm film alone exhibits a [020] peak on the $Q_z$ axis and the $Q_r$ axis. This represents a bimodal distribution of crystal orientations with one population in the conventional [101] orientation with slabs perpendicular to the substrate, the other in the [010] orientation representing slabs parallel to the substrate. At the end of this chapter I will

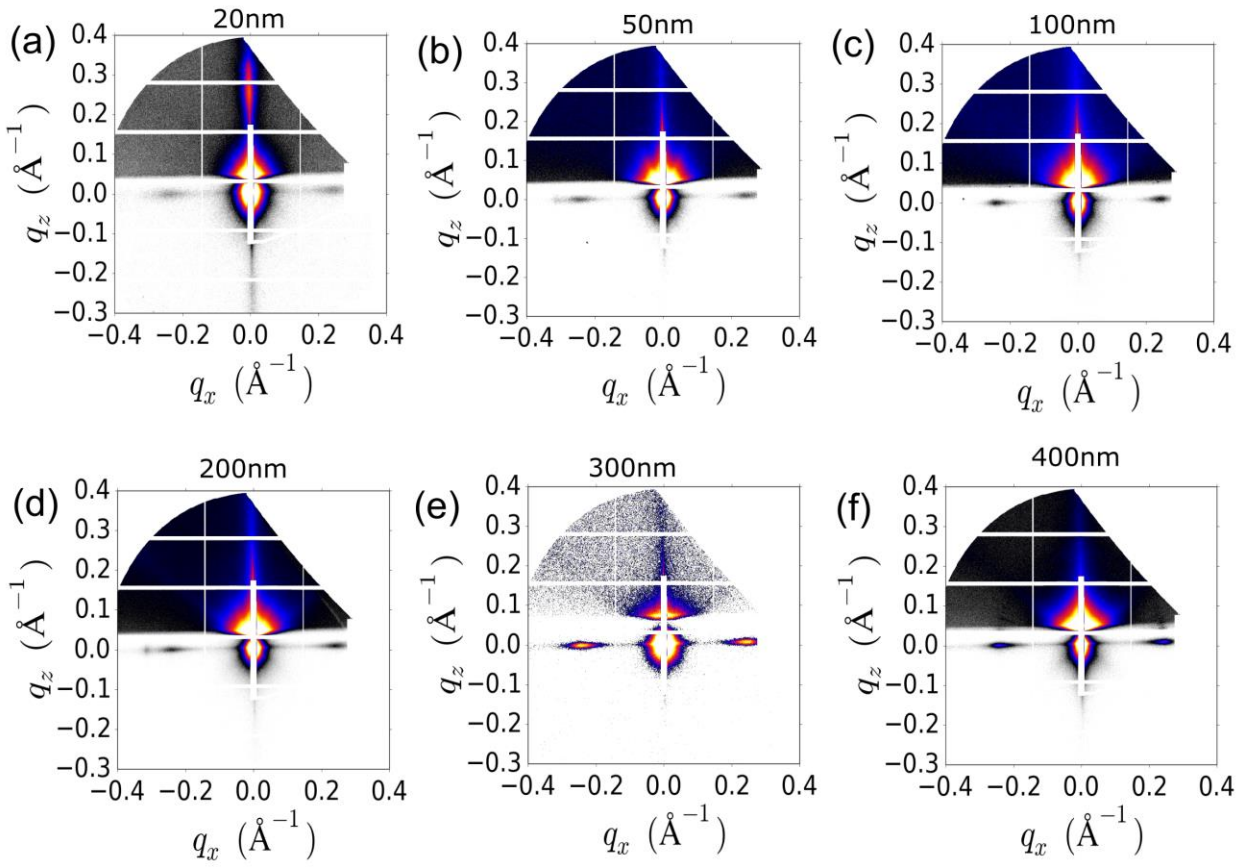


**Figure 9.** Panels a-f show the GISAXS pattern obtained on hot cast n=3 RPP thin films of various thicknesses.

speculated about the significance of this fact, and what it might imply about nucleation mechanism producing the vertical slab orientation obtained via the hot casting procedure.

The region above $Q_z$=0.05Å$^{-1}$ reflects the surface scattering of the direct beam. Figure 10 shows the normalized $Q_r$ slices of the surface scattering at various $Q_z$. This data exhibits two important distinct decay regimes as a function of $Q_r$. The low $Q_r$ regime decays as a power law with an exponent of 0.5. At a certain $Q_r$, a crossover to a much faster decay is observed. The $Q_r$ at which this crossover occurs increases with increases $Q_z$. Another regime appears at still greater $Q_r$ which is characterized by a much slower decay. These profiles qualitatively agree with previous measurements of roughness on a self-affine surface[10–12]. Although we note that the characteristic of self-affine surfaces: $\lim_{Q_r \to \infty} I(Q_r) \sim Q_r^{-\nu}$ [10,12] does not appear to obtain in our films. Rather it is the

low $Q_r$ behavior that appears like a power law with a power of 1/2. Further analysis of the surface scattering may yield an understanding of the crystal growth mechanisms, as it has in the case of kinetic roughening[10,11]. Further understanding of this phenomenon may be obtained by acquiring data with a higher Q resolution, to confirm if this power law behavior hold at even larger length scales.

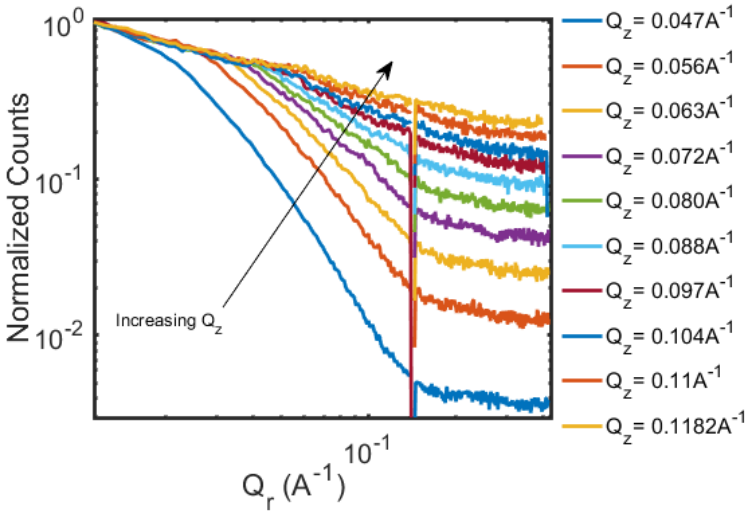


**Figure 10.** This figure shows normalized slices of the SAXS surface scattering as a function of $Q_r$ for various $Q_z$. This data was obtained on a 300nm film at an incident angle of 0.3°.

Figure 11 shows the $Q_z$-integrated profiles of the Bragg scattering in the region around $Q_z$=0. Most of the observed [020] peaks reflect a n=3 layer spacing, but there is some residual scattering from other phases in the form of distinct satellite peaks. Thus we conclude that our films contain a mixture of phases, but are dominated by n=3.

Figure 12 shows these same profiles on a linear scale (note the sign inversion of the $Q_r$ axis). Here we have chosen the measurements exhibiting the largest amplitude of the satellite peaks. We note that 20nm film contained no discernable satellite peaks, although the peak width is relatively broad. The observed Bragg peaks are well localized and centered around the n=3 value. These profiles were fit by constraining the centers of the Gaussians to lay at the theoretical positions of the [020] of the n=2,3,4 RPP phases respectively, and the results look quite good in most cases. The figures d and e show relatively poor fits in the region $|Q|>0.28Å^{-1}$ which likely over-estimates the contribution of the n=2 phase. From these fits, the relative peak magnitudes have been extracted. The absolute scattering intensity of these crystals were calculated using the single crystal

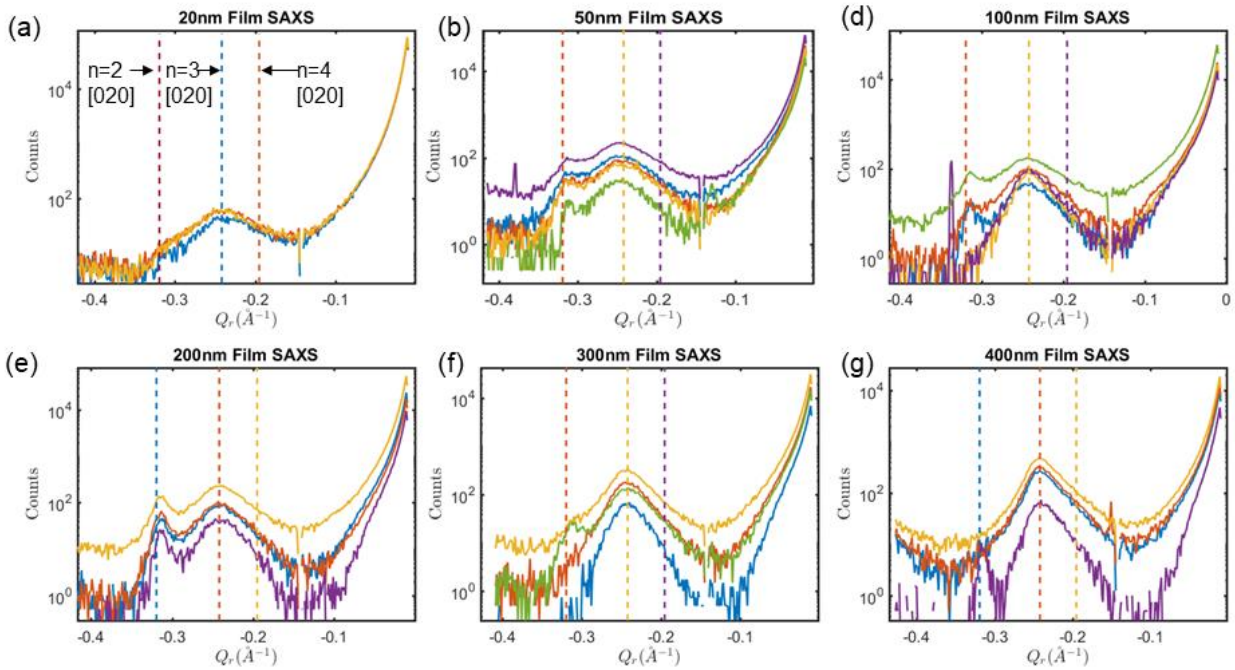


**Figure 11.** Panels a-g show the observed $Q_z$ integrated profiles, some displaying satellite peaks, other without them.

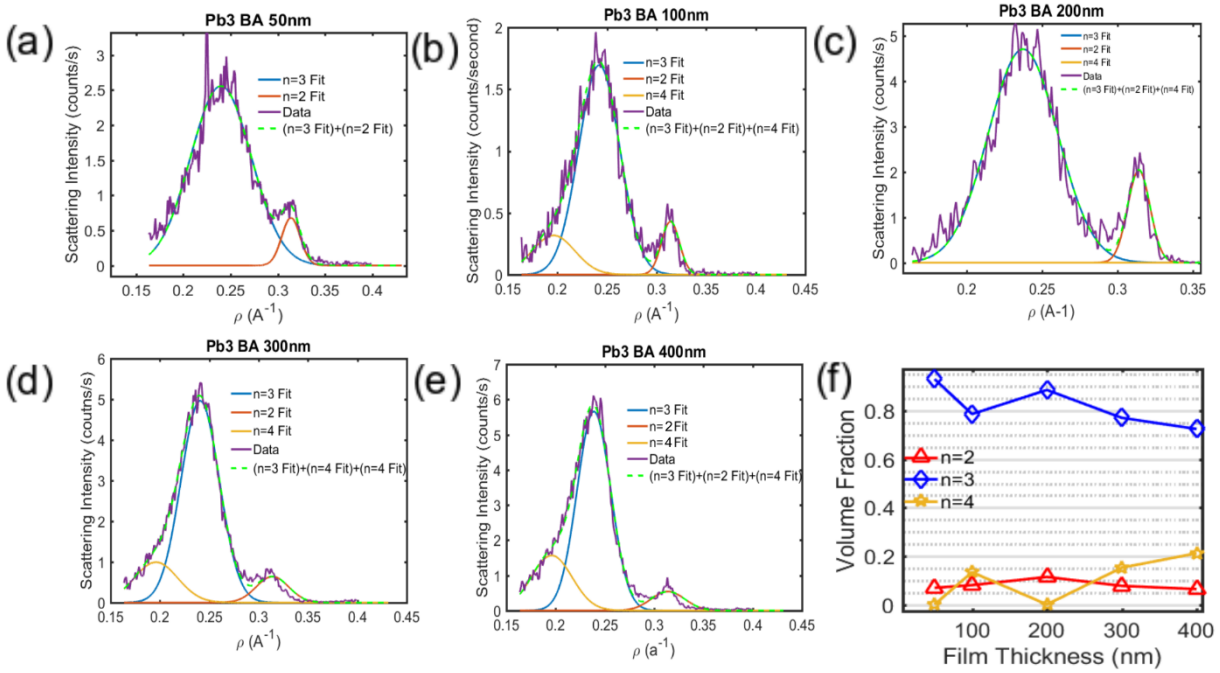


**Figure 12.** Panels a-e show the $Q_z$ integrated SAXS profiles, which are fit with gaussians at the theoretical peak positions. Panel f shows the calculated relative volumetric abundances of each phase.

structure. Combing the simulations with the peak magnitudes, allows us to calculate the relative

volumetric abundances of the various phases, which is shown in figure 12f. This shows that our films are all at least 70% n=3 RPP films.

This value roughly agrees with the relative sizes of the observed optical features in the linear absorption spectrum. We note that the beam foot print on our samples was large ~10mm long compared to the size of our samples. We typically observe an increase in film thickness moving outward from the films center, as can be observed as a gradient in the darkness of the film. This results from edge effects of the spin coating process. When performing grazing incidence diffraction the whole illuminated contributes to the scattering. Thus we cannot tell from this data if the other phases exist preferentially towards the edges or are equally mixed through the film. Importantly the center of the film is where we conducted all of the optics experiments.

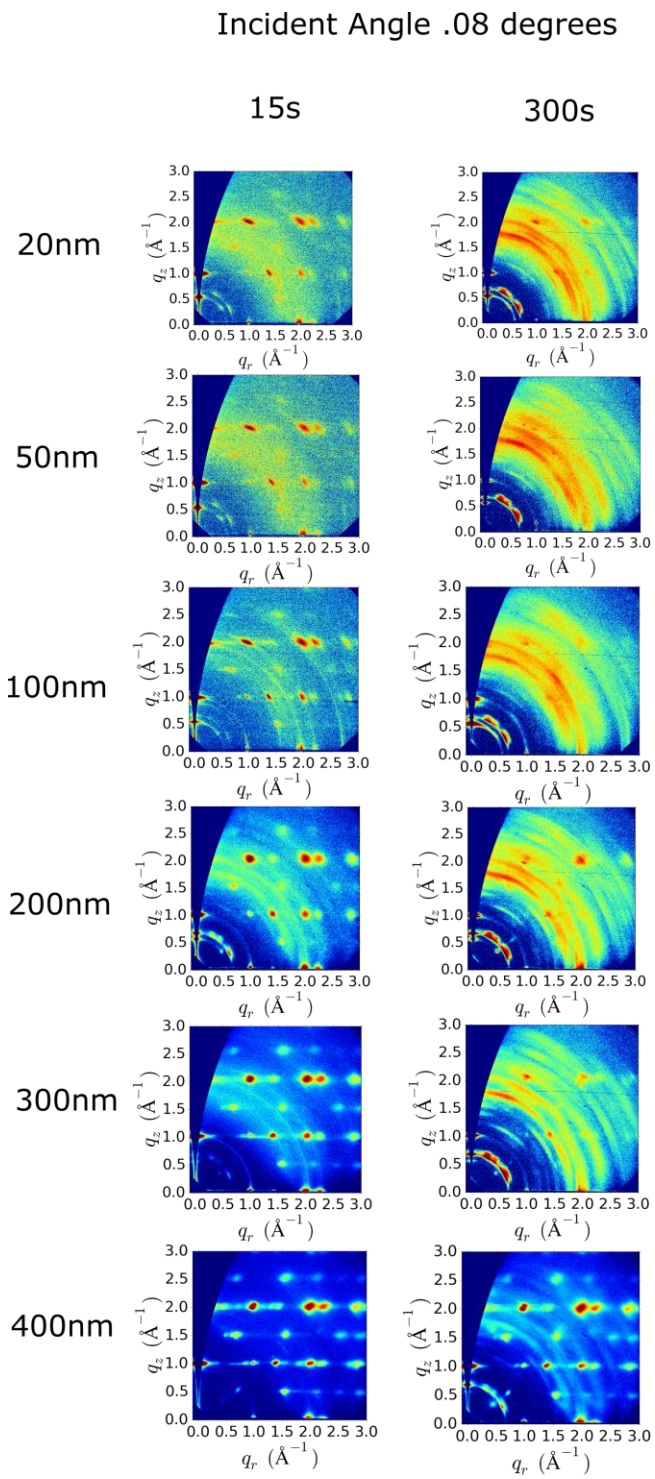


**Figure 13.** This figure shows the measured GIWAXS patterns obtained at 15s integration time vs 300s integration time for all film thicknesses.

Sample Degradation Analysis

Our samples exhibited a pronounced degradation effect which is apparent in the long integration time data shown in figure 13. The peaks are systematically blurred out in the azimuthal direction, eventually leading nearly isotropic scattering at large |Q|. Therefor all of our analysis is based on the 15 second integration time data, for which we observe no irreversible changes in the scattering pattern. The X-ray dose used to acquire out data was $7.4 \times 10^{15}$photons/mm$^2$ with a photon energy of 13.5keV.

GIWAXS as a Function of Incident Angle: 200nm Film

Figure 14 shows the calculated beam footprint versus incident angle. Our samples were 10mm long which means that the data obtained at low incident angle ($\alpha_{incident} < 0.3^0$) over fills the sample. This effect implies that below 0.3 degrees we should see a steady decrease in the scattering intensity of all peaks. However, the scattering cross section increases at low angle which tends to increase the scattering intensity of all peaks. Together,

these effects produce peak magnitudes that vary in a less intuitive way than we would like, however the peak ratios still contain physically meaningful information.

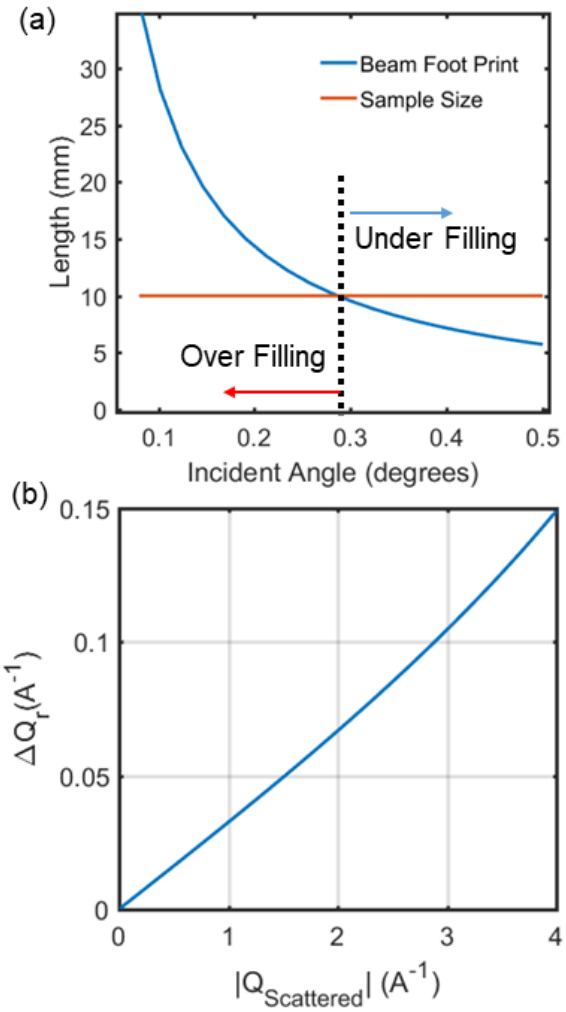


**Figure 14.** Panel a shows the calculated beam foot print and panel b shows the expected radial broadening.

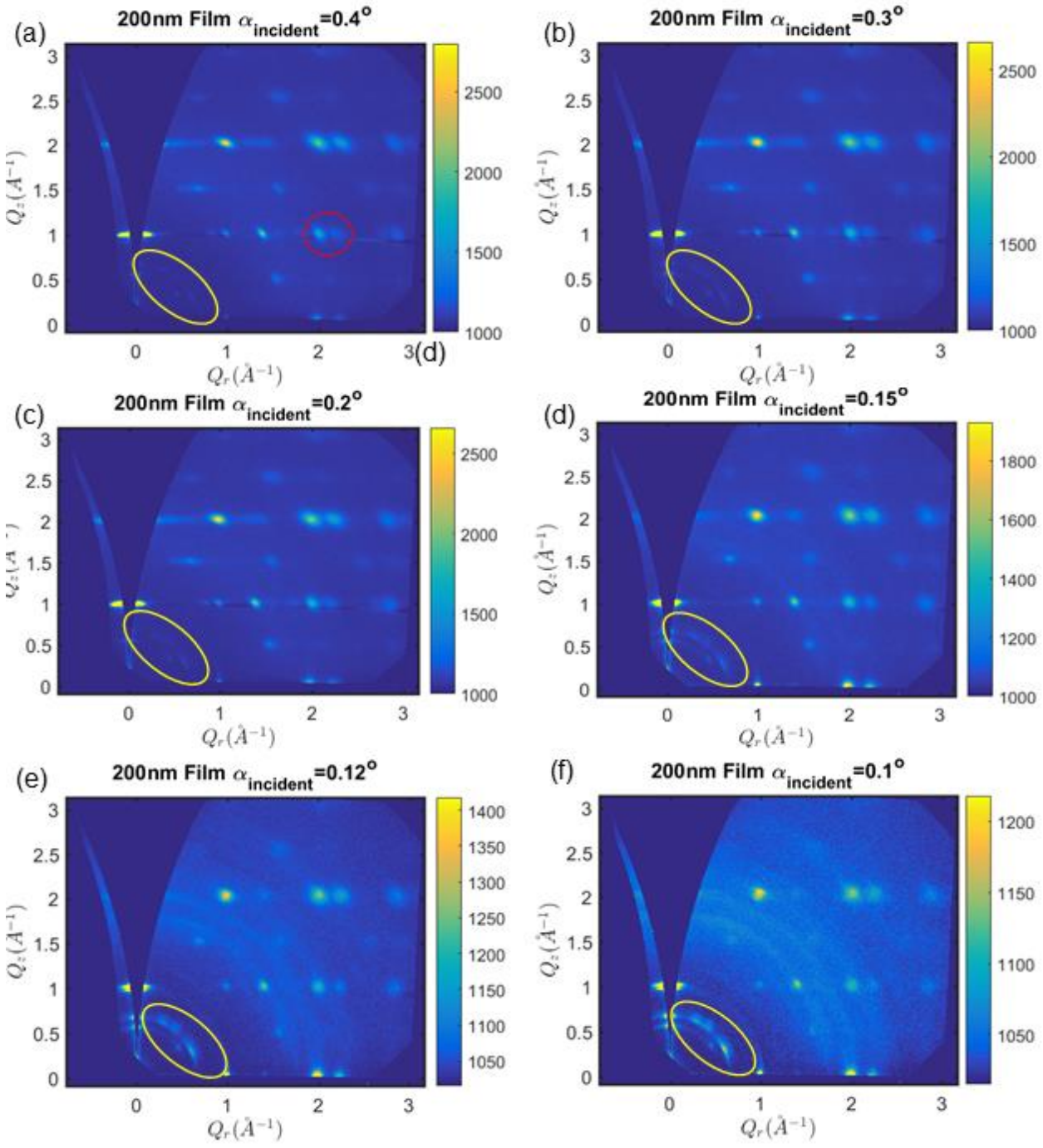


**Figure 15.** These panels show the measured GIWAXS pattern of a 200nm film as a function of incident angle.

Figure 15 shows the GIWAXS patterns obtained on a 200nm film as a function of incident angle. These patterns were all taken on the same spot on the film, and chronologically were taken from lowest angle to highest angle, which implies that the low angle data corresponds the lowest total dose of radiation given to the spot. As shown in figure 6, at 0.4 degrees incident angle the

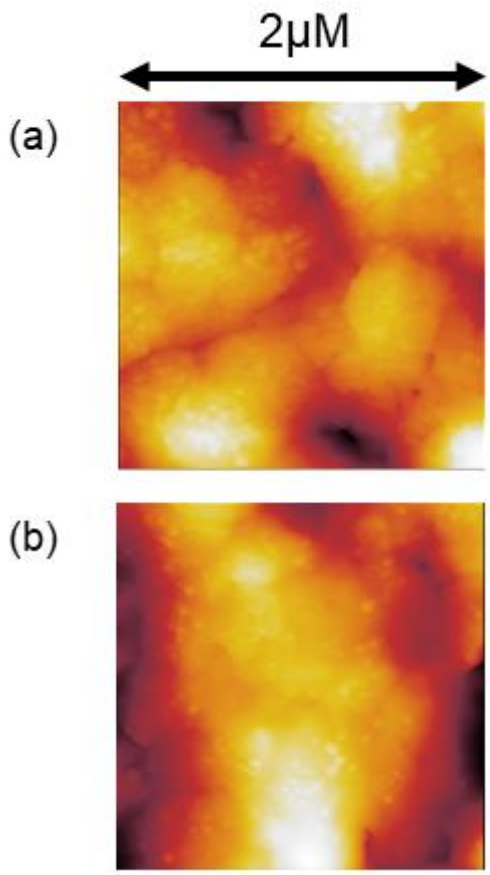


**Figure 16.** These panels show AFM images of the surface of an n=3 RPP film. The color range is 50nm, while the whole box is (2μ)x(2μ).

absorption length is 200nm which corresponds to the full thickness of this film. At while at 0.1 degrees the scattering originates from a region within 3.5nm from the surface. As expected, the peak magnitudes decrease at lower angle due to the greatly decreased transmission coefficient at angles less than the critical angle. As a result of this our signal to noise decreases such that some of the fainter peaks present at $0.4^0$ incident angle can no longer be distinguished from the background. However, there is a set of peaks at $|Q|\sim0.67Å^{-1}$ whose relative prominence increases with respect to the others as the incident angle is decreased. These peaks are circled in yellow in figure 15.

At low angle we also observe an increase in magnitude of a set of diffuse rings at $|Q|>1.5\ Å^{-1}$. The azimutha width of these peaks indicates they do not arise from the highly oriented structure which gives rise to the Bragg peaks. However, |Q| of these rings seem correlated to the peaks of the RPP structure. We therefor conclude that these diffuse rings at high angle represent a strongly disordered nano-crystalline population existing on the films surface. Features looking like nanocrystals can be observed in AFM images of the films surface in figure 16a and 16b. We don't suspect the nanocrystals are responsible for creation of the anomalous mid gap sates, because the latter also occur in exfoliated flakes of single crystal n=3 RPP as well, and AFM images haven't detected them there.

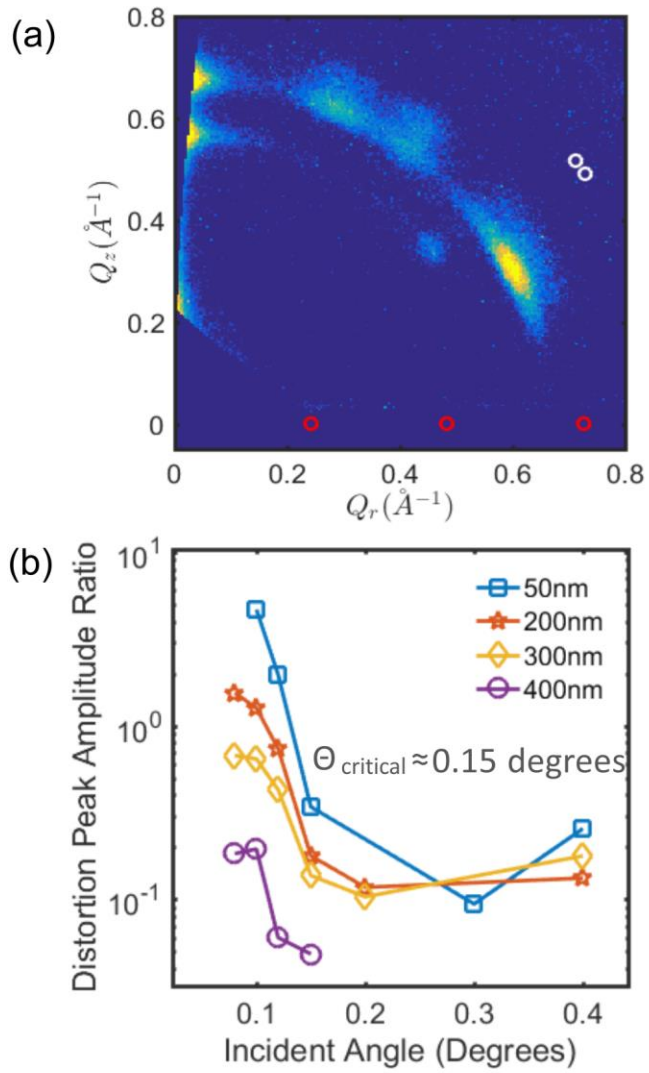


**Figure 17.** Panel a shows a zoom in of the peaks at 0.67Å$^{-1}$ extracted from figure 15f. Panel b shows the relative peak magnitude as a function of incident angle.

Figure 17a shows a zoom-in of the peaks at 0.67Å$^{-1}$. The red circles represent the expected scattering peaks of the n=3 RPP, while the white circles are the expected peak position of $MaPbI_3$ in the [010] and [001] orientations. However, none of these peaks coincide with the positions of the observed peaks. It can be shown that there is no orientation of $MaPbI_3$ or the n=3 RPP which can explain these peaks. Their position indicates they correspond to a periodicity of ~93Å. Which is almost twice the size of the n=3 RPP unit cell (~102Å). The orientation of the peaks indicates that they represent a periodicity which is well defined with respect to the RPP lattice. We therefor infer that they represent a distortion of the n=3 RPP unit cell, however it is unclear exactly what type of distortion they correspond to. We'll hereafter refer to them as 'distortion peaks'.

Figure 17b plots the ratio of the magnitude of the distortion peak to that of the Bragg peak circled in red in figure 15a (which corresponds to the RPP [311]). This peak was chosen for normalization of the distortion feature, as it has the same azimuthal coordinate. However this choice is arbitrary and figure 15 a-f show that the same conclusion would be drawn using any

prominent peak in the scattering pattern. The distortion features exhibit a large increase in relative magnitude below the critical angle, which shows that these features are surface localized. We expect that these peaks represent distortions which come about due to surface strain. Distortions of the RPP crystal structure are expected to have a huge impact on the films electronic structure[12]. The observation of a surface localized distortion is interesting because as will be shown in chapter 6, our films contain a mid-gap state localized on the film's surface. Due to concomitant appearance of mid gap states and distortions on the films surface, as well as the a-priori connection between electronic structure and crystal structure, we infer that these surface distortions are the physical cause of the mid gap surface state. This is one of the main results of this thesis. However, this is clearly not proof of a causal connection between them.

GIWAXS as a Function of Film Thickness: 0.4 Degrees Incident Angle

Trends in the behavior of the Bragg peaks as a function of angle and film thickness can be quantified by fitting the GIWAXS scattering peaks with a function of the form:

$$F(\rho,\theta)=A+ B*\exp(-2[( (\theta- \theta_0)/2\sigma_\theta)^2+ ( (\rho- \rho_0)/2\sigma_\rho)^2)])$$

Such that $Q_z= \rho Sin(\theta)$ and $Q_r= \rho Cos(\theta)$. From these fits $\sigma_\theta$, $\sigma_\rho$ and the peak amplitude can be extracted as a function of film thickness. Note that these extracted fit values were used in making figure 17b. Figure 18a shows the indexing scheme used to identify features referred to subsequently. Figures 2,3, and 4 show that the most prominent features contain contributions from multiple planes. However, I have here used the convention to index the peaks according to the plane contributing the maximum theoretical intensity to the feature. This indexing scheme appears different than previous attempts[1,2,4], however this is simply a result of the stated convention.

Figure 18b shows the scaling of the peak magnitudes against the square of the film thickness, illustrating the quadratic scaling of the peak magnitudes between 50nm and 200nm. This factor of four increase in the film thickness results in roughly a factor of 16 increase in the

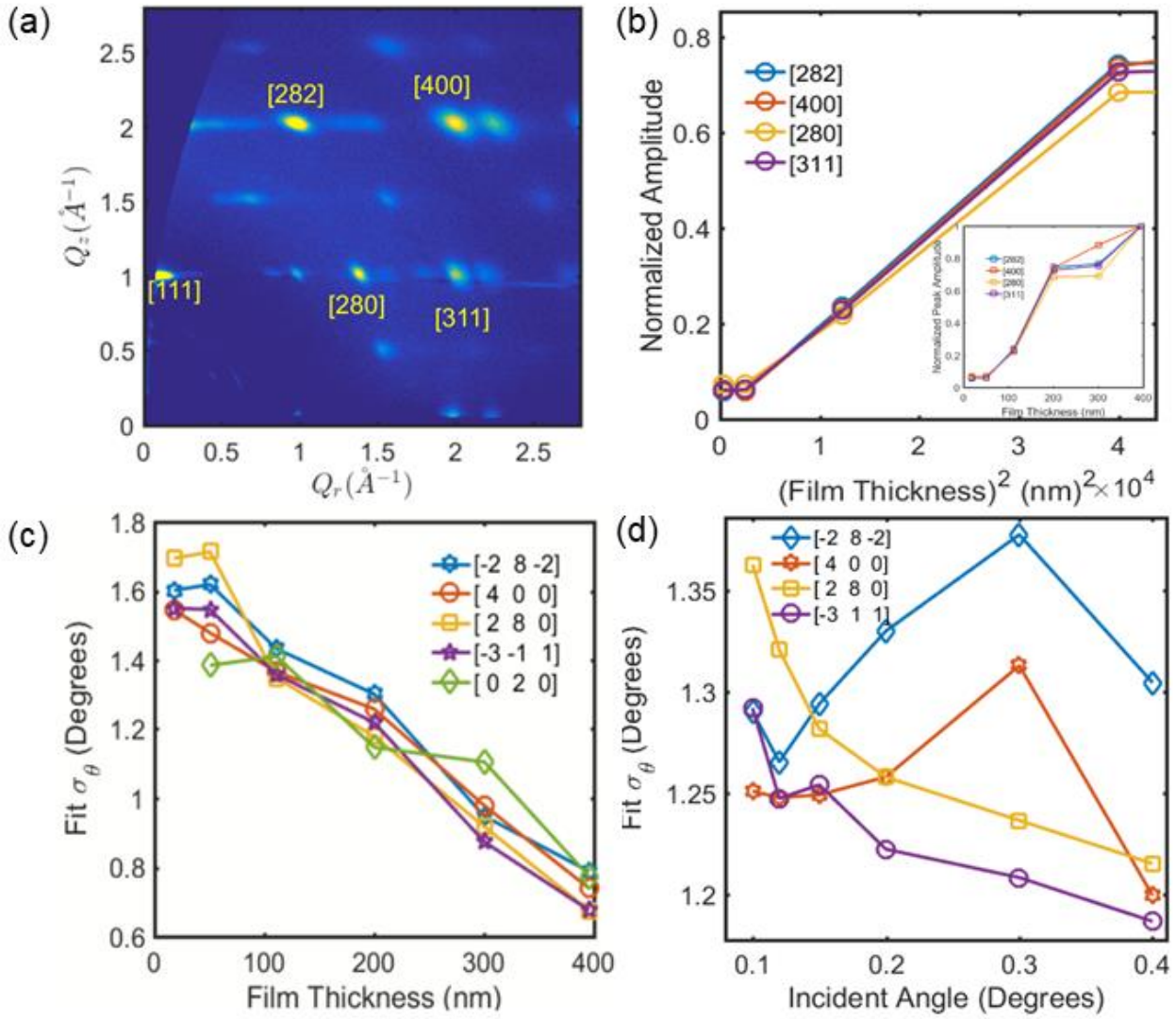


**Figure 18.** These panels show the behavior of the observed GIWAXS patterns as a function of film thickness. Panel a shows the indexing of the various features. Panel b and b inset show the scaling of the peak magnitudes with film thickness. Panel c shows the fit azimuthal width as a function of film thickness. Panel d shows the variation of the peaks width with incident angle.

peak magnitude as expected. The inset on figure 18b shows the scaling against the film thickness for all of the films. Films thicker than 200nm show peak magnitudes which increase relatively

slowly compared to the quadratic scaling seen for thinner films. However, this does not reflect anything physically important about the structure of the films. Rather, the absorption length of the radiation at 0.4 degrees incident angle is 200nm as is shown in figure 6. Therefor the decrease in the slope for films greater than 200nm in 19b is reflecting the absorption of X-rays in the film. The region of quadratic scaling of peak magnitudes indicates that the full thickness of the crystal is scattering coherently, which strongly indicates single crystal behavior through the films depth. We note that the 20nm film does not fit this trend, and the peak magnitudes level off below 50nm, however this is not entirely unexpected, as the SAXS data of the 20nm film shows a bimodal distribution of peak intensities, and thus a-priori has a different statistical distribution of lattice orientations than the rest of the film.

Figure 18c shows the extracted azimuthal peak width, $\sigma_\theta$ for the various peaks as a function of film thickness. The relative consistency of $\sigma_\theta$ for all peaks in all films indicates that this angular spreading should be interpreted as resulting from the distribution of grain lattice orientations, rather than some other type of disorder. The data indicates this distribution of lattice orientations is gaussian with a width on the order of $1^o$. A monotonic decrease in the angular spreading is observed with increasing film thickness indicating a progression towards better gain alignment with increasing film thickness. This reasonably small but consistent trend is likely directly reflective of the crystal growth or nucleation mechanism, and any candidate model of this mechanism should provide a way to understand this data. In contrast the radial peak width shows no monotonic trend in film thickness, likely because it is dominated by instrumental resolution.

Finally, figure 18d shows how the azimuthal peak width varies as a function of incident angle. The variation is with angle is less than 10% with no clear trend. Thus this data shows that the ordering of the lattice is roughly independent of the depth of the film which is probed, which is also consistent with single crystal behavior in the out of plane direction.

<u>Speculation Regarding the Nucleation Process Which Gives Rise to Vertical Slab Orientation.</u>

As noted the SAXS data taken on the 20nm film indicates a bimodal distribution of layer orientations (figure 9a). Clearly the nucleation process in this 20nm film is strongly influenced by the proximity to the substrate. This implies that the natural growth motif of the crystal nucleated on the substrate leads to slab stacking parallel to the substrate. We thus reason that the nucleation process which seeds the vertical slab orientation likely occurs at the air-solvent interface, in agreement with a recent publication which showed that vertically oriented RPP slabs can nucleate at the air-solvent interface[2].

This concept sheds light on how the hot casting procedure works. I suggest that hot casting causes strongly oriented films by inhibiting nucleation at the substrate, and thereby promoting the contributions which nucleate at the air-film interface, which is inherently oriented. Nucleation at the substrate is inhibited because it's elevated temperature increases the solubility of the ions in the solution in its immediate vicinity. However, at the air-solvent interface, solvent is rapidly evaporating, cooling the liquid and increasing the concentration of ions. Thus hot casting allows nucleation at the top interface by inhibiting nucleation at on the substrate. And nucleation at the top interface is vertically oriented[2].


1. Tsai, H. *et al.* High-efficiency two-dimensional Ruddlesden–Popper perovskite solar cells. *Nature* **536,** 312–316 (2016).
2. Chen, A. Z. *et al.* Origin of vertical orientation in two-dimensional metal halide perovskites and its effect on photovoltaic performance. *Nat. Commun.* **9,** (2018).
3. Cao, D. H., Stoumpos, C. C., Farha, O. K., Hupp, J. T. & Kanatzidis, M. G. 2D Homologous Perovskites as Light-Absorbing Materials for Solar Cell Applications. *J. Am. Chem. Soc.* **137,** 7843–7850 (2015).

4. Blancon, J.-C. *et al.* Extremely efficient internal exciton dissociation through edge states in layered 2D perovskites. *Science* **355,** 1288–1292 (2017).
5. Yuan, M. *et al.* Perovskite energy funnels for efficient light-emitting diodes. *Nat. Nanotechnol.* **11,** 872–877 (2016).
6. Liu, J., Leng, J., Wu, K., Zhang, J. & Jin, S. Observation of Internal Photoinduced Electron and Hole Separation in Hybrid Two-Dimentional Perovskite Films. *J. Am. Chem. Soc.* **139,** 1432–1435 (2017).
7. Stoumpos, C. C. *et al.* Ruddlesden–Popper Hybrid Lead Iodide Perovskite 2D Homologous Semiconductors. *Chem. Mater.* **28,** 2852–2867 (2016).
8. Pedesseau, L. *et al.* Advances and Promises of Layered Halide Hybrid Perovskite Semiconductors. *ACS Nano* **10,** 9776–9786 (2016).
9. Dosch, H. *Critical Phenomena At Surfaces and Interfaces*. (Springer Tracts in Modern Physics, 1992).
10. Salditt, T., Metzger, T. H., Brandt, C., Klemradt, U. & Peisl, J. Determination of the static scaling exponent of self-affine interfaces by nonspecular x-ray scattering. *Phys. Rev. B* **51,** 5617–5627 (1995).
11. *X-ray scattering*. (Nova Science Publishers, 2012).
12. Sinha, S. K., Sirota, E. B., Garoff, S. & Stanley, H. B. X-ray and neutron scattering from rough surfaces. *Phys. Rev. B* **38,** 2297–2311 (1988).

# Chapter 6:

## Transient Absorption Analysis

## Transient Absorption Spectroscopy Studies Of $BA_2MA_2Pb_3I_{10}$

Although RPP thin films exhibit a crystalline structure which strongly resembles that of single crystal samples, notable differences in their optical properties have been observed[1–4]. Photoluminescence studies show the films contain a sub gap defect state whose emission dominates that of the film. A number of photophysical questions about the electronic structure of these films and how they operate in devices remain. In particular: How can a strongly excitonic material produce an efficient solar cell in a planar geometry? What's the relationship between the emissive mid gap states and excitons, and how do they interact during device operation? How does the well-established [101] structural orientation observed in hot cast films impact on photo-excited carrier dynamics? Is the electronic structure constant through the film? To answer these questions, we performed femtosecond and nanosecond transient absorption spectroscopy on a set of hot cast $BA_2MA_2Pb_3I_{10}$ films with varying thickness (20nm-400nm), and compared the results to those obtained on a post annealed film.

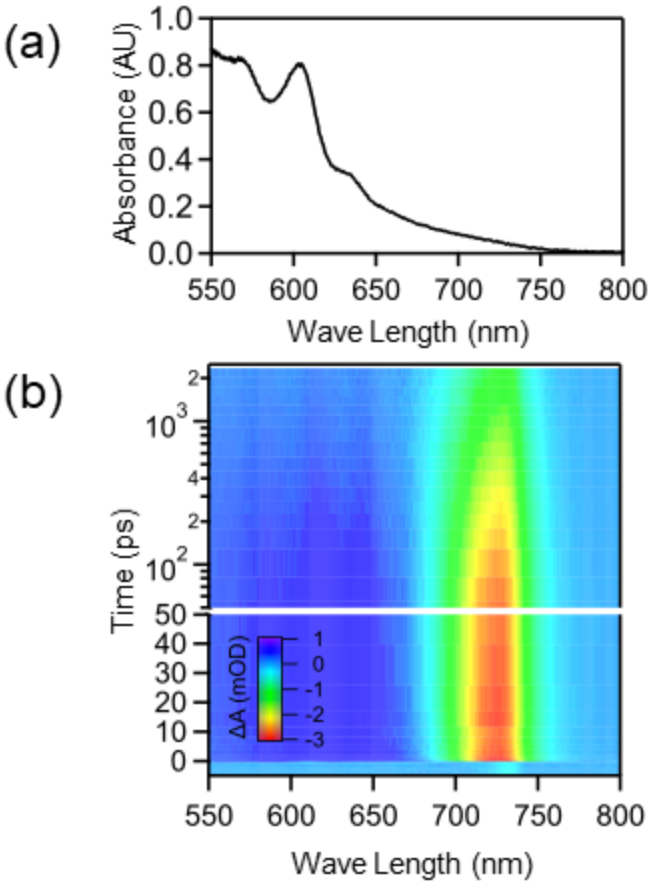


**Figure 1.** Panel a shows the measured linear absorption of an n=3 hot cast RPP film 200nm thick. Panel b shows that measured transient absorption spectrum of the same film excited at 730nm with an absorbed fluence of $1x10^{13}cm^{-2}$.

Figure 1a shows the absorbance spectrum measured using a fourier transform interferometer. This curve was calculated by measuring both the transmission and reflection, and calculating $-\log(T/(1-R))$. It can be shown that using empirically determined T and R implies this function well approximates $4\pi[Imag(n)]L/\lambda$. In the former equation n is the complex refractive index L is the film thickness and λ is the wavelength. This spectrum exhibits 3 the sharp excitonic features. The largest feature at 605nm coincides with the ground state exciton in single crystal n=3 RPP[3–6]. Around the central feature at 605nm are two satellite peaks at 572nm and 635nm. It has been noted that the positions of these smaller peaks correspond to the ground state exciton transitions in single crystal n=2 and n=4 RPPs, and have thus been attributed to contaminating n=2 and n=4 phases respectively[4,7–11]. Phase purity analysis based on grazing incidence small angle scattering measurements (in chapter 5) indicate that our films contain up to 30% percent (by volume) contamination with other RPP phases. Thus, following the literature we assign the small features at 572nm and 635nm in figure 1a as the ground state excitons of the contaminating n=2 and n=4 phases respectively.

Figure 1b shows the TA spectrum observed exciting the thin film at 710nm. A broad bleaching features centered at 730nm rises quasi-instantaneously (instrument limited) after

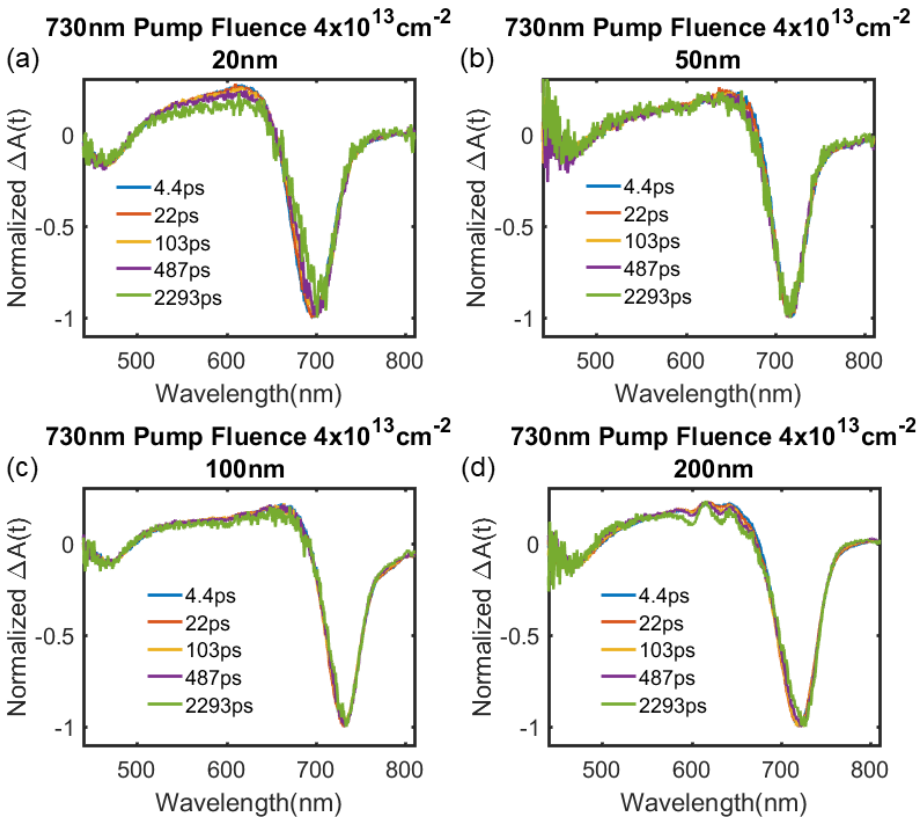


**Figure 2.** These panels show the normalized differential absorption spectrum observed in RPP thin films under NIR excitation for various film thicknesses. Panel a, 20nm. Panel b, 50nm. Panel c 100nm. Panel d 200nm.

excitation. This feature represents a population of photo-excited carriers occupying the states involved in the transition at 730nm. The feature at 730nm does not coincide with the ground state RPP exciton of the n=1,2,3,4, or 5 phases. The appearance of an optically active state in the band gap of RPP single crystals is expected in RPP thin films based on previous PL studies which have detected it[1,3,7,12,13]. Highly efficient LEDs based on spin coated RPPs films have been shown to emit through this state[2,8]. Although this sub gap state dominates the emission in RPP thin films, it's intensity is greatly diminished in photoluminescence studies of RPP single crystals[3–6]. However, this feature can be observed in single crystal RPPs on the perimeter of exfoliated flakes via confocal photoluminescence spectroscopy[3]. This observation led the authors of reference 3 to name them 'edge states'. Because edge states are associated with the termination of the 2d crystalline planes, they are expected to be localized in the grain

boundaries of the poly-crystalline films, and thus dominate their optical properties due to the expected small crystalline domains present in spin-coated films[14]. Due to the spectral proximity of this feature to the previously observed edge state feature[3], we assign the prominent feature at 730nm in the TA spectrum to photoexcited carrier occupation of edge state optical transition. We note that this assignment is controversial, as recent studies of spin coated RPP thin films have assigned this feature to $MaPbI_3$[8,12] or another high n RPP contaminating the sample. However recent TA studies of $MaPbI_3$ thin films show steady state bleaching features centered at 750nm[15,16]. In chapter 5 analyzing x-ray diffraction data, serious consideration of the $MaPbI_3$ contamination hypothesis is given, but we have ultimately concluded that there is no evidence for crystalline $MaPbI_3$ in our films.

Figure 2 shows the normalized differential absorption spectrum measured on the 20nm, 50nm, 100nm, and 200nm films, for various values of the pump-probe delay time. The center of the edge state feature systematically moves from approximately 700nm in the case of the 20nm film to approximately 730nm in the case of the 200nm films. However, when comparing different batches of films there appears no robust correlation between the spectral position of the edge state feature and the film thickness. The shifting of this feature in films made from the same batch of material, and between different batches of materials indicates there exist unknown extrinsic factors determine its energetics, and also suggests that this shift is not related to a thin film interference phenomena. We suggest surface strain plays a role, which is discussed in chapter 5.

Figure 2 a-d shows that the long time spectra (mostly) take on the same shape as the early time spectra. This indicates the photo-excited carrier dynamics are not greatly impacted by cooling, which redistributes the photo-excited population in energy, changing the line shape. It also indicates that the spectral shift of the center of the edge state feature observed in the thinnest films is not a transient phenomenon related to cooling. Therefor we expect the spectral positions of the edge state feature in figure 2a-d to truly represent the energetic position of the

optical band gap in these films.

Another important feature of these spectra are small ripples between 600nm and 700nm, which gain relative prominence at late time (seen in figure 2d). We do not currently have a satisfactory explanation of the kinetics of these features or why they are observed at all. Spectrally, these features occur at the same position as native RPP excitonic peaks seen in the linear absorption spectrum in figure 1a, and in the transient spectrum shown in figure 4a-d. This seems to imply they result from photoexcited carrier occupation of these higher energy transitions. However, because these features are so much higher in energy than the edge state features (340meV between 730nm and 600nm), it is highly unlikely that they result from thermal excitation of an electron-hole pair from the edge state. High energy features can occur in these experiments resulting from undesired two photon absorption of the 730nm pump, or from residual second harmonic of the 730nm leaking through the OPA. However, it is shown in the coming sections that when the excitonic features are directly excited they decay faster than the edge states. Thus if these features were directly excited by two photon absorption or the second harmonic of the pump, we would not expect them to grow in relative prominence at late times. We note only that these features seem related to the native excitons present in the single crystal materials. The fact that the excitonic features are present under NIR excitation indicates that the edge state features likely arise from the same material as the excitonic features, as opposed to a distinct phase contaminating RPP material.

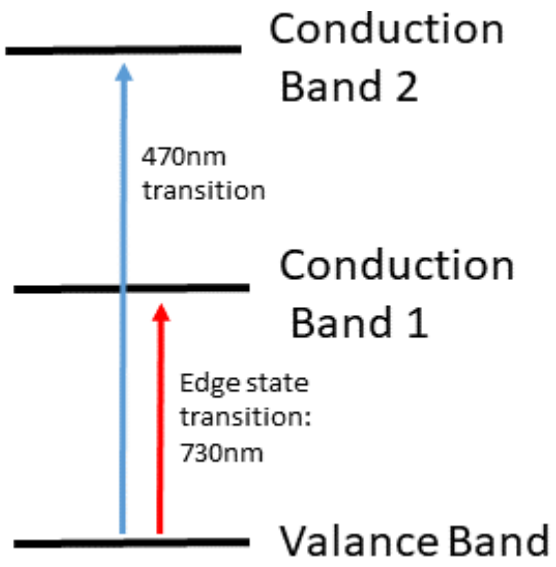


**Figure 3.** This figure shows a possible electronic structure which could explain the observed kinetics of the feature at 470nm.

In addition to the dominant edge state feature, there appears high energy bleach feature at about 470nm which is partially cut off in figure

2. The relative magnitude of this feature does not appear to change significantly with film thickness. The kinetics of the 470nm feature are directly proportional to the kinetics of the edge state feature, as is shown by its constant magnitude on the normalized curves in figure 2(a-d) which implies the magnitude of this feature is directly proportional to the population of edge states. This suggest a situation like the one depicted in figure 3. In this model the transition at 470nm shares a common valance band energy level with the edge state. Thus photoexcited holes in the valance band decrease the number of optical transitions available to conduction band 2, decreasing its optical absorption. An alternative to this model in which the 470nm transition and the edge state transition share a conduction band state is equally possible. Again, because this feature is so much higher in energy than the edge state feature it seems very unlikely that this feature corresponds to a population thermally excited from the edge state. We note that the interpretation that the valance band is shared between the edge state transition and the 470nm transition is in agreement with DFT calculations done by our collaborators in a heretofore unpublished work.

TA Analysis: 500nm Excitation

Figure 4 shows the differential absorption spectra obtained when exciting the films at 500nm. This data was obtained on the same set of films as the NIR excitation data (figure 2). Compared to the NIR excitation we see new features emerge which have distinct dynamics from the edge states, as can be seen by the changing magnitudes of the peaks on the normalized curves. All together there are 4 sharp peaks visible, the largest of which is at 605nm. Figure 4 shows that at short times the center of the edge state feature appears significantly blue shifted and broadened, while at long times the center of the edge state peak returns to the position observed under NIR excitation. A hot phonon bottleneck has recently been reported to occur in

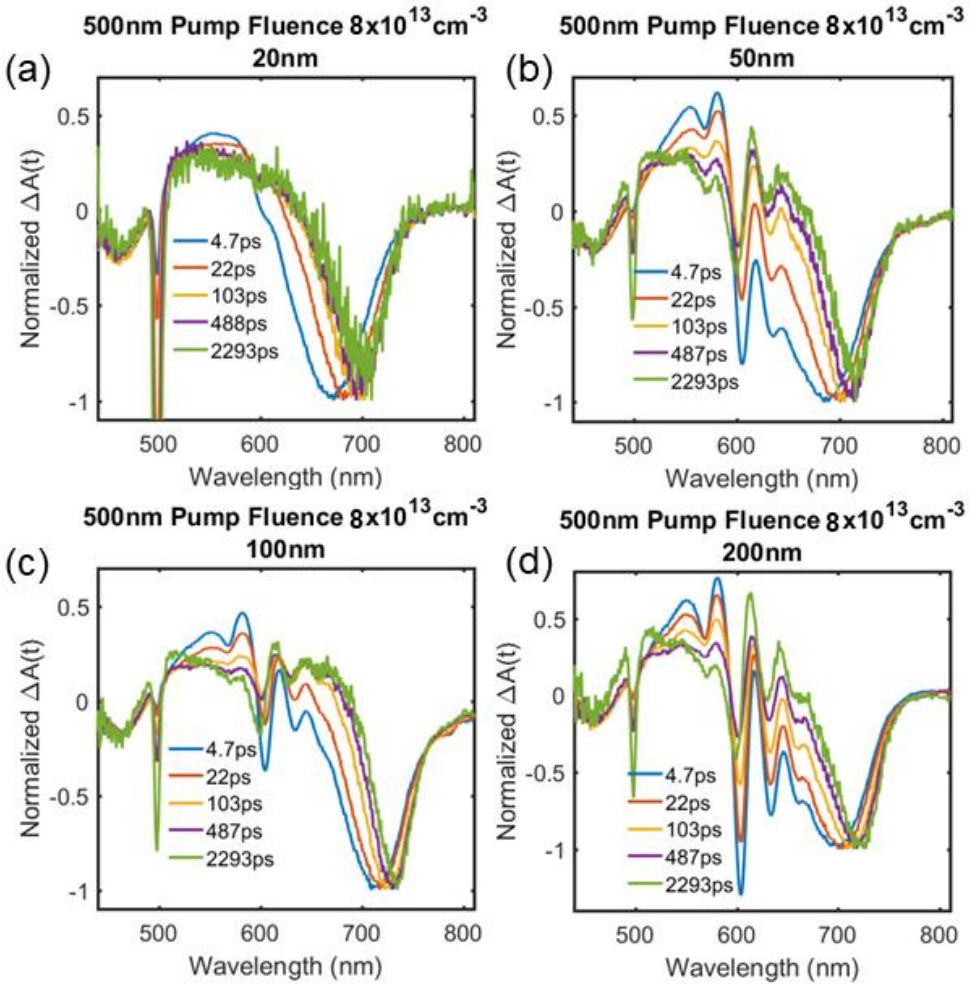


**Figure 4.** These panels show the normalized differential absorption spectrum observed in RPP thin films under 500nm excitation for various pump probe delay times. Panel a, 20nm. Panel b, 50nm. Panel c 100nm. Panel d 200nm.

$MaPbI_3$[17] at similar absorbed fluences, and in the following we consider the possibility that the shifting and broadening behavior of the edge state bleach results from a hot phonon bottle neck.

After photoexcitation, cooling of the electronic population generally occurs by the emission of optical phonons. However, at high photo-excited carrier density, so many optical phonons can be created that phonon reabsorption by the photo-excited carriers can effectively compete with dissipation of the optical phonons into acoustic phonons. In this case energy is transferred back into the electronic system, which slows the net dissipation of electronic energy in to heat. When this occurs in $MaPbI_3$[17] a cooling timescale $\tau_{cooling}$ ~40ps is observed at a photo-excited carrier

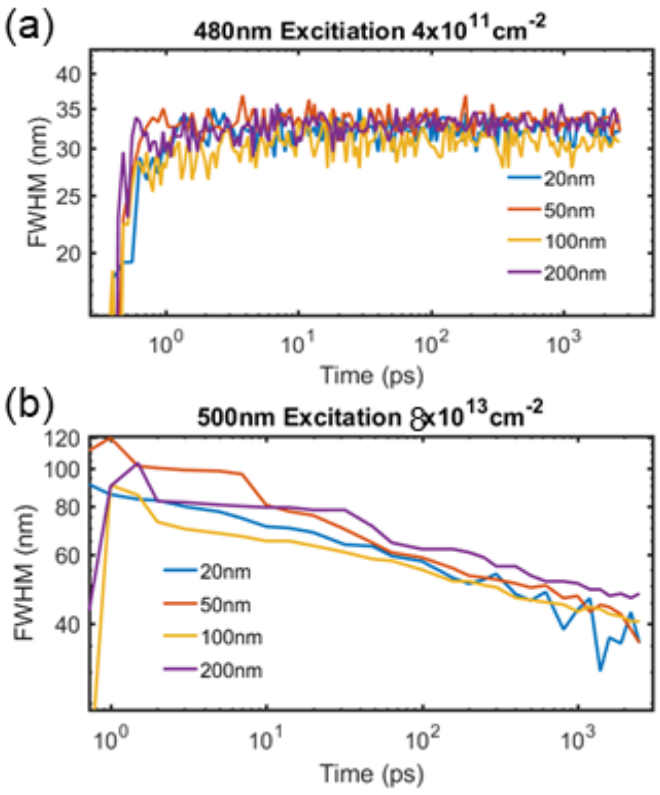


**Figure 5.** This figure shows the kinetics of the edge state feature's FWHM. Panel a shows the data obtained when exciting the film at $4x10^{11}cm^{-2}$, while panel b shows the data obtained when exciting the film with $4x10^{13}cm^{-2}$.

density of $6x10^{18}cm^{-3}$ (absorbed fluence $4.2x10^{13}cm^{-2}$), while a cooling timescale of only 50fs is observed at a density of $5.2x10^{17}cm^{-3}$ (absorbed fluence $3.6x10^{12}cm^{-2}$). This corresponds to a change in the cooling time by a factor of 800 for a density change by a factor of roughly 10.

Figure 5 shows the kinetics of the FWHM of the edge state feature (730nm) for low fluence and high fluence. Figure 5a shows that the FWHM is roughly independent of film thickness and time, in the case of an absorbed fluence of $4x10^{11}cm^{-2}$. This indicates that cooling has already completed by 1ps, in agreement with the observation that cooling by occurs on ultrafast time scales at low absorbed carrier densities[17]. Figure 5b shows the FWHM exhibits a much different time dependence in the case of a photo-excited fluence of $8x10^{13}cm^{-2}$. In panel b the FWHM starts about 3x as large as in the case of low fluence and decays slowly to roughly the same value as the low fluence case. Thus we find generically that the cooling kinetics do depend on absorbed fluence in agreement with reference 15. We note that the FWHM kinetics appear very similar in all films, which is not expected, as the thinnest film has a photo-excited carrier *density* ten times larger than that of the thickest films (density=fluence/film thickness). However, this chapter will show that the edge state feature is physically localized on the air-film interface. In this context, the similarity of the FWHM kinetics in films of varying thickness makes perfect sense.

Alternatively, such an effect could be explained by the disordered natured of the edge states. In this picture the edge states are localized and exist over a broad range of energies, and the slow motion of the carrier population downward in energy reflects the slow hopping process by which the carriers explore the energy landscape, and become stuck in low energy wells. Such a phenomenon is observed in transport studies on the band tails of disordered semiconductors such as amorphous silicon[18]. However, this picture does not account for the difference in the kinetics observed with different pump fluences. Such a picture could be brought into correspondence with the data if we assume a waiting time distribution which depends on carrier density, however this assumption is completely ad hoc. The data can be explained with the fewest assumptions in the hot phonon bottle-neck hypothesis, which we therefore adopt. In either of the stated cases this shifting and broadening phenomena indicate that the edge states have a continuum of energy levels spread over a broad range of about 300meV.

TA Analysis: 480nm Excitation, New Samples

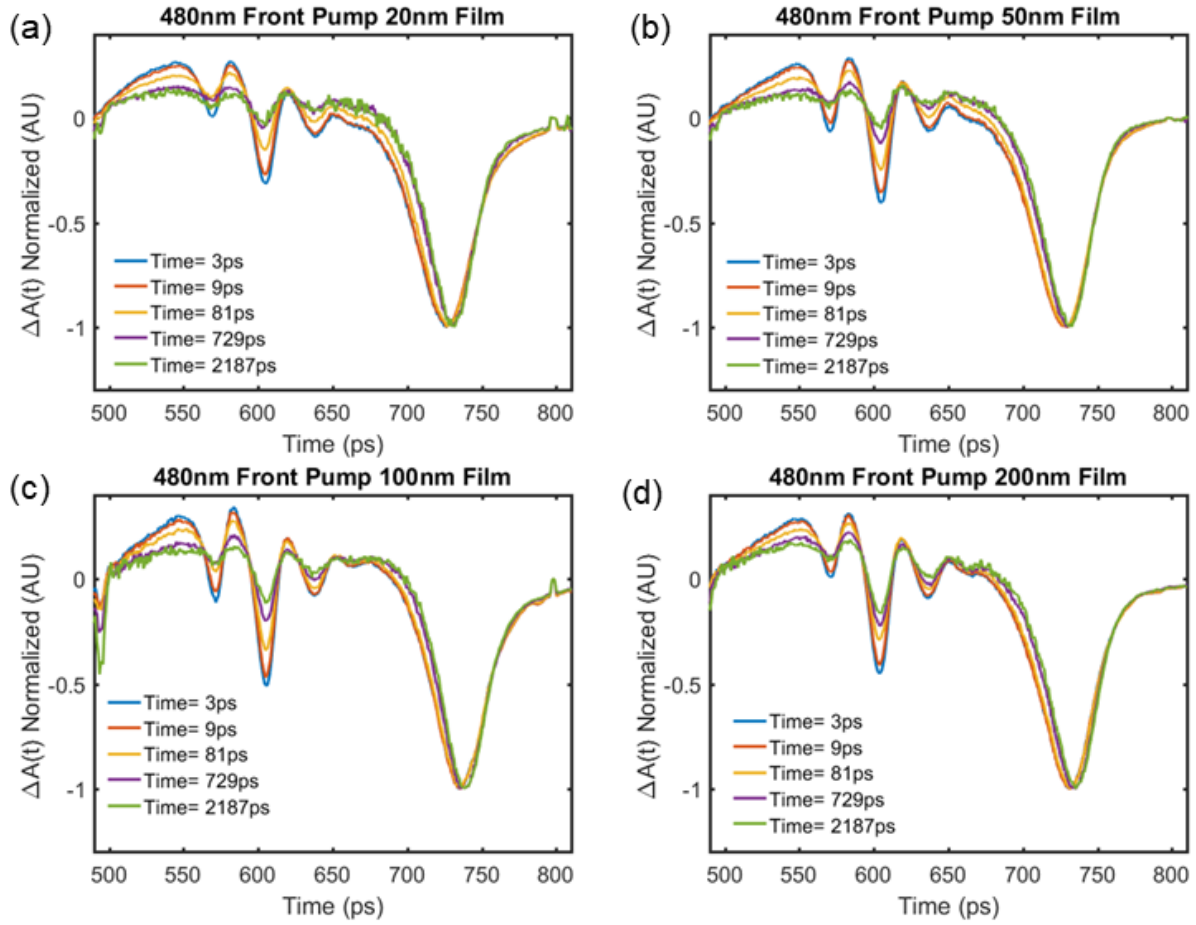


**Figure 6.** This figure shows the differential absorption kinetics obtained by exciting our new samples at 480nm with a fluence of $2x10^{13}cm^{-2}$. Panel a 20nm, panel b 50nm, panel c 100nm, panel d 200nm

We obtained a new set of hot cast n=3 RPP samples, which appear very similar to the previous ones, however we note a couple of important differences. The spectra obtained on the new batch of films are much more consistent across film thickness. For example, the edge state feature in the new batch of films appears consistently at about 730nm, whereas the 20nm film in the previous batch showed an edge state feature at 700nm. Also, the transient spectra obtained on the 20nm film from the previous batch (figure 4a), shows practically no contribution from the excitonic states which are featured prominently in the all films of the new batch. For the remainder of the chapter I'll analyze the TA spectrum of the "new batch" of films.

TA Analysis: 480nm Excitation, Front-Back Analysis

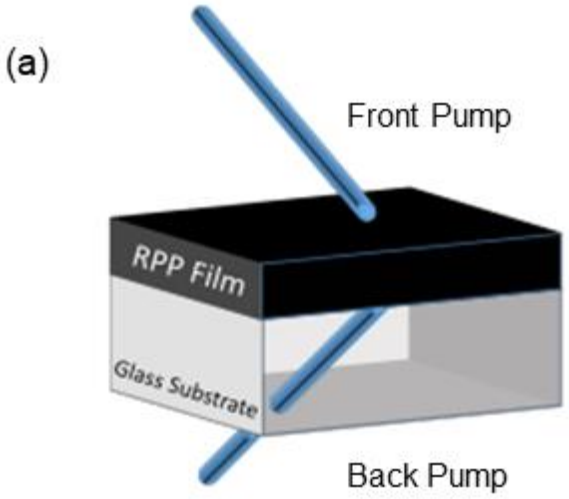


**Figure 7.** This figure defines the front and back pump geometries.

When exciting the film with visible radiation, the absorption length becomes comparable to the film thickness. At 480nm, we measure the absorption length to be about 100nm. Thus depending on the pump geometry defined in figure 7 we can selectively deposit carriers toward the air-film interface, or the glass-film interface.

Figure 8 shows the transient spectra at 5ps obtained in the front and back pump geometries when exciting our hot cast RPP films with 480nm radiation for an absorbed fluence of $4x10^{11}cm^{-2}$. We find that the size of the edge state feature is larger in the in front pump geometry than in the back pump geometry in all films. In the case of the 200nm film, we observed an edge state feature which is roughly seven times larger in the front pump geometry than the back pump geometry. This front back asymmetry is fundamentally driven by the relationship between the absorption length and the film thickness, and accordingly the asymmetry decreases significantly in the thinner films. In this respect one would expect no asymmetry at all in the case of the 20nm and 50nm films, and this will be addressed directly in the coming paragraphs. As established in chapter 4 the early time (~5ps) transient absorption spectrum contains information about the electronic structure in the volume excited by the laser. Therefor the relatively small magnitude of the edge state feature in the back pump geometry reflects a relative paucity of edge states on the glass-film interface and through the bulk of the film. Conversely, the relatively large edge state feature observed in the front pump geometry implies that the edge states exist

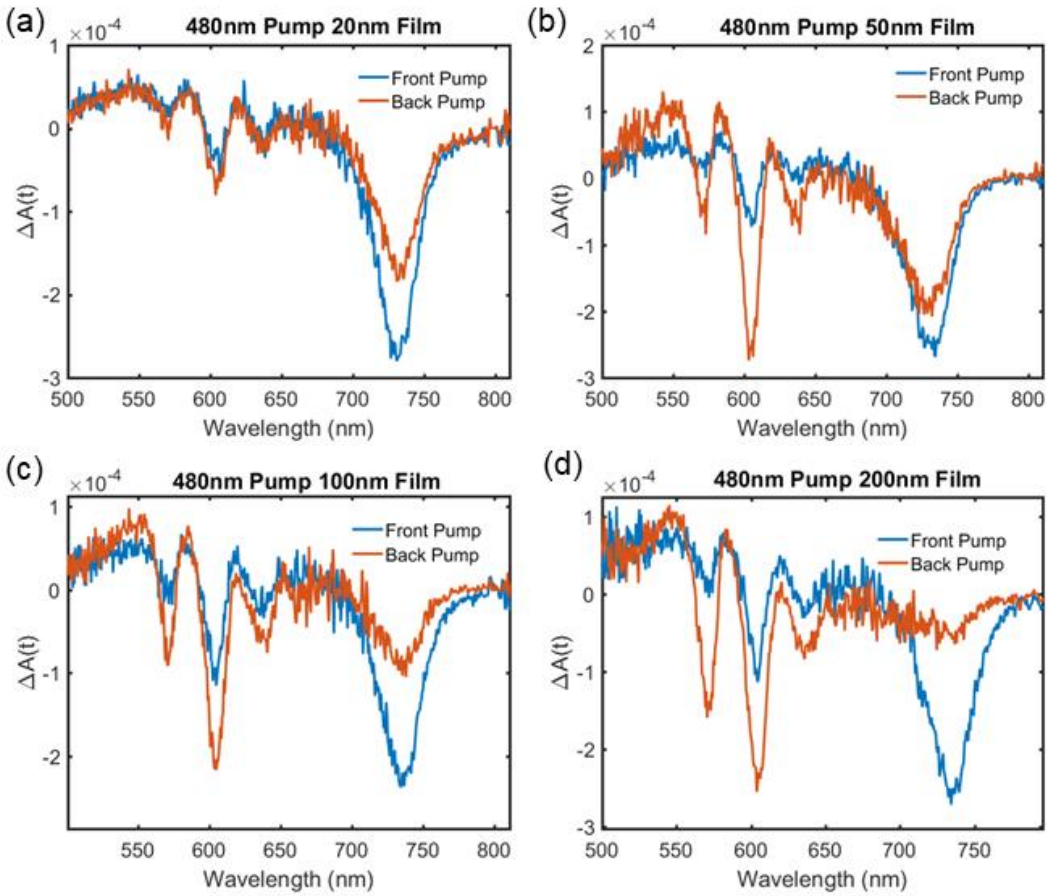


**Figure 8.** This figure compares the transient absorption spectra obtained when exciting our films at 480nm in the front pump and back pump geometries. In all cases the absorbed fluence is $4x10^{11}cm^{-2}$.

preferentially towards the air film interface. We note also that that the decreased magnitude of the edge state feature in the back pump geometry is correlated with an increased magnitude of the excitonic features. Thus it appears that one population is created at the expense of the other as would be expected.

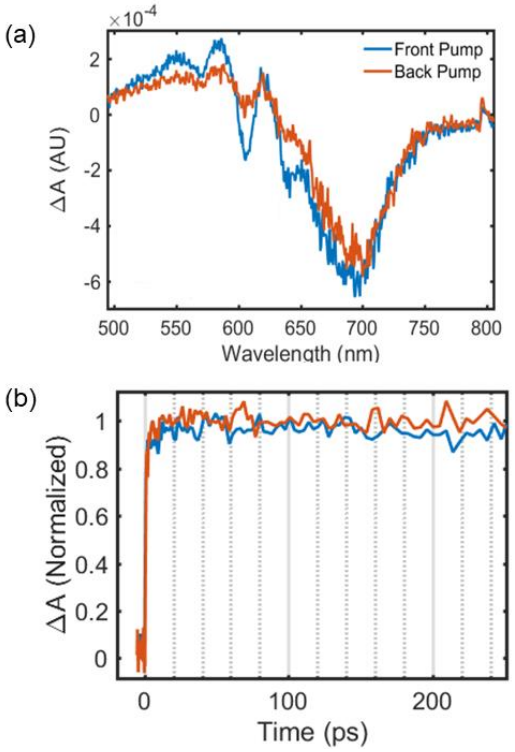


**Figure 9.** Panel a shows the transient spectra obtained at 3ps when exciting a post annealed film at 480nm with an absorbed fluence of $8x10^{11}cm^{-2}$. Panel b shows the kinetics of the edge state feature in the front and back pump geometry, taken under the same conditions as panel a.

Figure 9 shows that such profound asymmetry is not present in 200nm thick post annealed films, indicating that the edge states are distributed symmetrically in the post annealed film. Additionally, the 200nm post annealed films exhibits an edge state feature which is dramatically shifted relative to the 200nm hot cast sample. The appearance of the edge state feature at 700nm, and the relative front back symmetry in post annealed films indicates the profound electronic consequences of different spin coating deposition methods. We thus conclude there is something 'special' about the hot casting technique that drives all of the edge states out of the bulk and on to the surface. We hypothesize that this phenomenon is related to concomitant macroscopic alignment of the [101] planes parallel to the substrate in hot cast films (shown in chapter 5). This difference in the distribution of edge states may be of profound technological significance as post annealed films generally exhibit a 3x lower photovoltaic power conversion efficiency (~4%) than hot cast films ( 12%)[1]. This seems to imply that the segregation of edge states observed in hot cast films is an essential ingredient in producing high quality photovoltaics devices using RPP materials.

The conclusion that edge states have an impact on photovoltaic device performance is supported by the work of Liu et al[12], where they showed that depositing an electron accepting film (PCBM) on top of the RPP film produces strong quenching of the edge state feature, while

depositing the RPP film on top of a hole accepting film (PEDOT:PSS) has no impact on the edge state feature. We have confirmed the latter result in our lab as well. This indicates the surface localized nature of the edge state feature in RPP films survives the deposition of an electron accepting layer, and that charge transfer occurs between these films. These facts correlate with our understanding of edge states as localized on the films front surface. We note that PCBM and PEDOT:PSS are the same electron accepting and hole accepting contacts used in the highly efficient RPP photovoltaic devices[1].

Figure 10b shows the differential absorption spectral kinetics obtained on a 200nm hot cast thin film in the back pump geometry. This spectrum displays three sharp and prominent excitonic peaks, as well as the edge state feature at 730nm. The excitonic peaks in the differential absorption spectrum have corresponding peaks in the linear absorption spectrum in figure 10a. In the back pump geometry, these peaks display a nearly instrument limited rise time (<1ps) and subsequently decay. However, the dominant kinetic process of the edge state feature at 730nm is a slow rise that roughly correlates with the decay of the excitonic features. Based on our finding regarding the surface localization of the edge states, we hypothesize the long slow rise of the edge state feature results from diffusion of excitons from the back of the film to the front, where they decay into the much lower energy edge states. Let us make some predictions based on this model.

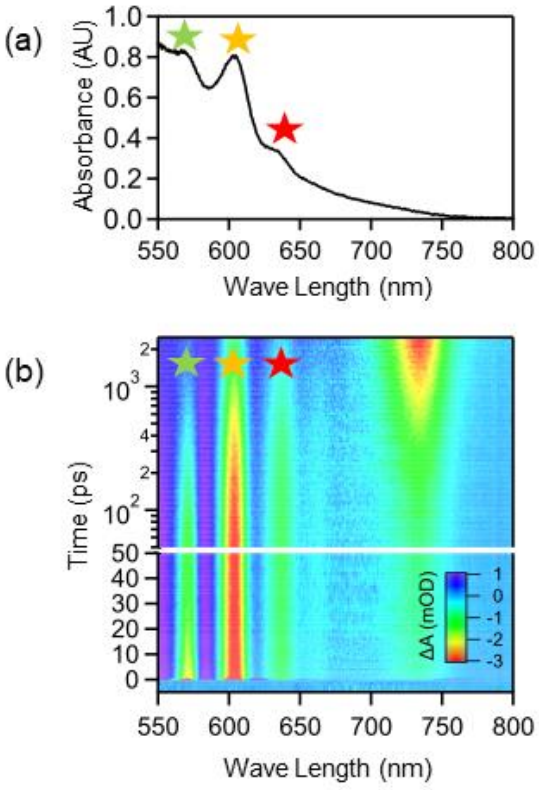


**Figure 10.** Panel a shows the measured linear absorption of a 200nm n=3 hot cast RPP film. Panel b shows the TA spectrum obtained on the same film when excited at 480nm in the back pump geometry with a fluence of $1.2x10^{12}cm^{-2}$.

Modeling the Edge State and Excitonic Kinetics Using the 1D Diffusion Equation

In order to make our model soluble, we make four simplifying assumptions: 1) edge states are entirely localized at the front of the film 2) excitons decay into edge states immediately upon arrival in the vicinity of the surface 3) there is no flux of excitons from the glass into the film or the film into the glass 4) we neglect any exciton decay in travel from the back of the film to the front. Under these assumptions the excitonic density ρ(x,t) can be simply modeled using the diffusion equation. The above conditions imply that the edge state population per unit area n(t) is given by:

$$n(t) = \int_0^t J(L,t')dt' = -D\int_0^t \frac{\partial \rho}{\partial x}(L,t')dt'$$

Which comes from assumption 2. The diffusion equation for the excitonic density ρ is:

$$\frac{\partial \rho}{\partial t} = D\nabla^2\rho$$

Where D is the diffusion constant. We assume the glass interface is at x=0 thus the boundary conditions reads:

$$\lim_{x\to 0} \frac{d\rho(x,t)}{dx} = 0$$

Which comes from the no flux assumption, number 3. The at the other boundary we stipulate:

$$\lim_{x\to L} \rho(x,t) = 0$$

Which is a result of assumptions 1 and 2. The temporal boundary condition at t=0 reads:

$$\lim_{t\to 0} \rho(x,t) = \frac{e^{-x/\beta}}{\beta}$$

Which is the initial distribution of photoexcitations in the film in the back pump geometry. Here β is the absorption length of 100nm. We also stipulate that the solution should go to zero as time goes to infinity. The eigenfunctions obeying the spatial boundary conditions are:

$\varphi_n(x,t) = \cos(k_n x)\, e^{-\gamma_n t}$ such that $k_n = \frac{\pi(2n+1)}{2L}$, $n \in \{0,1,2 \ldots \infty\}$

Using the diffusion equation, one can show these eignefunctions obey the diffusive dispersion relation:

$$\gamma_n = Dk_n^2 = D\left(\frac{\pi(2n+1)}{2L}\right)^2$$

Or:

$$\tau_n = D^{-1}\left(\frac{2L}{\pi(2n+1)}\right)^2$$

This show that the decay rate of the diffusive eignefunctions increases quickly with n. The n=1 mode decays 9 times faster than the n=0, and the n=2, 25 times faster. It is therefore reasonable to assume that the slow rise behavior of the TA signal results from only the slowest diffusive mode. This assumption is very good particularly in the thicker films where the initial distribution has a strong spatial overlap with the lowest diffusive mode. In this mode:

$$\tau(L)_1 = D^{-1}\left(\frac{2L}{\pi}\right)^2$$

Thus:

$$n(t) = \int_0^t J(L,t')dt' = -D\int_0^t \frac{\partial \rho}{\partial x}(L,t')dt' = -\gamma(L)_1^{-1}\int_0^t e^{-\gamma(L)_1 t'}dt' = \left(1 - e^{-\gamma(L)_1 t}\right)$$

$$= \left(1 - e^{-\gamma(L)_1 t}\right) \quad (1)$$

Using the convention that n =1 at late times. Thus, because magnitude of the edge sate feature is directly proportional to the population occupying the edge states we expect the rise of edge state feature to evolved similarly to equation 1. There exists some uncertainty in what the initial population in the edge states is, both from the decay of the faster modes, and perhaps some initial excitation by laser penetrating through the film. In the above model the initial edge state

population it is exactly zero, but we are free to add a constant initial population in the edge states. Thus we predict the rise time of the edge state feature ($\tau_{rise}^{730nm}$) to vary with film thickness according to $\tau(L)_1$, meaning we expect it to vary proportionally to $L^2$.Therefore if we fit our rising edge data with the function:

$$\Delta A(730nm, t) = A - Be^{-\gamma(L)_1 t} \quad (1)$$

as a function of film thickness we can construct the plot of $\tau_{rise}^{730nm}$ vs $L^2$. Recalling the diffusive dispersion relation, we have:

$$\tau(L)_1 = D^{-1}\left(\frac{2L}{\pi}\right)^2 = \tau_{rise}^{730nm}(\mathrm{L})$$

Thus when plotting $\tau_{rise}^{730nm}$ vs $L^2$ the slope 'm' will be equal to $D^{-1}\left(\frac{2}{\pi}\right)^2$

The diffusion constant is then given as: $D = m^{-1}\left(\frac{2}{\pi}\right)^2$.

Figure 11a shows that under conditions of identical low ($4x10^{11}cm^{-2}$, 480nm) absorbed fluence in the back pump geometry, the rise time of the edge state feature is a monotonically increasing function of film thickness. The edge state rising kinetics in the 300nm and 400nm films are shown in figure 11b, and continue this trend. Amazingly, it takes almost 15ns for the edge state signal to reach it maximum value in the 400nm film. We note that at these low absorbed fluences, we don't expect a hot phonon bottleneck to impact our observations, as is shown by the invariance of the FWHM in time in figure 5a. Figure 11e shows the decay time of the n=3 excitonic feature at 605nm is a monotonically increasing function of film thickness in

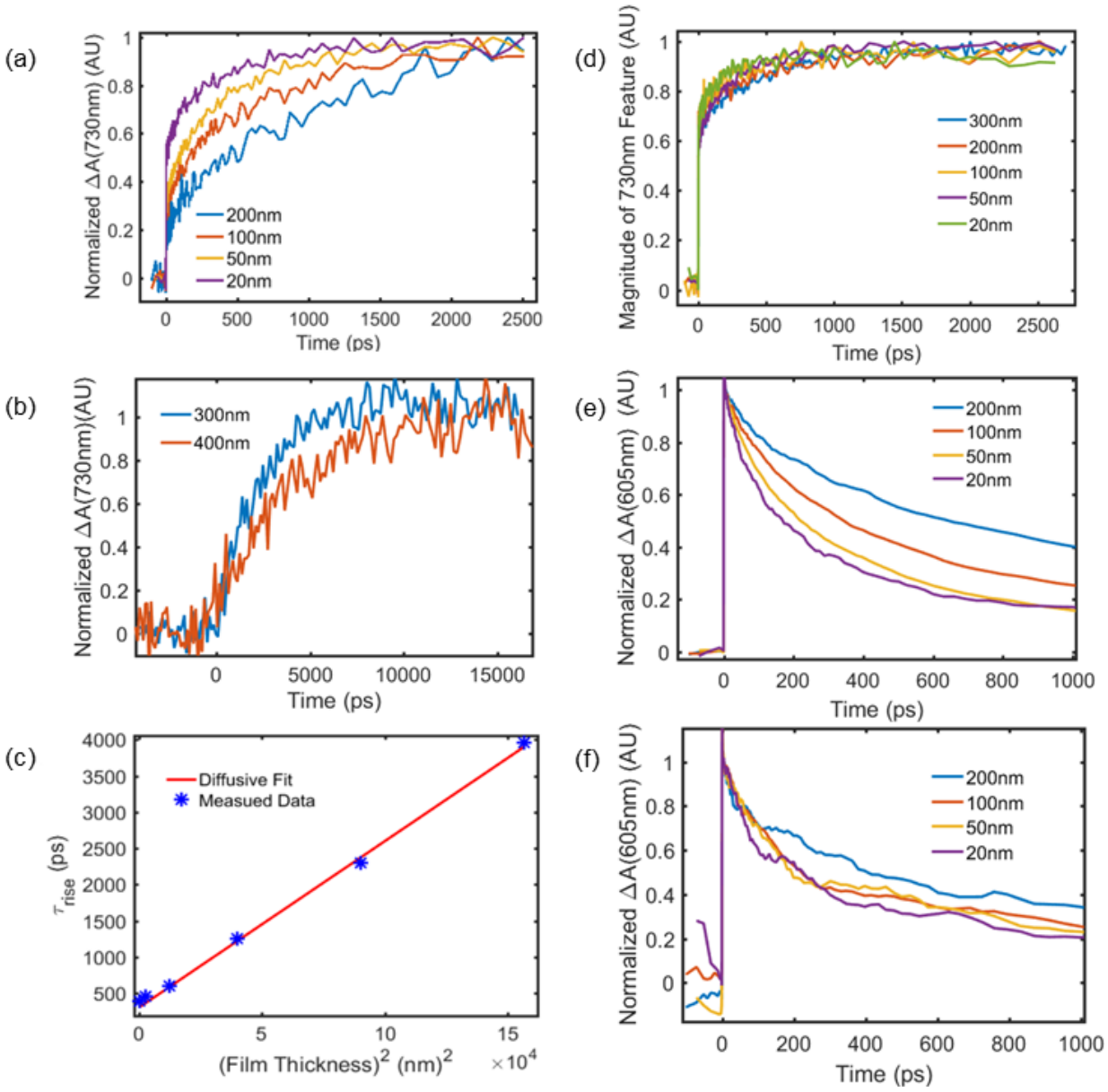


**Figure 11.** This figure shows the kinetics of various differential absorption features obtained when exciting our film at 480nm with an absorbed fluence of $4x10^{11}cm^{-2}$. Panel a shows the normalized rising kinetics of the edge state feature in the 20nm-200nm films. Panel b shows the same data, obtained on 300nm and 400nm films. The time scales extracted by Fitting the data in panels a and b are plotted vs $L^2$ in panel c. Panel d shows rising kinetics of the edge state feature obtained in the front pump geometry. Panel e shows the normalized excitonic decay kinetics in films of various thicknesses in the back pump geometry. Panel f shows the same excitonic kinetics obtained in the front pump geometry.

the back pump geometry. In contrast to figures 11a and 11e, figures 11d and 11f indicate the rising kinetics of the edge state feature, the and exciton decay kinetics in the front pump

geometry are largely independent of film thickness.

The variation of the excitonic decay time and the edge state rise time with film thickness, as well as the observed asymmetry of these features in the front and back pump geometries imply that these kinetics could not result from any intensive process in the film. Thus figures 11a and 11e demonstrate a strong agreement with our model in which the diffusion of excitons and their subsequent decay into edge states dominates the observed photo-excited carrier dynamics. This is one of the main results of this thesis. Note the strong contrast between the front-back kinetics of edge state feature in hot cast films in figure 11 with the post annealed films in figure 9.

The edge state rising kinetics were fit with the function defined in equation 1, and the extracted time scales are plotted vs the square film thickness in figure 11c, and this relationship appears satisfactorily linear. We note that for the thinnest film (20nm) there appears a deviation from the prediction of the model. The rise time for this film is longer than what is predicted by our model. As we have assumed that every carrier which is incident on the interface is absorbed by the edge states, it would be inconsistent to ascribe this deviation to a finite 'capture rate' by the edge sates *without making additional assumptions*. We therefor note that the 20nm films exhibit a bi modal distribution of layer stacking motifs, as is revealed in their small angle scattering pattern (shown chapter 5), and we ascribe this deviation at low film thickness to this observed structural difference.

The slope of the fitting line in figure 7c is equal to 0.023($ps/nm^2$) which according to equation 2 corresponds to a diffusivity of 0.176$cm^2 s^{-1}$. Using the Einstein relation, we can compare this value to carrier mobilities measured on these materials in the past. Previous measured mobilities in spin coated RPP thin films have yielded very small values from $1.1x10^{-4}$-$10^{-2}$ [1,19] for both electrons and holes. We note that the measurement on the high end of this range was taken by our collaborators who made our samples implying that a difference

in material preparation is likely not the cause of the discrepancy. These mobility values correspond to diffusivities between $2.8\text{x}10^{-6}\text{cm}^2\text{s}^{-1}$ and $2.5\text{x}10^{-2}\text{cm}^2\text{s}^{-1}$. This amounts to a disagreement by a factor between $7\text{x}10^2$ and $7\text{x}10^4$. The diffusion coefficient of free carriers in semiconductors is on the order of $D \sim \frac{\tau^* K_b T}{m^*}$ where $\tau^*$ is the carrier scattering time and $m^*$ is the band effective mass.

It is clear that the exciton mass cannot be responsible for the observed discrepancy because excitons are generally heavier than free carriers and thus diffuse more slowly which is the opposite trend from what is observed. The electronic temperature is likely to play a role in this large discrepancy, but certainly cannot account for all of it. We estimate the maximum possible electronic temperature using the equipartition theorem. In these experiments the material was excited at 2.6eV, while the ground state n=3 exciton is at 2.05eV. Assuming that all of the excess energy turns in to the excitons kinetic energy yields an average kinetic energy of 600meV. We note that this is large enough to ionize the excitons but let us assume this energy is stored in the excitons translational motion as a worst case scenario. Using the equipartition theorem for two dimensional system implies that $600meV = K_b T$, which implies at maximum the electronic temperature is a factor of 24 larger than room temperature. This would account for an increase in the diffusion constant by a factor of 24, which cannot account for the measured discrepancy factor of at least 700. We thus conclude that the scattering time varies by at least a factor of 30 and thus accounts for the majority of the variation between exciton diffusivity and the free carrier diffusivity. This discrepancy warrants additional discussion.

We note a recent report in which the PL line width and decay rate are studied as a function of temperature. Their analysis shows that the temperature scaling of the optical properties are inconsistent with both charged impurity scattering, and polar optical phonon scattering, indicating that homopolar optical phonons and acoustic phonons interacting through the

deformation potential are the main source of excitonic scattering[20]. They put an upper limit on the deformation potential of $6x10^8$eV/cm (6eV/Å ) which (without expertise in the matter), seems very large . They conclude that the excitons are protected from scattering mediated by the coulomb interaction due to the formation of an exciton–polaron. This reference was included because they have a similar conclusion to ours, however we note that the logic employed in the paper appears fundamentally flawed. They assume that the rise time of the photoluminescence is the decoherence time of the optical polarization, which they then relate to exciton scattering mechanisms. However as noted in chapter 4 there are a number of processes which can occur on these time scales that could give rise to delayed luminescence, such as phonon assisted cooling. Their data at 200K implies a decoherence time of 20ps, which seems unphysical in comparison with the phonon induced dephasing time measured in GaAs quantum wells at 200K of 100fs[21]. Furthermore, they claim that the photoluminescence decay time is proportional to the exciton scattering time, which is quite hard to understand.

We believe the large discrepancy between our diffusivity value and that of our collaborators results from incorrect assumptions which they have made about the nature of the films in calculating the mobility from their data. They have calculated the mobility using the carrier extraction by linearly increasing voltage (CELIV) technique which is commonly applied to very low mobility organic semiconductor films[22,23]. However in it's closed from is not applicable to higher mobility films[23]. We believe that it is worth it to perform more quantitative experiments that directly measure the excitonic scattering time as a function of temperature to gain information about the types of interactions which scatter excitons. We suggest a photon echo experiment, which is capable of measuring the dephasing time of an inhomogeneously broadened transition[24].

Back Pump TA Kinetics Vs Absorbed Fluence

Figure 12 shows the observed kinetics of the edge state feature normalized by the

absorbed fluence. The dynamic behavior of these curves depends greatly on the absorbed fluence. At low fluence, the rise of the edge state feature dominates the kinetics, while at high fluence the decay of the edge state feature dominates. One prominent trend observed in figure 12 is a decrease in the maximum bleach per particle, as the fluence increases. This effect is shown by by the decreasing magnitude of the curves in figure 12 with increasing fluence. Modeling of these decay kinetics shows that this effect can be properly understood as a

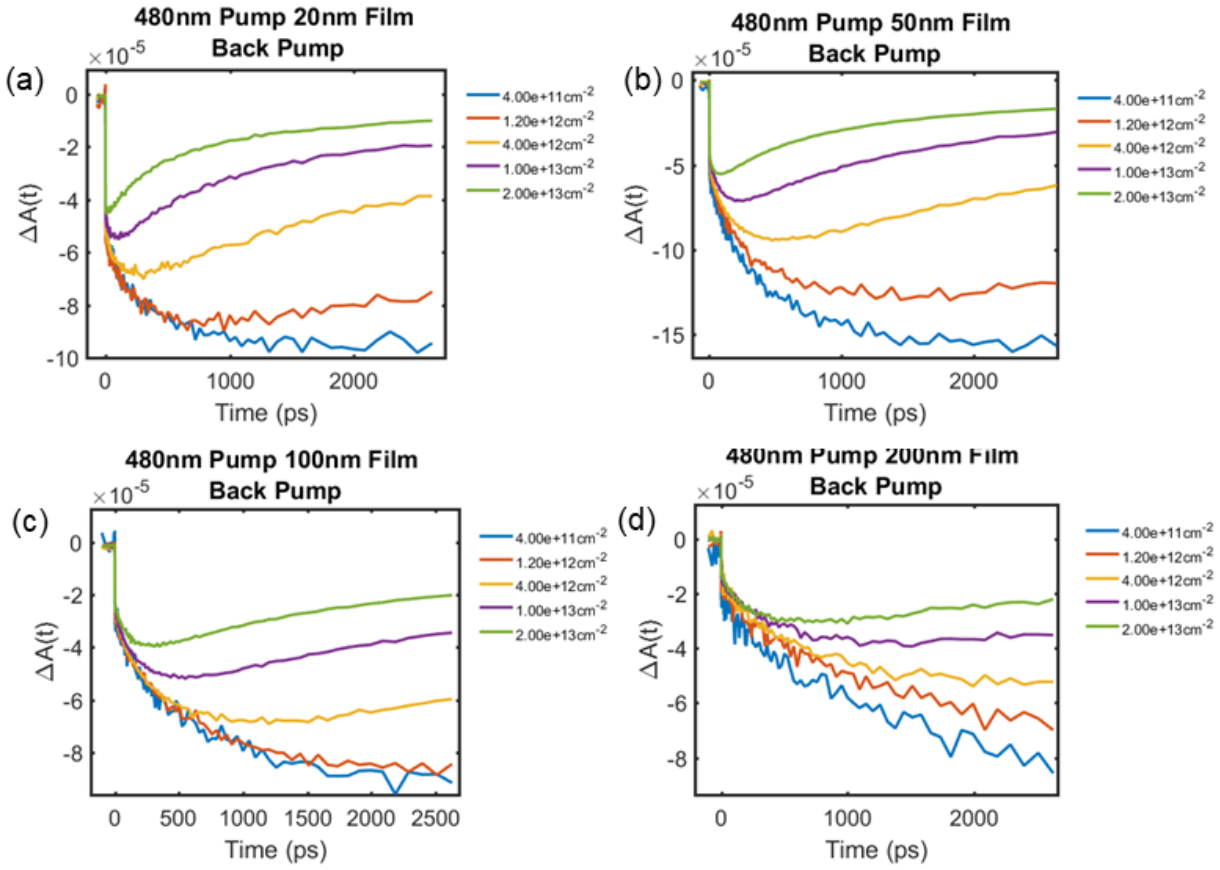


**Figure 12.** This figure shows the kinetics of the edge state feature normalized by the absorbed fluence in the back pump geometry, for various film thicknesses.

competition between a first order diffusive process which injects population into the edge states, and a higher order decay process which annihilates photo excited carriers from the edge states, for example photoluminescence. An increased contribution to the decay kinetics from radiative recombination at higher photo-excited carrier density is consistent with the increased

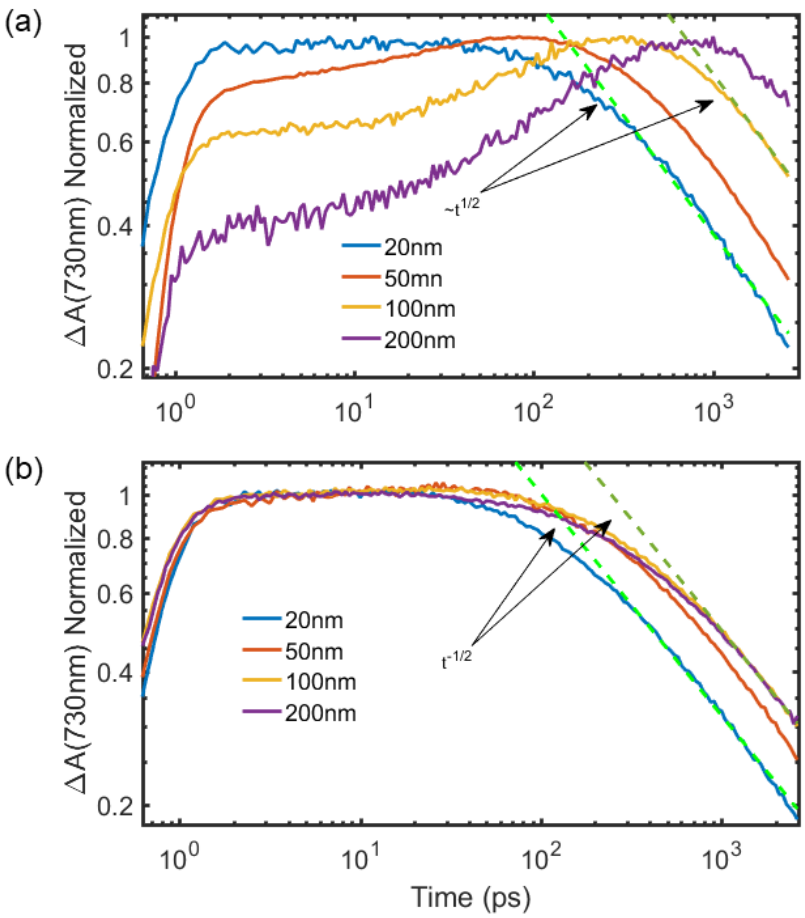


**Figure 13.** Panel a shows the edge state kinetics obtained in the back pump geometry under 480nm excitation with an absorbed fluence of $2x10^{13}cm^{-2}$. Panel b shows the same data obtained under the same conditions as panel a, but in the front pump geometry.

photoluminescence quantum yields (~20%) observed in RPP thin films at similar absorbed fluences[3]. Figure 11 shows that at a fluence of $4x10^{11}cm^{-2}$ we cannot observe the effect of recombination, thus we a justified in extracting the diffusion time scale from this data.

At late times the diffusive process is over and the decay kinetics of the edge state feature become clear. Figure 13a shows that at late times the edge sate feature decays as a power law with $\Delta A(t) \sim t^{1/2}$. Figure 13b shows that in the front pump geometry we come to the same conclusion, however the influence of diffusion is significantly less than in the back pump geometry. To establish pure power law behavior, it is generally accepted to observe the decay over at least two orders of magnitude, which we cannot do. However this argument shows that the asymptotic decay behavior of the edge state features concur in the front and back pump geometries (in the time window we can observe), which can be understood as a consequence of the surface localized nature of the edge state feature. We note that the observed power law decay $\sim t^{-1/2}$ cannot be understood in the context of a standard kinetic model in which population decay is proportional

to an integer power of the density.

In conclusion, we have shown that in hot cast films the luminescent mid gap edge state is localized on the surface of the film, which is in strong contrast with the behavior observed in post annealed films. We have established this by observing the early time differential absorption spectrum, as well as diffusive behavior in the rise of the edge state feature, and the decay of the excitonic feature at low absorbed fluence. We have extracted the excitonic diffusion constant, and shown it is significantly larger than what is expected based on measured single carrier diffusivities. In addition, we have observed strongly density dependent cooling kinetics which are consistent with a hot phonon bottleneck. This optics data in conjunction with our observation of a surface localized structural distortion in chapter 5 strong support to the interpretation that the edge states are created by the surface distortions, rather contamination of the sample by $MaPbI_3$.


1. Tsai, H. *et al.* High-efficiency two-dimensional Ruddlesden–Popper perovskite solar cells. *Nature* **536,** 312–316 (2016).
2. Tsai, H. *et al.* Stable Light-Emitting Diodes Using Phase-Pure Ruddlesden-Popper Layered Perovskites. *Adv. Mater.* **30,** 1704217 (2018).
3. Blancon, J.-C. *et al.* Extremely efficient internal exciton dissociation through edge states in layered 2D perovskites. *Science* **355,** 1288–1292 (2017).
4. Wang, K., Wu, C., Yang, D., Jiang, Y. & Priya, S. Quasi-Two-Dimensional Halide Perovskite Single Crystal Photodetector. *ACS Nano* (2018). doi:10.1021/acsnano.8b01999
5. Cao, D. H., Stoumpos, C. C., Farha, O. K., Hupp, J. T. & Kanatzidis, M. G. 2D Homologous Perovskites as Light-Absorbing Materials for Solar Cell Applications. *J. Am. Chem. Soc.* **137,** 7843–7850 (2015).
6. Stoumpos, C. C. *et al.* Ruddlesden–Popper Hybrid Lead Iodide Perovskite 2D Homologous Semiconductors. *Chem. Mater.* **28,** 2852–2867 (2016).

7. Milot, R. L. *et al.* Charge-Carrier Dynamics in 2D Hybrid Metal–Halide Perovskites. *Nano Lett.* **16,** 7001–7007 (2016).
8. Yuan, M. *et al.* Perovskite energy funnels for efficient light-emitting diodes. *Nat. Nanotechnol.* **11,** 872–877 (2016).
9. Zhou, N. *et al.* Exploration of Crystallization Kinetics in Quasi Two-Dimensional Perovskite and High Performance Solar Cells. *J. Am. Chem. Soc.* **140,** 459–465 (2018).
10. Proppe, A. H. *et al.* Synthetic Control over Quantum Well Width Distribution and Carrier Migration in Low-Dimensional Perovskite Photovoltaics. *J. Am. Chem. Soc.* **140,** 2890–2896 (2018).
11. Li, L. *et al.* Unraveling the Growth of Hierarchical Quasi-2D/3D Perovskite and Carrier Dynamics. *J. Phys. Chem. Lett.* **9,** 1124–1132 (2018).
12. Liu, J., Leng, J., Wu, K., Zhang, J. & Jin, S. Observation of Internal Photoinduced Electron and Hole Separation in Hybrid Two-Dimentional Perovskite Films. *J. Am. Chem. Soc.* **139,** 1432–1435 (2017).
13. Venkatesan, N. R., Labram, J. G. & Chabinyc, M. L. Charge-Carrier Dynamics and Crystalline Texture of Layered Ruddlesden–Popper Hybrid Lead Iodide Perovskite Thin Films. *ACS Energy Lett.* **3,** 380–386 (2018).
14. Straus, D. B. & Kagan, C. R. Electrons, Excitons, and Phonons in Two-Dimensional Hybrid Perovskites: Connecting Structural, Optical, and Electronic Properties. *J. Phys. Chem. Lett.* **9,** 1434–1447 (2018).
15. Manser, J. S. & Kamat, P. V. Band filling with free charge carriers in organometal halide perovskites. *Nat. Photonics* **8,** 737–743 (2014).
16. Price, M. B. *et al.* Hot-carrier cooling and photoinduced refractive index changes in organic–inorganic lead halide perovskites. *Nat. Commun.* **6,** (2015).
17. Yang, Y. *et al.* Observation of a hot-phonon bottleneck in lead-iodide perovskites. *Nat. Photonics* **10,** 53–59 (2016).

18. *Charge Transport in Disordered Solids with Applications in Electronics: Baranovski/Charge Transport in Disordered Solids with Applications in Electronics*. (John Wiley & Sons, Ltd, 2006). doi:10.1002/0470095067
19. Ma, C., Shen, D., Ng, T.-W., Lo, M.-F. & Lee, C.-S. 2D Perovskites with Short Interlayer Distance for High-Performance Solar Cell Application. *Adv. Mater.* 1800710 (2018). doi:10.1002/adma.201800710
20. Guo, Z., Wu, X., Zhu, T., Zhu, X. & Huang, L. Electron–Phonon Scattering in Atomically Thin 2D Perovskites. *ACS Nano* **10,** 9992–9998 (2016).
21. Kim, D.-S. *et al.* Giant excitonic resonance in time-resolved four-wave mixing in quantum wells. *Phys. Rev. Lett.* **68,** 1006–1009 (1992).
22. Tiwari, S. & Greenham, N. C. Charge mobility measurement techniques in organic semiconductors. *Opt. Quantum Electron.* **41,** 69–89 (2009).
23. Lorrmann, J., Badada, B. H., Inganäs, O., Dyakonov, V. & Deibel, C. Charge Carrier Extraction by Linearly Increasing Voltage:Analytic framework and ambipolar transients. *J. Appl. Phys.* **108,** 113705 (2010).
24. Shah, J. & American Telephone and Telegraph Company. *Ultrafast spectroscopy of semiconductors and semiconductor nanostructures*. (Springer, 1996).